PATTERN-INTEGRATED INTERFERENCE LITHOGRAPHY: SINGLE-EXPOSURE FORMATION OF PHOTONIC-CRYSTAL LATTICES WITH INTEGRATED FUNCTIONAL ELEMENTS

A Thesis
Presented to
The Academic Faculty

by

Guy Matthew Burrow

In Partial Fulfillment
of the Requirements for the Degree
Doctor of Philosophy in the
School of Electrical and Computer Engineering

Georgia Institute of Technology
August 2012

PATTERN-INTEGRATED INTERFERENCE LITHOGRAPHY: SINGLE-EXPOSURE FORMATION OF PHOTONIC-CRYSTAL LATTICES WITH INTEGRATED FUNCTIONAL ELEMENTS

Approved by:

Professor Thomas K. Gaylord, Advisor
School of Electrical and Computer Engineering
Georgia Institute of Technology

Professor Muhannad S. Bakir
School of Electrical and Computer Engineering
Georgia Institute of Technology

Professor Miroslav M. Begovic
School of Electrical and Computer Engineering
Georgia Institute of Technology

Dr. Donald D. Davis
School of Electrical and Computer Engineering
Georgia Institute of Technology

Professor Zhuomin Zhang
School of Mechanical Engineering
Georgia Institute of Technology

Date Approved: 29 May 2012

ACKNOWLEDGEMENTS

Over the course of nearly three years at Georgia Tech, numerous people have impacted my life and proven instrumental to the research presented in this thesis. It is with great appreciation and humility that I acknowledge their support and contributions.

First and foremost, I want to express my sincere thanks to my advisor, Professor Thomas K. Gaylord. I am grateful to have had the chance to learn and develop under his expert guidance. Having served for more than 20 years in the Army, I have found no better example of a true professional. Thank you, sir, for being such a great mentor and leader to us all.

I would also like to recognize the other members of my thesis committee: Professor Muhannad S. Bakir, Professor Miroslav M. Begovic, Dr. Donald D. Davis, and Professor Zhuomin Zhang. Your participation and guidance throughout this process were invaluable. Knowing the busy schedule that you all keep, I sincerely appreciate your time and consideration.

I am also grateful to have worked alongside the other outstanding members of the Georgia Tech Optics Laboratory. Whether problem-solving with Dr. Mike Hutsel, receiving cleanroom instruction from Jon Maikisch, developing laboratory procedures with Joe Kummer, or asking Matthieu Leibovici for one more simulation using his Fourier model, I could not have anticipated the level of teamwork and support that I have experienced in this group. For our Friday lunch discussions and other words of wisdom, I would also like to thank the other group members, past and present, including Dr. Chien-I Lin, Micah Jenkins, Lorelyn Kilby, Prof. Amy Sullivan, LTC(R) Greg Kilby,

Prof. Stephen Schultz, David Davis, Jacob Block, Melissa Meister, Laney Hall, and, of course, Dr. Justin Stay, from whom I inherited this well-developed line of research.

From the Georgia Tech Machine Shop, I would like to thank Louis Boulanger for his expert fabrication of the custom components for the experimental configuration.

I would also like to thank my family and friends who have helped me throughout my life: my mother Debbie, my father Guy, my sister Kathryn and her family, and my brother John and his family. I want to specifically acknowledge my grandmother, Iona Hardison, for developing both my scientific and creative mind through everything from science fairs to art lessons. Of course, there are countless educators from grade school through grad school who provided me with the knowledge and motivation for this research. For this, I thank you all.

Most importantly, I want to thank my wife, Dee Ann, for her love and support during this process. I am grateful for your patience as I often worked late into the evening and occasionally through the weekend. Seeing your smile at the end of the day remains my greatest motivation and source of happiness.

Finally, I thank God for taking me down this path. For this and for all of you who have supported me in this endeavor, I am forever grateful.

G. MATT BURROW

Georgia Institute of Technology
May 2012

TABLE OF CONTENTS

LIST OF FIGURES

LIST OF TABLES

LIST OF ACRONYMS AND ABBREVIATIONS

A-Beam Ambient Beam

ACR Alignment Card Range

C-Beam Central Beam

CCD Charge-Coupled Device

CL Condenser Lens

DBS Diffractive Beam Splitter

DIPCS Dense Integrated Photonic Circuits and Systems

EBL Electron-Beam Lithography

EL Expander Lens

FIB Focused Ion Beam

GDR Gridded Design Rules

IL Interference Lithography

LED Light-Emitting Diode

MBI Multi-Beam Interference

OL Objective Lens

OPD Optical Path Difference

PC Photonic Crystal

PIIES Pattern-Integrated Interference Exposure System

PIIL Pattern-Integrated Interference Lithography

PL Projection Lithography

RMS Root-Mean Square

SEM Scanning Electron Microscope

SRR Split-Ring Resonator

UV Ultraviolet

SUMMARY

In 1965, Gordon Moore, a co-founder of Intel, predicted that the number of transistors in an integrated circuit would double every two years. For more than three decades, optical lithography has enabled the semiconductor industry to meet this prediction. However, today there is serious doubt that conventional optical lithography can continue to meet the demands for decreased device sizes. New nanopatterning methods are needed. One technology being considered is interference lithography (IL).

Multi-beam interference (MBI) provides the ability to form a wide variety of sub-micron periodic optical-intensity distributions in one, two, and three dimensions. Accordingly, MBI has been used in a wide variety of application areas including nano-electronics [1-10], photonic crystals [11-20], biomedical structures [21-25], optical trapping [26-31], metamaterials [32-37], and numerous subwavelength structures [24-43]. However, a unified understanding of how MBI has been employed in each of these fields was missing from the literature. The research presented in this thesis addresses this need with a comprehensive review of MBI application areas [38], establishing the potential impact of MBI across a wide range of technologies.

As a result of the broad application of MBI, research has demonstrated numerous periodic and quasi-periodic patterns with specific space-group symmetries by careful selection of individual beam amplitudes, polarizations, and wavevector configurations [39-53]. These same parameters are also used to optimize the contrast of the resulting interference lattice, providing lithographically useful patterning possibilities [54-60]. As such, several optical configurations and lithographic techniques have been developed to

incorporate MBI, providing the potential for simple, rapid, wafer-scale, and low-cost fabrication [5,10,61-71]. In fact, a recent economic assessment of various lithography choices concluded that a multi-step method employing IL and a double-exposure technique, may be the best choice for low- to medium-volume production [2]. A new method is needed to make IL a preferred component of higher-volume commercial fabrication.

The primary objective of the research presented in this thesis is to demonstrate a new lithographic method, Pattern-Integrated Interference Lithography (PIIL) [72-76]. PIIL is the integration of superposed pattern imaging with IL. The result is a complex optical-intensity distribution composed of an MBI-defined periodic lattice modified by an integrated mask pattern image to form functional elements. To demonstrate the PIIL method, a Pattern-Integrated Interference Exposure System (PIIES) is presented that incorporates a projection imaging capability in a novel three-beam interference configuration. The purpose of this system is to fabricate, in a single-exposure step, a two-dimensional periodic photonic-crystal lattice with non-periodic functional elements integrated into the periodic pattern.

In the design of the PIIES configuration, a complete understanding of MBI patterning possibilities is required. While previous research has described the full range of translational and space-group symmetries, missing from the literature are general studies of the individual motif geometries within the unit cell of an interference pattern. This need is addressed in the present research with accurate motif geometry models for the 2D plane-group symmetries possible via linearly-polarized three-beam interference [77,78], optimized for maximum absolute contrast and primitive-lattice-vector direction

equal contrast [58]. These new models provide additional insight into MBI patterning possibilities, enable more precise analysis of MBI lattice properties for a wide range of applications, and facilitate simplified algorithms to determine the beam parameters required for the design of specific motif geometries.

In the optimized design of the specific space-group symmetries and motif geometries, most research assumes individual control over beam amplitudes and polarizations. Given the limitations of most MBI configurations this is not always possible. Without the ability to condition the key parameters of each interfering beam, it is not clear that full patterning capability remains. Furthermore, even if a particular plane-group symmetry or motif geometry is possible, it is not clear that sufficient contrast is possible for optical lithography purposes. The research presented here provides the missing analysis of constrained parametric optimization for both square and hexagonal translational symmetries [77,79]. A straightforward methodology is presented to facilitate a thorough analysis of effects of parametric constraints on interference-pattern symmetries, motif geometries, and their absolute contrasts.

With a complete understanding of MBI patterning possibilities and considerations, including the effects of parametric constraints, the design of the basic PIIES configuration is presented along with a model that simulates the resulting optical-intensity distribution at the system sample plane where the three beams simultaneously interfere and integrate a superposed image of the projected mask pattern. Appropriate performance metrics are defined in order to quantify the characteristics of the resulting photonic-crystal structure. These intensity and lattice-vector metrics differ markedly from the metrics used to evaluate traditional photolithographic imaging systems.

Simulation and experimental results are presented that demonstrate the fabrication of example photonic-crystal structures in a single-exposure step. These well-defined structures exhibit favorable intensity and lattice-vector metrics, demonstrating the potential of PIIL for fabricating dense integrated optical circuits.

Beyond the fabrication of photonic crystal structures as demonstrated in the current research, PIIL has the potential to provide a new lithographic method to allow the semiconductor industry to continue meet Moore's law predictions, while finding additional applications in an increasing variety of micro- and nano-technology fields.

CHAPTER 1

INTRODUCTION

Nothing has had a greater impact on our daily lives than microelectronics. The semiconductor revolution has enabled numerous technologies including cell phones, tablet computers, the internet, flat-panel televisions, flash memory chips, global positioning system devices, solar cells, etc. Microelectronics have had a profound impact on the fields of biomedicine, transportation, communications, entertainment, defense, environmental monitoring, and homeland security [80]. Gordon Moore, a co-founder of Intel, predicted that the number of transistors in a commercial integrated circuit would double every two years. Today there is serious doubt that conventional optical lithography, the tool of choice for more than three decades, can continue to provide a means to fabricate the decreasing device sizes required to satisfy this prediction. Efforts to reduce the wavelength of the source have not met commercial success [2]. New nanopatterning technologies are needed. Techniques being considered include 1) self-assembly approaches; 2) construction-based approaches including immersion lithography, double patterning, two-photon lithography, printing, direct writing, mask optimization, and micromanipulation; and, 3) interference lithography [2,5,9,10]. Among these approaches, interference lithography (IL), sometimes referred to in the literature as "holographic" or "interferometric" lithography, has emerged as a promising technology for relatively simple, subwavelength, and cost-effective periodic patterning in one, two and even three dimensions [1-3].

1.1 Background

1.1.1 Multi-Beam Interference

While much effort has focused on the use of IL to meet micro- and nano-electronic fabrication requirements, multi-beam interference (MBI) has found numerous additional applications outside the semiconductor industry, specifically in the fields of photonic crystals (PCs) [11-20], metamaterials [32-37], subwavelength structures [24-43], optical trapping [26-31], and biomedical structures [21-25]. Given these numerous application areas, research has provided a comprehensive understanding of MBI patterning possibilities and optimization requirements.

1.1.1.1 Two-Beam Interference

An understanding of MBI may be developed by first considering the familiar interference pattern produced by two linearly-polarized, monochromatic, plane waves derived from a common coherent source. Each plane wave may be defined by $\boldsymbol{\mathcal{E}}_{\mathrm{i}}(\mathrm{r},t) = E_{\mathrm{i}} \cos(\omega t - \mathbf{k}_{\mathrm{i}} \cdot \mathbf{r} + \phi_{\mathrm{i}})\hat{\mathbf{e}}_{\mathrm{i}}$, where E_i is the amplitude, ω is the radian frequency, $\mathbf{k}_{\mathrm{i}}$ is the wavevector, ϕ_{i} is the phase, $\hat{\mathbf{e}}_{\mathrm{i}}$ represents the linear polarization vector, and i = 1,2. When the two plane waves interfere, a one-dimensional (1D) fringe pattern is produced with a periodicity, Λ, directly proportional to the wavelength, λ, and inversely proportional to the sine of the common wavevector incidence angle, θ, with respect to the z axis as depicted in Fig. 1.1.

The total time-independent intensity distribution, $I_T(\mathbf{r})$, at the intersection of the two waves is expressed as the absolute square of the sum of the amplitudes,

$I_T(\mathbf{r}) = \left|\boldsymbol{\mathcal{E}}_1(\mathbf{r}) + \boldsymbol{\mathcal{E}}_2(\mathbf{r})\right|^2$. For the wavevector configuration depicted in Fig. 1.1, the total intensity distribution may be given by

$$I_T(\mathbf{r}) = I_o\left[1 + \frac{E_1 E_2(\hat{\mathbf{e}}_1 \cdot \hat{\mathbf{e}}_2)}{I_o}\cos\left(k_o 2\sin\theta\,\hat{y} + \phi_1 - \phi_2\right)\right], \tag{1.1}$$

where $k_o = 2\pi/\lambda$ and a DC intensity term, $I_o = 1/2\left(E_1^2 + E_2^2\right)$, is introduced. From Eq. (1.1), we see that the spatial-cosine term describes a 1D periodic pattern that varies along the *y* axis with a periodicity of $\Lambda = \lambda/2\sin\theta$ as depicted in Fig. 1.1.

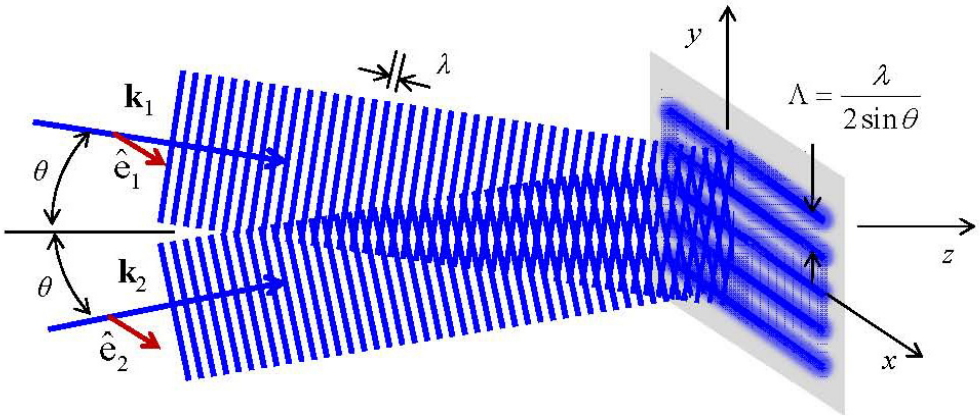

Figure 1.1: Two-beam interference. An interference fringe with a periodicity, Λ, is formed by two linearly-polarized, monochromatic, plane waves. In this example $\mathbf{k}_1$ and $\mathbf{k}_2$ are contained in the *y*-*z* plane at an angle, θ, with respect to the *z* axis [81].

1.1.1.2 N-Beam Interference

For *N* interfering beams, the general form of the total time-independent intensity distribution, $I_T(\mathrm{r})$, may be given as

$$I_T(\mathrm{r}) = I_o\left\{1 + \sum_{\mathrm{j>i}}^{N} V_{\mathrm{ij}}\cos\left[\left(\mathbf{k}_\mathrm{j} - \mathbf{k}_\mathrm{i}\right)\cdot\mathbf{r} + \phi_\mathrm{i} - \phi_\mathrm{j}\right]\right\}, \tag{1.2}$$

where I_o is now $\frac{1}{2}\sum_{\mathrm{k=1}}^{N}\left(E_\mathrm{k}^2\right)$, and an interference coefficient, V_{ij}, is defined as [59]

$$V_{ij} = \frac{E_i E_j \left(\hat{\mathbf{e}}_i \cdot \hat{\mathbf{e}}_j\right)}{I_o}. \tag{1.3}$$

In Eq. (1.2), we see that every beam-pair combination produces a fringe pattern, each defined by a spatial-cosine term with magnitude V_{ij}, that contributes to the overall periodic optical-intensity distribution. The orientation and periodicity of these 1D fringe patterns are determined by the relative beam-pair wavevector configurations and angles of incidence, while the relative phase difference determines the position of the fringes along the dimensional axis. In general, three-beam interference produces up to three 1D fringe patterns that combine to form a two-dimensional (2D) optical-intensity distribution as depicted in Fig. 1.3. Four-beam interference provides three-dimensional (3D) patterning with up to six interfering beam pairs. Increasingly complex designs are realized as the number of interfering beams increases and elliptical or circular beam polarizations are considered.

In three-beam interference, the wavevector configuration to produce a desired 2D translational symmetry is found by first calculating the reciprocal lattice vectors

$$\mathbf{A} = 2\pi \frac{\mathbf{b} \times \hat{\mathbf{z}}}{\mathbf{a} \cdot \mathbf{b} \times \hat{\mathbf{z}}} \text{ and } \mathbf{B} = 2\pi \frac{\hat{\mathbf{z}} \times \mathbf{a}}{\mathbf{a} \cdot \mathbf{b} \times \hat{\mathbf{z}}}, \tag{1.4}$$

where **a** and **b** represent the primitive basis vectors of the lattice formed in the *x*-*y* plane as the pattern remains invariant along the *z* axis as depicted in Fig. 1.2(a). The required recording wavevectors are then calculated as depicted in Figs. 1.2(b) and (c) by finding the circumcenter vector, **P**, of the triangle defined by the two reciprocal lattice vectors, **A** and **B**, by

$$\mathbf{P} = \frac{1}{2} \frac{|\mathbf{A}|^2 \left(\mathbf{B} \times \hat{\mathbf{z}}\right) + |\mathbf{B}|^2 \left(\hat{\mathbf{z}} \times \mathbf{A}\right)}{\mathbf{A} \cdot \mathbf{B} \times \hat{\mathbf{z}}}. \tag{1.5}$$

The projection of the wavevectors on the *x*-*y* plane are then defined by

$$\mathbf{k}_{1,xy} = -\mathbf{P}, \mathbf{k}_{2,xy} = \mathbf{A} - \mathbf{P}, \text{ and } \mathbf{k}_{3,xy} = \mathbf{B} - \mathbf{P}. \tag{1.6}$$

The *z* component of each wavevector is determined by

$$\left|\mathbf{k}_i\right| = nk_o, \tag{1.7}$$

where $k_o = 2\pi/\lambda$ and n is the index of refraction of the recording medium [82]. The resulting wavevector configuration for a hexagonal lattice is depicted in Fig. 1.2(d).

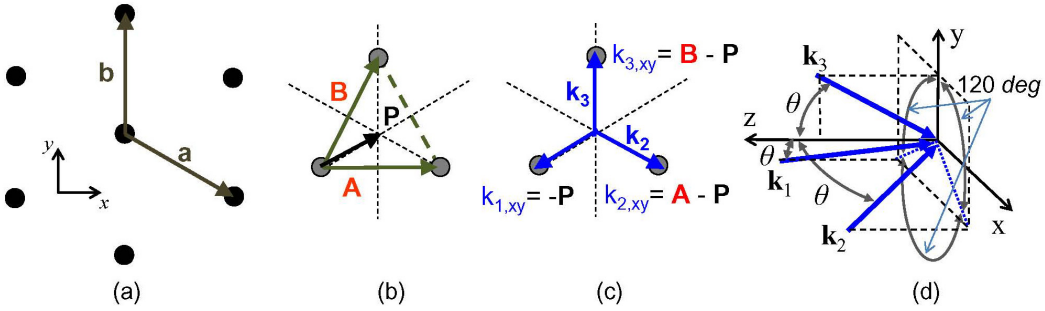

Figure 1.2: Determination of recording wavevectors for a hexagonal lattice. (a) A hexagonal lattice is defined by the primitive basis vectors **a** and **b**. (b) The triangle defined by the two reciprocal lattice vectors, **A** and **B**, determines the circumcenter vector, **P**. (c). The projections of the wavevectors on the *x*-*y* plane are determined by the relationships between **P**, **A**, and **B**. (d) The resulting wavevector configuration consists of $\mathbf{k}_3$ contained in the *y*-*z* plan and $\mathbf{k}_1$ and $\mathbf{k}_2$ arranged such that the projections of all three vectors are separated by exactly $120 deg$ in the *x*-*y* plane.

The geometry of the unit cell within the periodic pattern further defines the space-group symmetry as determined by the amplitude and polarization of the individual beams. Specifically, the magnitude of each interference coefficient, as defined by Eq. (1.3), is proportional to the product of the amplitudes, $E_i E_j$, and the dot product of the polarization vectors, $\hat{\mathbf{e}}_i \cdot \hat{\mathbf{e}}_j$, for each beam pair. The interference coefficient for each spatial cosine term, in turn, determines the contrast and relative contribution of each beam-pair fringe pattern to the overall periodic distribution. The significance of the individual beam polarizations is demonstrated in square-lattice pattern depicted in

Fig. 1.3. By adjusting the relative linear polarizations of the beams defined by $\mathbf{k}_1$ and $\mathbf{k}_2$, the interference coefficient, V_{12}, may be set to a zero value when the two polarization vectors are mutually orthogonal, thereby eliminating the fringe pattern of Fig. 1.3(d) altogether. In this case, assuming equal contrast for the two remaining fringe patterns ($V_{13} = V_{23}$), a square lattice is formed with *p4m* plane-group symmetry as depicted in Fig. 1.3(e). Alternatively, for the same wavevector configuration, the relative polarizations may be selected such that all three interference coefficients are equal ($V_{12} = V_{13} = V_{23}$), again combining to form a square lattice, but now with *cmm* plane-group symmetry as depicted in Fig. 1.3(f). In fact, for the wavevector configuration depicted in Fig. 1.3(a), the interference coefficients may be selected to produce two additional plane-group symmetries, *pmm* and *p2*.

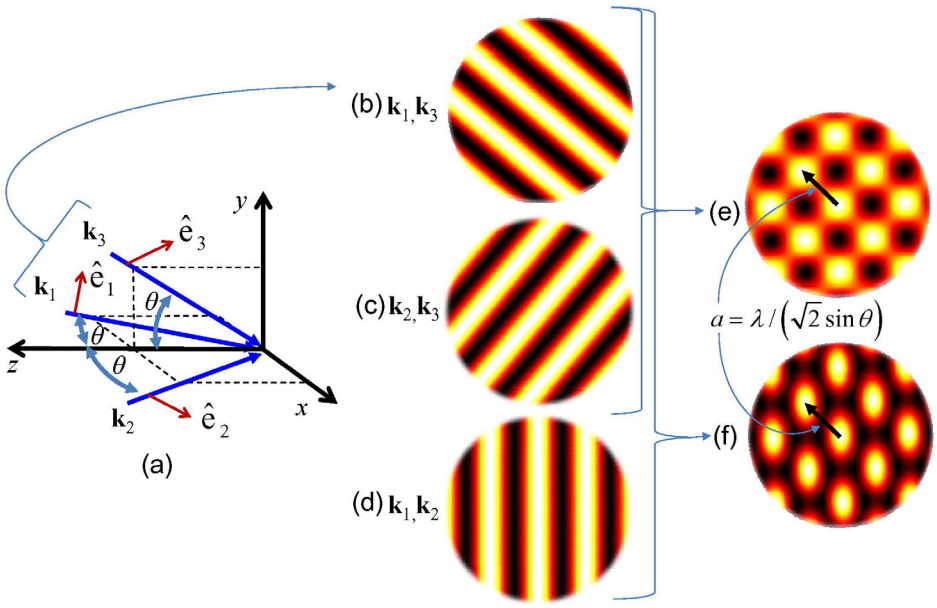

Figure 1.3: Three-beam interference. (a) Three beams defined by $\mathbf{k}_1$, $\mathbf{k}_2$, and $\mathbf{k}_3$ interfere at the *x*-*y* plane at a common angle of incidence, θ, with respect to the *z* axis. The beam pairs defined by (b) $\mathbf{k}_1$ and $\mathbf{k}_3$, (c) $\mathbf{k}_2$ and $\mathbf{k}_3$, and (d) $\mathbf{k}_1$ and $\mathbf{k}_2$ form three distinct 1D interference-fringe patterns. (e) The fringes patterns of $\mathbf{k}_1$ and $\mathbf{k}_2$ and $\mathbf{k}_1$ and $\mathbf{k}_3$ combine to form a square lattice with *p4m* plane-group symmetry. (f) The fringe pattern of $\mathbf{k}_1$ and $\mathbf{k}_2$ combine with the other two fringe patterns to form a square lattice with *cmm* plane-group symmetry.

By careful selection of the wavevector configurations, beam amplitudes, and beam polarizations, research has demonstrated the ability to create all 2D Bravais lattices [39], five of seventeen 2D plane-group symmetries [42], and all 3D Bravais lattices via single- [40,43,45,46] and multiple-exposure [41,44] techniques. If elliptical polarization is allowed for the individual beams, four additional 2D plane-group symmetries have been demonstrated for a three-beam configuration [42]. Figure 1.4(a) demonstrates a 2D hexagonal lattice with *p6m* plane-group symmetry formed by three-beam interference. Figure 1.4(b) depicts a 3D face-centered-cubic lattice formed by four-beam interference. When the phase of the individual beams is considered, additional control over the interference pattern is possible. For patterns created by four or fewer linearly polarized beams, a change to the relative phase translates the interference pattern according to the translational symmetry. If more beams are added, the relative phase difference of the beam pairs will further define the unit cell structure leading to increasingly complex patterning possibilities and space-group symmetries [45,47,83,84]. As an example, a 2D honey-comb structure formed by six-beam interference is depicted in Fig. 1.4(c). Alternatively, a phase shift may be introduced by elliptical polarization in one or more of the interfering beams to produce compound lattices formed by as few as four beams [85-87]. Other quasi-periodic patterns demonstrated using MBI include 2D structures with 5-, 10-, 12-, and 60-fold symmetries [88,89]; connected *fcc*-like lattices [90]; chiral-basis [87] and icosahedral [91] structures; and, Archimedean-tiled and Penrose lattices [89].

1.1.1.3 Motif Geometry

The translational periodicity, together with the space-group symmetry of the periodic patterns, determine the geometry of the individual lattice points, or motifs, created by MBI [92]. In some cases, the motif geometry plays a significant role in the performance characteristics of a device fabricated using MBI. For example, the lattice point geometry has been shown to affect the photonic-bandgap characteristics in PCs [48-50,52,53,93-103], selective plasmonic excitation in plasmonic crystals [104], PC laser beam pattern [105] and polarization-mode control [106], birefringence of PC fibers [107], cell behavior in tissue engineering [25], tuning of surface textures [108], magnetization switching in periodic magnetic arrays [109], and negative refraction and superlensing in metamaterials [51,110].

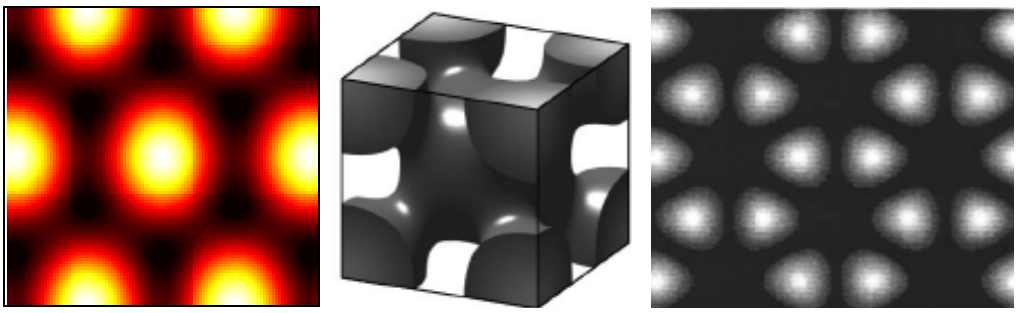

(a) (b) (c)

Figure 1.4: Multi-beam interference patterning. (a) A two-dimensional hexagonal lattice has *p6m* plane-group symmetry. (b) A three-dimensional pattern forms a body-centered-cubic lattice [58]. (c) A two-dimensional pattern forms a honey-comb structure [47].

Based on the significance of motif geometries in periodic lattices, numerous studies report analytical and computational methods to model and analyze the effects of motif orientation and shape for each of the application areas. In most cases, motif geometries are assumed to be circular [50,97,98,106], elliptical [50,94,95,101,102,106,110,111], square [50], rectangular [50,101], triangular[112] with rounded corners [99], rhombic

[107], or hexagonal [48,101]. However, these assumptions are not entirely accurate. In fact, the motif shape in a 2D periodic pattern formed by three-beam interference may change between an ellipse and a rhombus or an ellipse and a hexagon as a function of the radial distance from the center of the motif corresponding to an intensity maxima (or minima). As technologies continue to rely on MBI for micro- and nano-scale patterning, accurate analytical models are required to describe MBI motif geometries. This will provide valuable insight into patterning possibilities and enable more precise analysis and optimization of interference lattices for use across the full range of application areas.

Without an accurate analytical model to describe MBI motifs, researchers are often required to analyze the intensity distribution given by Eq. (1.2) [50,51,100]. These methods typically require the interference coefficients, defined by Eq. (1.3), to be adjusted systematically and then analyzed based on the desired characteristics of the resulting intensity distribution for a given application. Once an optimal set of interference coefficients is obtained, beam parameters are then determined as required to generate the coefficients for the desired pattern [48,49,52,53]. As an example, one recent report indicates that the photonic bandgap for a square PC lattice may be improved by optimizing the shape of the individual motifs to an "elliptical-like" geometry with *p2* plane-group symmetry as depicted in Fig. 1.5 [52]. In this example, the relative photonic bandgap was improved from an initial value of 2.60% to 9.68% using a Nelder-Mead simplex iteration algorithm. In this algorithm, an arbitrary set of interference coefficients were used to produce an initial intensity distribution, resulting in a binary representation of the pattern as depicted in Fig. 1.5(a). The photonic bandgap for this pattern was then determined by analyzing the photonic dispersion curve for the PC lattice as depicted in

Fig. 1.5(b). The interference coefficients were then adjusted according to the algorithm procedures, and the new binary pattern was analyzed. After 134 iterations of the algorithm, an optimized motif geometry and improved relative photonic bandgap was obtained as depicted in Figs. 1.5(c) and (d). Methodologies such as these are computationally expensive and experimentally prohibitive. Given an accurate model to describe MBI motif geometries, analysis could be conducted directly using the analytical model without the requirement to solve and analyze the intensity distribution. Once an optimal motif geometry is obtained, the beam parameters could then be determined directly. This methodology would provide simplified optimization algorithms and enhance the development of MBI-enabled applications.

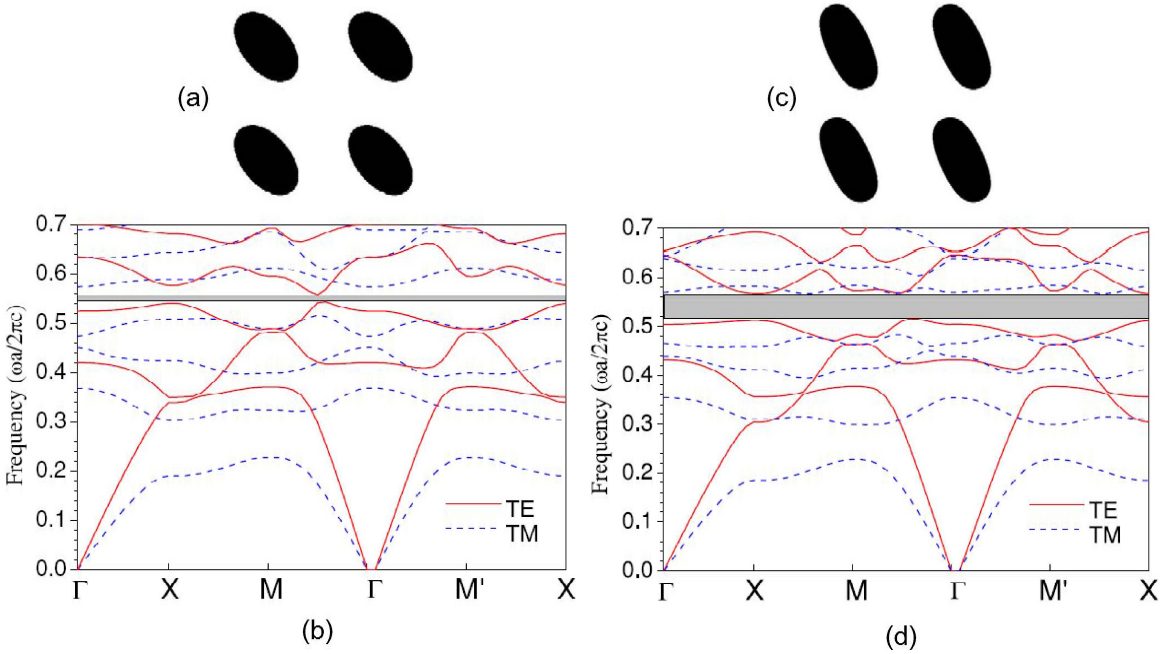

Figure 1.5: Motif geometry considerations in a PC square-lattice photonic bandgap. (a) An initial binary pattern depicts elliptical rods. (b) The resulting photonic dispersion curve exhibits a relative photonic bandgap of 2.60%. (c) The optimized binary pattern depicts "elliptical-like" rods. (d) The resulting photonic dispersion curve exhibits an improved relative photonic bandgap of 9.68% [52]. In the photonic dispersion curves, ω is the radian frequency, a is the lattice constant, c is the velocity of light in vacuum, TE represents the transverse-electric mode, TM represents the transverse-magnetic mode, and Γ, X, and M are the irreducible Brillouin zone symmetry points.

1.1.1.4 Optimization

Given the numerous periodic patterning possibilities afforded by MBI, significant research has focused on maximizing the absolute contrast of the interference pattern by optimized selection of individual beam amplitudes, polarizations, and phases [54,56,60,113-117]. The absolute contrast, often called "fringe visibility" or "fringe contrast" in the literature, is defined as

$$\mathrm{V}_{\mathrm{abs}} = \frac{I_{\max} - I_{\min}}{I_{\max} + I_{\min}}, \tag{1.8}$$

where I_{max} and I_{min} are the maximum and minimum values of the intensity distribution given by Eq. (1.2). In this effort, the concept of uniform contrast was first introduced, in which the relative amplitudes and individual-beam polarizations are optimized to ensure the highest contrast of the pattern as a whole for three- [55,118,119] and four-beam interference [57,120]. To find the optimal set of polarization vectors for a given three-beam wavevector configuration, a mathematical method was developed to solve for the conditional maximum of the function [55]

$$\begin{aligned} &f\left(l_1', m_1', n_1', \ldots, l_3', m_3', n_3', \lambda_1, \ldots, \lambda_6\right) \\ &\quad = V + \sum_{j=1}^{3} \lambda_j \left(l_j'^2 + m_j'^2 + n_j'^2\right) + \sum_{j=1}^{3} \lambda_{j+3} \left(l_j l_j' + m_j m_j' + n_j n_j'\right), \end{aligned} \tag{1.9}$$

where l_j, m_j, and n_j are the three normalized direction cosines for the corresponding wavevectors, l'_j, m'_j, and n'_j are the normalized direction cosines for the polarization vectors, λ_i are Lagrangian multipliers, and V is the common uniform interference coefficient. This common interference coefficient, derived from Eq. (1.3), is required for optimized uniform contrast and is defined as

$$V = V_{12} = V_{13} = V_{23} = \frac{2e_{12}e_{13}e_{23}}{e_{12}^2 + e_{13}^2 + e_{23}^2}, \tag{1.10}$$

where

$$e_{ij} = \hat{e}_i \cdot \hat{e}_j \tag{1.11}$$

is the polarization efficiency factor [55].

More recently, the conditions for primitive-lattice-vector-direction equal contrasts provided a complete treatment of contrast considerations in three- [59] and four-beam interference [58,82]. When applied to three-beam interference, the conditions for primitive-lattice-vector-direction equal contrasts require individual control over each recording wavevector, beam amplitude, and beam polarization to produce an interference pattern with maximized absolute contrast and uniform contrast in the primitive-lattice-vector directions. In this method, a symbolic designation, $\pm C_n^{(m)}$, was introduced, where the quantity n is the total number of interfering beams, m *is* the number of contributing interfering beam pairs, and the sign indicates whether an intensity maxima (+) or minima (–) is located at a lattice point.

For the $\pm C_3^{(2)}$ case, this symbolic designation implies that only two sets of interfering beam pairs contribute to the interference pattern created using three-beam interference as depicted in Fig. 1.3(e). Under the conditions for primitive-lattice-vector-direction equal contrasts, the initial constraints on interfering beam amplitudes and polarizations are [59]

$$e_{12} = 0, \tag{1.12}$$

and

$$E_2 = \frac{e_{13}}{e_{23}} E_1. \tag{1.13}$$

Under these constraints, Eq. (1.3) simplifies to

$$V = \frac{E_1 E_3 e_{13} e_{23}^2}{E_3^2 e_{23}^2 + E_1^2 e_{23}^2 + E_3^2 e_{13}^2}. \tag{1.14}$$

These conditions may be satisfied when the beam amplitudes and polarizations are chosen such that

$$V_{13} = V_{23} = \frac{e_{13} e_{23}}{\sqrt{e_{13}^2 + e_{23}^2}}, \tag{1.15}$$

and

$$V_{12} = 0. \tag{1.16}$$

Of course, it is also possible to set V_{13} or V_{23} to zero and satisfy $C_3^{(2)}$ requirements. For the purposes of the proposed research, only the above derivation will be used. The resulting optimized electric field ratios are then

$$E_1 = \frac{e_{23}}{\sqrt{e_{13}^2 + e_{23}^2}} E_3, \tag{1.17}$$

and

$$E_2 = \frac{e_{13}}{\sqrt{e_{13}^2 + e_{23}^2}} E_3. \tag{1.18}$$

For the $C_3^{(3)}$ case, this symbolic designation implies that all three interfering beam pairs contribute equally to the interference pattern as depicted in Fig. 1.3(f). Under the conditions for primitive-lattice-vector-direction equal contrasts, the constraints on interfering beam amplitudes and polarizations are [59]

$$E_1 = \frac{e_{23}}{e_{12}} E_3, \tag{1.19}$$

and

$$E_2 = \frac{e_{13}}{e_{12}} E_3. \tag{1.20}$$

Under these constraints, Eq. (1.3) simplifies to

$$V = \frac{2e_{12}e_{13}e_{23}}{e_{12}^2 + e_{13}^2 + e_{23}^2}. \tag{1.21}$$

Finally, the conditions for $\pm C_3^{(3)}$ may be satisfied when the beam amplitudes and polarizations are chosen according to Eq. (1.10).

For a hexagonal lattice with *p6m* plane-group symmetry, the conditions for $\pm C_3^{(3)}$ must be applied. Similarly, $\pm C_3^{(2)}$ conditions are required for square lattices with *p4m* plane-group symmetry, as well as patterns with *pmm* symmetry. Either $\pm C_3^{(3)}$ or $\pm C_3^{(2)}$ conditions may be applied to achieve *cmm* symmetry depending on the translational symmetry. The lowest order symmetry, *p2,* is possible, without constraints, for general three-beam interference. Figure 1.6 depicts the conditions for all five of the plane-group symmetries possible using linearly-polarized three-beam interference. As constraints are placed on the primitive basis vectors and interference coefficients, higher-order symmetries are realized.

By applying the conditions for $\pm C_n^{(m)}$ and maximizing absolute contrast to determine the required individual beam parameters, a high-quality, lithographically useful interference pattern is possible. Using this methodology, it is shown that unity absolute contrast, $V_{abs} = 1$, can always be achieved for a square lattice with *p4m* plane-group symmetry. For the hexagonal lattice with *p6m* plane-group symmetry, unity absolute contrast can only be achieved when intensity minima are located at the lattice points, satisfying the $-C_3^{(3)}$ conditions. For the $+C_3^{(3)}$ case, V_{abs} varies from a maximum of unity absolute contrast (when all three recording wavevectors are collinear or coplanar) to a minimum optimized absolute contrast of $V_{abs} = 0.6$ (when all three recording wavevectors are orthogonal) [69,71].

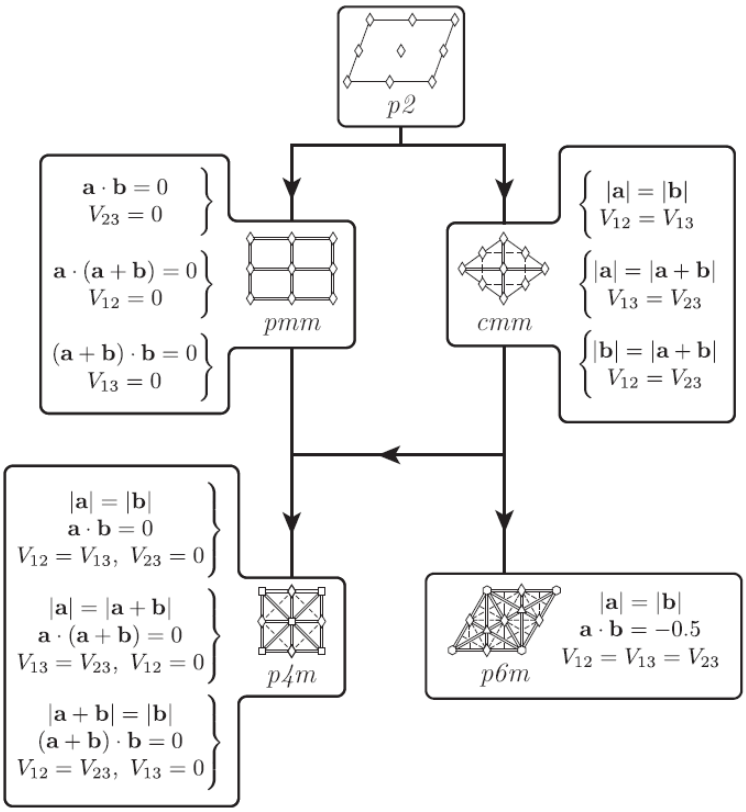

Figure 1.6: Conditions for primitive-lattice-vector-direction equal contrasts in linearly-polarized, three-beam interference. The lowest order symmetry, *p2*, is possible, without constraints, for general three-beam interference. As constraints are placed on the interference coefficients, V_{ij}, and primitive basis vectors, **a** and **b**, higher-order symmetries are realized [82].

While these conditions assume individual control over beam amplitude and polarization, recent research suggests that sufficient contrast may still possible, even when beam parameters are perturbed [86]. In one study, the effects of a single linear polarization was analyzed for a system of cube beamsplitters and right-angle prisms used to generate three interfering beams from a common linearly polarized source [121]. However, this study was limited to a 2D hexagonal lattice. Missing from the literature is a general methodology and study of the effects of amplitude and polarization constraints on the full range of MBI patterning possibilities in linearly-polarized three-beam

interference. This information is required to ensure that a specific MBI configuration can meet the requirements for a given application.

1.1.2 Multi-Beam Interference Configurations

Numerous optical configurations have been employed to generate the multiple beams required for MBI with varying levels of control over beam parameters, interferometric stability, and coherence requirements. These configurations may be broadly categorized as amplitude-splitting or wavefront-dividing methodologies.

1.1.2.1 Amplitude-Splitting Configurations

Amplitude-splitting configurations typically split the single common source beam into two or more beams through the use of beam splitters or diffractive elements. The beams are then directed to intersect at the plane of interference through the use of mirrors, lens, and/or prisms. An example two-beam configuration to record a 1D grating utilizing a single beam splitter and beam-directing mirrors is depicted in Fig. 1.7(a). In any two-beam configuration, multiple exposures are required to generate more complex 2D and 3D patterns in a photo-sensitive material [122-125]. This requirement is often satisfied by incorporating a rotating sample stage at the recording plane [126-129]. More advanced amplitude-splitting systems, such as the configuration depicted in Fig. 1.7(b), allow for the single-exposure of multiple beams [130,131]. Ideally suited for research and development, these configurations often afford the option of individual control over beam amplitude, polarization, and phase. They may also be reconfigured easily for a wide range of wavevector configurations and incidence angles [132,133]. For example, using an argon-ion laser source of $363.8\,nm$, the configuration in Fig. 1.7(b) can produce

five of the seventeen 2D plane-group symmetries with a lattice constant ranging from approximately $3.5\,\mu m$ down to $300\,nm$.

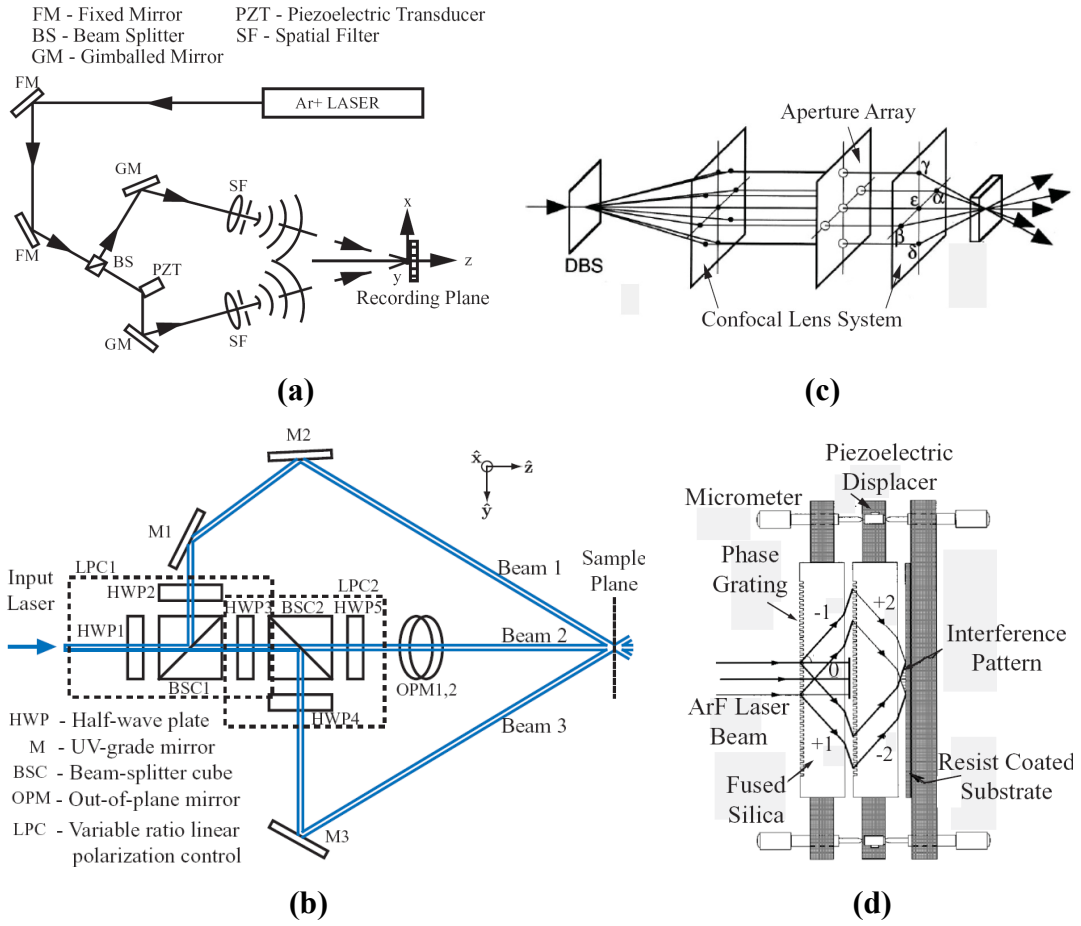

Figure 1.7: Amplitude-splitting MBI configurations. (a) Two-beam configuration used to record a subwavelength polarization-dependent reflection grating [61]. (b) Three-beam MBI configuration for single-exposure 2D patterning with individual control of beam amplitude and polarization [69]. (c) Five-beam MBI configuration for single-exposure patterning with a diffractive beam splitter (DBS) and a confocal lens system [63]. (d) Cascaded diffractive elements implement monochromatic IL [68].

Other amplitude-splitting configurations have been developed that rely on gratings to diffract a single incident beam into two or more beams. These beams are, in turn, focused onto the plane of interference by either a lens system as depicted in Fig. 1.7(c) [63,120], beam-directing mirrors [89,134], or cascaded diffractive elements [135,136] such as the monochromatic IL configuration depicted in Fig. 1.7(d) [68]. The symmetries

formed by the zero- and first-order diffracted beams in Fig. 1.7(c) make this configuration particularly useful in implementing the much-studied five-beam umbrella configuration consisting of a central beam (C-beam) surrounded by four symmetric ambient beams (A-beams) [117,137-140]. For an umbrella configuration, this scheme is particularly useful if the individual beams require specific conditioning, such as different polarizations (e.g. circularly polarized C-beam and linearly polarized A-beams) [141] or phase control [89].

1.1.2.2 Wavefront-Dividing Configurations

To simplify opto-mechanical configurations, wavefront-dividing schemes have been developed that divide portions of a single expanded source beam into the multiple beams required for MBI. The most common wavefront-dividing configuration incorporates a Lloyd's mirror to reflect a portion of an expanded source beam to intersect with the transmitted portion as depicted in Fig. 1.8(a). As early as 1985, a Lloyd's mirror configuration was used as a simple way to fabricate linear grating couplers [142]. Again, multiple exposures are required with this configuration to produce 2D and 3D patterns [143]. One recent report demonstrated a Lloyd's mirror capable of producing three beams with $120 deg$ symmetry [144]. A Lloyd's mirror configuration may also be combined with immersion lithography, further reducing the fringe pattern periodicity to the sub-$100 nm$ range [145].

A second common wavefront-dividing configuration incorporates a prism designed to divide and refract a single expanded beam into multiple beams as depicted in Fig. 1.8(b) [146-148]. This prism-based method is particularly useful in implementing the umbrella configuration, with expanded options for four or more beams [149]. By

selecting a prism with a refractive index matching that of the recording material, refraction-induced asymmetries may be mitigated at the at the prism-sample-plane interface. In fact, an index-matching prism element may also be used in amplitude-splitting configurations, incorporated at the sample plane, to mitigate these same asymmetries, including changes to the individual beam polarizations at the air-photoresist interface [16,89,150].

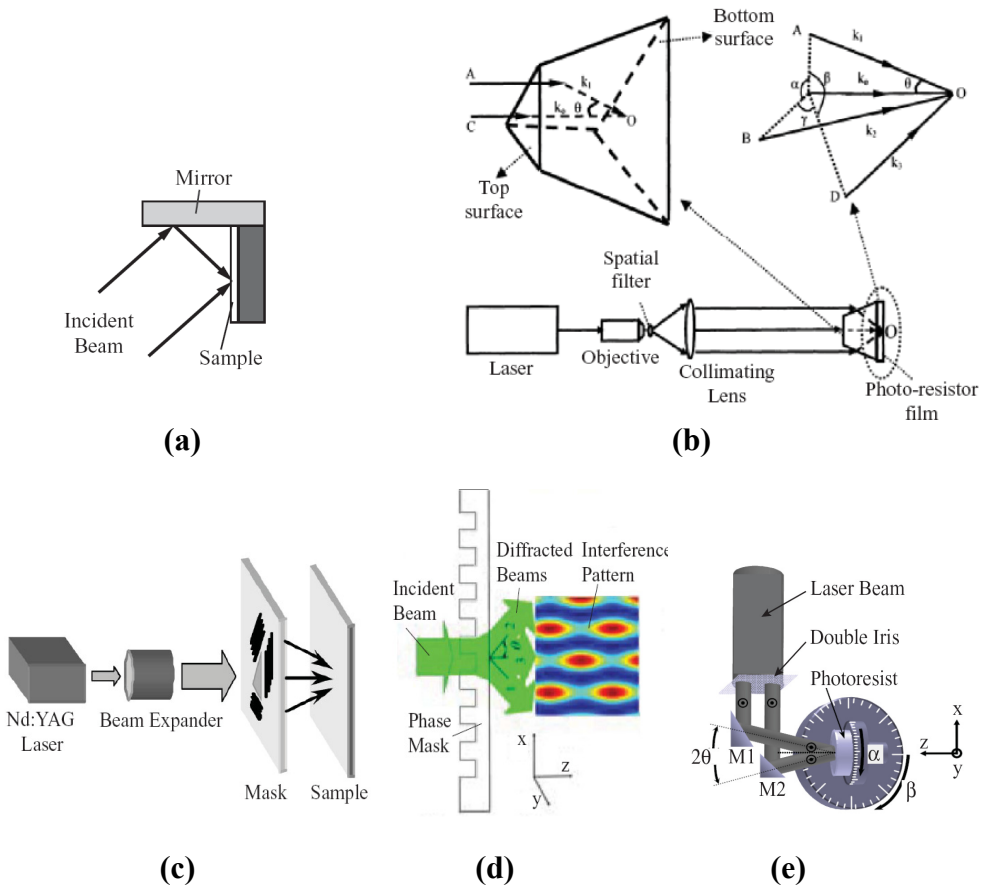

Figure 1.8: Wavefront-dividing MBI configurations. (a) Lloyd's mirror configuration reflects a portion of the incident beam onto the transmitted beam at the sample. (b) A prism is used to divide and refract different portions of an incident collimated beam to produce four-beam umbrella interference [70]. (c) A diffractive-grating mask divides portions of the incident expanded beam such that the first-order diffracted beams intersect and interfere at the sample plane [62]. (d) A 1D phase mask diffracts the incident beam into +1, 0, and −1 orders to create a near-field interference pattern [66] (e) A double-iris amplitude mask defines two MBI beams from a single collimated source for multiple two-beam interference patterning [65].

Diffractive gratings may also be used in a wavefront-dividing scheme in the form of a single diffractive photo-mask. In this configuration, two or more gratings are typically used to diffract a single expanded beam, such that the first order diffracted beams intersect and interfere at the sample plane as depicted in Fig. 1.8(c) [62,151-155]. In one report, multiple gratings with controlled periods were used to produce compound periodic patterns with a large depth of focus using an achromatic source [83]. If an umbrella configuration is required, the zero-order diffracted beam from a diffractive photo-mask may function as the C-beam [156].

A fourth option for wavefront dividing places a photo-mask with a single diffractive optical element in close proximity to the sample plane to produce a near-field self-interference pattern of the zero-, positive-, and negative-diffracted orders as depicted in Fig. 1.8(d) [157-161]. In this example, a 1D phase mask diffracts the incident beam into three interfering beams at the exit of the mask. Multiple exposures of a 1D phase mask may be used to produce complex 3D periodic patterns, such as a woodpile-type structure [66,162]. Alternatively, a multi-layer mask with two orthogonal diffractive gratings [163-165] or a single 2D diffractive optical element [166-169] may be used to produce multiple beams with a single exposure.

Finally, a fifth wavefront-dividing option is depicted in Fig. 1.8(e) that employs a double-iris amplitude mask to define the individual beams, while providing the opportunity for individual beam conditioning and wavevector control [65,170,171].

For each of the MBI configurations, there are varying levels of control over beam parameters, interferometric stability, and coherence requirements. A detailed comparison

of each configuration is given in Table 1.1. For the first three amplitude-splitting configurations, even-symmetry reflections or diffractions as depicted in Figs. 1.7(a), (c), and (d) may be used to resolve transverse coherence issues, assuming any beam offset is within the transverse coherence length and the spatial coherence meets depth of focus requirements [1,172]. However, a common drawback of beam-splitting-based configurations is the potential for interferometric instability. Any perturbations to the optical components, optical path lengths, or relative phases of the interfering beams may result in a translation of the pattern or change in the symmetry of the unit cell. Thus, pattern stability is generally low for amplitude-splitting schemes. Of the three amplitude-splitting configurations only a multiple-beam-splitting configuration, such as the three-beam interference system depicted in Fig. 1.7(b), provides the ability to reconfigure easily the individual beams for a wide range of lattice constants and translational symmetries, while allowing for individual control over beam parameters.

As a result of the relatively short optical path lengths for the diffracted beams in wavefront-dividing configurations, these methods are essentially phase-locked, representing the most interferometrically stable option for MBI. However, with this advantage does come some disadvantages. In most wavefront-dividing schemes, control over individual beam amplitudes and polarizations is typically limited, wavevector configurations are generally fixed, and each is sensitive to transverse incoherence. As an exception, the amplitude-mask-based system can be configured to allow for individual beam control and conditioning. However, this added flexibility comes at the expense of interferometric pattern stability, and transverse coherence issues remain.

Table 1.1: Comparison of MBI configurations.

Configuration	Configuration Characteristics				
	High Temporal Coherence?	Stabile Pattern?	Reconfigurable?	Individual Beam Conditioning?	Full Patterning Possibilities?
Multiple Beam Splitters	Yes	No	Yes	Yes	Yes
Diffractive Beam Splitter	Yes	Marginal	No	Amplitude Only	?
Cascaded Diffractive Elements	Yes	Marginal	No	No	?
Lloyd's Mirror	No	Yes	No	No	?
Prism	No	Yes	No	No	?
Diffractive Grating Mask	No	Yes	No	Amplitude Only	?
Phase Mask	No	Yes	No	No	?
Amplitude Mask	No	No	Yes	Yes	Yes

Even though most of the MBI configurations are not easily reconfigured, they may all be designed to provide a wide range of periodicities and translational symmetries based on wavevector configurations. However, it is not clear that full patterning capabilities remain as constraints are placed on beam amplitudes and polarizations. Furthermore, even if a particular plane-group symmetry is possible, it is not clear that sufficient contrast is attainable for optical lithography purposes. Accordingly, a thorough understanding of parametric constraints is required.

1.1.3 Interference Lithography

As early as 1970, the fringe patterns formed by two-beam interference were recorded in photoresist, forming a simple, reproducible diffraction grating for use in thin-film

waveguides [173]. Two decades later, multiple two-beam IL exposures were proposed to generate more complex 2D patterns in a photoresist [4]. Since then, a wide range of structures have been recorded via IL using near-infrared [7,168,174-176], visible light [21,47,54,63,93,94,177-186], ultraviolet (UV) [19,20,54,64,69,123,124,155,187-190], deep-UV [6,68,143,176,191,192], and extreme-UV sources [193-196].

Today, IL is considered a potentially key enabling technology for the ever-increasing demand for smaller feature sizes in optical lithography [1-3]. Modern integrated circuits have very regular layouts with an underlying grid pattern that defines the smallest feature size in the integrated circuit. IL can be used to define this underlying periodic or quasi-periodic grid-based structure. In this application, IL has the advantages of 1) simple optics, 2) large working distances, 3) fast processing, 4) low cost, and 5) high resolutions [2,89,197-199].

A wide array of photosensitive materials have been used to record the interference patterns formed by IL including positive resists [18,19,155], negative resists [69,200], hybrid organic-inorganic materials [194,201,202], extreme-UV photoresists [203], silsesquioxane-based photoresists [168], holographic polymer-dispersed liquid crystals [204], amorphous-chalcogenide-semiconductor thin films [205], titanium-containing monomer films [206], red-sensitive photopolymers [179], polyimide foils [108], biocompatible polymers [25], oligomer films [21], and even silica [207] and chalcogenide [208] glasses. In the most general terms, given sufficient optical intensity, an interference pattern may be recorded in or on any material that responds to laser illumination at a given wavelength [190], to include direct writing on metallic surfaces

via laser interference metallurgy [209] and direct laser interference patterning of π-conjugated polymers [210].

The primary drawback to IL is the inherent limitation to periodic patterning. Research is now focused on ways to incorporate IL into commercial applications, combining MBI with other conventional lithographic processes to produce functional integrated devices. For example, to create functional elements in the periodic pattern defined by IL, a second lower spatial-frequency trim exposure may be used to define the non-periodic features using a conventional technique, such as projection lithography (PL). This helps overcome the diffraction limitations of using PL alone [5,10,211]. Figure 1.9(a) depicts a hybrid optical maskless lithography technique demonstrating the use of two-beam interference to form vertical fringes, followed by a second traditional low-pitch PL trim exposure [192]. Similarly, Fig. 1.9(b) demonstrates a multi-step procedure to create more complex composite patterns.

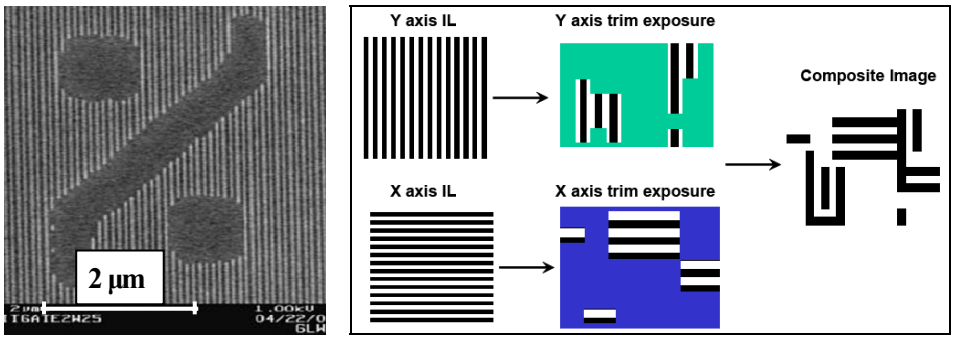

(a) (b)

Figure 1.9: Interference lithography (IL) combined with projection lithography (PL). (a) Scanning electron microscope image of the combined use of IL and PL techniques. Here, 45 *nm* grid lines were produced via two-beam IL. Next, the higher-spatial-frequency modulating pattern was recorded via PL [5]. (b) A complex composite pattern is created by two IL exposures and two PL trim exposures [10].

Others have combined IL with various lithographic techniques including electron-beam lithography (EBL) [127,212,213], electron-beam-induced deposition [214], focused

ion beam (FIB) lithography [188,215], direct laser writing [123,184,216,217], atomic force microscopy nano-indentation [218], and multi-photon polymerization [219-221]. For each of these combinational techniques, multiple exposures and processes are required to create the functional elements in the MBI-defined periodic pattern. This, in turn, increases the complexity and cost of incorporating IL into commercial applications. Furthermore, each process is time-consuming, making them impractical for large-scale fabrication requirements. A new method is needed to integrate IL with the established optical lithography techniques.

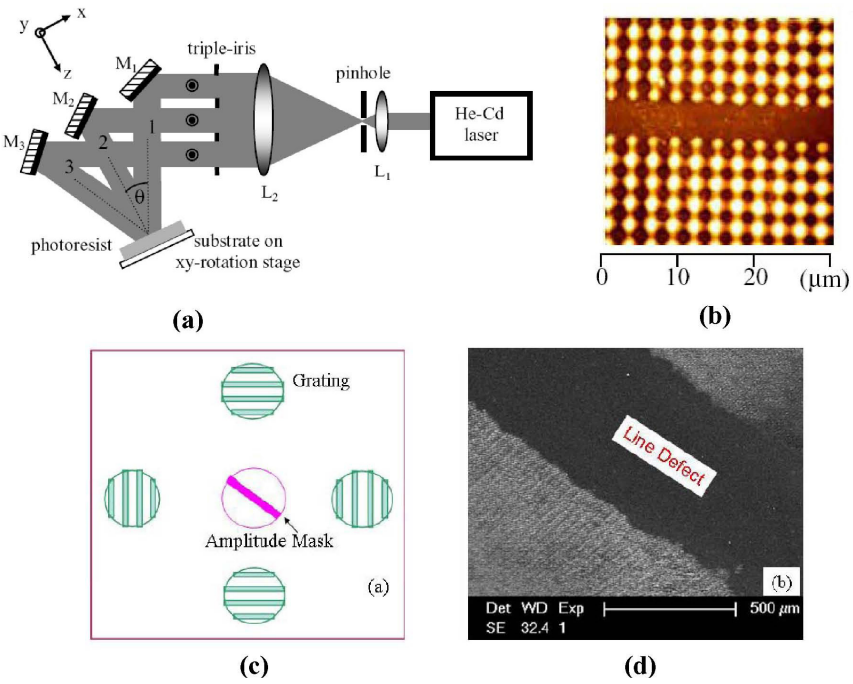

Figure 1.10: Combined fabrication techniques employing proximity and contact lithography to define non-periodic features. (a) Beams 1 and 3, reflecting off of Mirrors 1 and 3 (M1 and M3), intersect and interfere to form an interference fringe in the photoresist. Multiple exposures allow 2D periodic patterns. (b) A final exposure of a proximity or contact mask using Beam 2 produces a square-lattice interference pattern with a low-spatial-frequency line element [64]. (c) A five-beam diffractive-grating mask is modified to include a proximity amplitude mask with the central beam. (d) This allows for single exposure formation of a four-beam interference pattern with a low-spatial-frequency line element, defined by the mask [67].

Recently, IL was combined with mask-based proximity and contact lithography techniques, allowing for IL patterning incorporating low-spatial-frequency mask patterns in a positive photoresist [64]. In this method, once the periodic pattern was recorded in the photoresist through multiple two-beam exposures, a final exposure was made with a third beam, illuminating a mask on or in close proximity to the sample, as depicted in Fig. 1.10(a). The resulting square-lattice periodic pattern with incorporated mask elements is depicted in Fig. 1.10(b). More recently, a five-beam diffractive-grating mask was modified to include an amplitude mask with the central beam as depicted in Fig. 1.10(c) [67]. Using this method, a single exposure was used, for the first time, to produce a four-beam interference pattern with a single low-spatial-frequency mask element as depicted in Fig. 1.10(d).

A comparison of the combined techniques used to fabricate non-periodic functional elements in an MBI-defined periodic lattice is provided in Table 1.2. While the first five techniques listed in Table 1.2 offer the ability to fabricate high-spatial-frequency integrated functional elements, they are all prohibitively expensive and are based on time-consuming sequential fabrication methods to define the functional elements, precluding their use in commercial production. When PL is used to define the functional elements, as demonstrated in interference-assisted lithography, large-area patterning becomes possible, thereby reducing the fabrication time [5]. However, the requirement for multiple exposures makes this technique too expensive for large-volume production [2]. With the recent demonstration of MBI combined with proximity or contact lithography in a single-exposure step [67], commercially cost-effective fabrication seems possible. Unfortunately, while contact lithography offers high resolution, mask damage

results in low yield, making this method too costly for commercial production applications [222]. While proximity lithography reduces the risk of mask damage, this method is not capable of fabricating the full range of high-spatial-frequency integrated functional elements, with a typical resolution, or smallest feature size that can be recorded in a photoresist, limited to 2-4μm [222].

Table 1.2: Comparison of combined techniques to fabricate non-periodic functional elements in an MBI-defined periodic lattice.

Functional Element Fabrication Technique	Technique Characteristics			
	Fast?	Single Exposure?	Cost Effective?	High-Spatial-Frequency Integrated Functional Elements?
Electron Beam Lithography	No	No	No	Yes
Focused Ion Beam	No	No	No	Yes
Direct Laser Writing	No	No	No	Yes
Atomic Force Microscope Nano-Indentation	No	No	No	Yes
Multi-Photon Polymerization	No	No	No	Yes
Projection Lithography	Yes	No	No	Yes
Contact Lithography	Yes	Yes	No	Yes
Proximity Lithography	Yes	Yes	Yes	No

1.2 Research Objectives and Contributions

From Table 1.2 it is evident that a new lithographic method is needed to integrate a non-periodic functional element pattern within an MBI-defined periodic lattice in a single-exposure step, thereby reducing the complexity, fabrication time, and associated costs, making this combination a potential option for large-volume commercial fabrication. To address this need, the primary objective of the research presented in this thesis is to demonstrate a new lithographic method, Pattern-Integrated Interference Lithography

(PIIL). PIIL is the integration of superposed pattern imaging with IL. The result is a complex optical-intensity distribution composed of an MBI-defined periodic lattice modified by an integrated mask pattern image to form functional elements. In the work presented in this thesis, a Pattern-Integrated Interference Exposure System (PIIES) implements the PIIL methodology by incorporating a projection imaging capability in a novel three-beam interference configuration, enabling the single-exposure fabrication of a two-dimensional periodic PC lattice with non-periodic functional elements integrated into the periodic pattern [72,73]. After a description of the basic system design and functionality, a model is presented to simulate the optical-intensity distribution at the PIIES sample plane. The model is then used to evaluate the characteristics of the resulting PC structure with new intensity and lattice-vector metrics that differ markedly from those used in traditional photolithographic imaging systems. As a demonstration of PIIL, a prototype PIIES configuration is used to fabricate representative PC structures in a single-exposure step. Both simulations and experimental results confirm the potential of PIIL as method for fabricating dense integrated optical circuits.

In the design of the PIIES, a complete understanding of MBI patterning possibilities and configuration considerations is required. Accordingly, the secondary objective of this research is to provide a fundamental understanding of motif geometry possibilities along with the effects of parametric constraints on individual beam amplitudes and polarizations. From the comparison provided in Table 1.1, it is evident that this information is relevant to the PIIES design as well as future MBI systems.

The PIIL methodology, PIIES development, MBI applications review, motif geometry modeling, and constrained parametric analysis presented in this thesis resulted in the following accomplishments and contributions:

1. The development of PIIL to integrate superposed pattern imaging with IL as a method of single-exposure formation of an optical-intensity distribution consisting of high-spatial-frequency periodic patterns with integrated non-periodic functional elements [69,72-76].

2. The development of a PIIES that implements PIIL by incorporating a projection imaging capability in a novel three-beam interference configuration in order to fabricate, in a single-exposure step, a two-dimensional periodic PC lattice with non-periodic functional elements integrated into the periodic pattern [69,71-76].

3. The development of an analytical model that simulates the resulting optical-intensity distribution at the PIIES sample plane where the three beams simultaneously interfere and form a superposed image of the integrated mask pattern [75].

4. The development of appropriate PIIES performance metrics in order to quantify the characteristics of the resulting fabricated PC structure [75].

5. The development of PIIES alignment and experimental procedures [76].

6. The demonstration of the first single-exposure fabrication of representative PC structures using the PIIES configuration [72,75,76].

7. A comprehensive review of current MBI applications [38].

8. The development of an analytical model for the motif geometries associated with the plane-group symmetries possible for a square-lattice translational symmetry under the conditions for primitive-lattice-vector-direction equal contrast [77,78].

9. The development of an analytical model for the motif geometries associated with the plane-group symmetries possible for a hexagonal-lattice translational symmetry under the conditions for primitive-lattice-vector-direction equal contrast [77,78].

10. The development of a methodology to analyze parametric constraints in optimized three-beam interference [69,71,77,79].

11. The analysis of representative parametric constraints on the space-group symmetries and contrast for a square-lattice translational symmetry [77,79].

12. The analysis of representative parametric constraints on the space-group symmetries and contrast for a hexagonal-lattice translational symmetry [77,79].

The research in this field includes efforts to move PIIL towards commercial fabrication applications though (1) the development of comprehensive models to simulate and predict PIIL ability to fabricate densely packed functional elements over a large area, (2) systematic design and optimization of PIIES optical configurations, mask design, and fabrication methodologies, (3) development of a diffractive photo-mask to enable an interferometrically stable PIIL implementation for commercial applications [74], and (4) the application of PIIL in the areas of nano-electronics, PC devices, metamaterials, subwavelength structures, optical trapping, and biomedical structures.

1.3 Thesis Overview

The research objectives and accomplishments described previously are presented in detail in the following chapters.

First, a unified, comprehensive review of current MBI applications areas is presented in Chapter 2. Next, analytic models are presented in Chapter 3 to describe the specific motif geometries within the five 2D plane-group symmetries possible using three linearly

polarized interfering beams. These models are used to describe and design specific motif geometries for square and hexagonal-lattice points. With a complete understanding of three-beam interference patterning possibilities, Chapter 4 provides a methodology to analyze the effects of constraints on individual beam amplitudes and polarizations. Analysis includes the effects on interference-pattern symmetries and absolute contrast for both square and hexagonal lattices.

With this fundamental information, the PIIL methodology and PIIES design are presented in Chapter 5. In this chapter, a Fourier optics model is developed to simulate the aerial optical-intensity distribution produced at the PIIIES sample plane. This model includes both three-beam interference and the integrated mask pattern used to block selectively portions of the periodic pattern. With this model, new PC intensity and lattice-vector metrics are presented to quantify the quality of the resulting PIIIES-defined PC structures.

A demonstration of the PIIL methodology is presented in Chapter 6, including detailed PIIES configuration alignment techniques and experimental procedures. Finally, single-exposure PIIES experimental results are presented demonstrating the ability of the PIIL methodology to produce representative PC structures.

Chapter 7 summarizes the results of the research and provides directions for future work.

Appendix A provides a detailed description of the basic PIIIES optimization process using Zemax optical design software.

Appendix B provides a detailed description of the PIIES Zernike fringe coefficients obtained using Zemax optical design software.

CHAPTER 2

MUTI-BEAM INTERFERENCE APPLICATION AREAS

Over the past decade, research has developed a thorough understanding of the possibilities afforded by multi-beam interference (MBI). Accordingly, MBI has been utilized in an increasing variety of applications. While several review papers are available that describe MBI methods, capabilities, and impacts on nanostructure research [8,9,223,224], missing from the literature is a comprehensive review of current MBI applications. The present research complements these papers, providing a unified, comprehensive review of current applications utilizing MBI, including nano-electronics, photonic crystals, metamaterials, subwavelength structures, biomedical structures, and optical trapping. This review resulted in one invited journal publication [38].

2.1 Nano-Electronics

Driven by the microelectronics industry, interference lithography (IL) has received increasing attention in recent years as one of many potential methods of satisfying Moore's law prediction as documented previously in Chapter 1 of this thesis. In one example of a current application, IL was combined with optical contact lithography to fabricate triple-gate metal-oxide-semiconductor field effect transistors [6]. In another report, IL was used for metal thin-film patterning to fabricate the electrodes and metallization patterns required by modern microelectronic devices [7].

2.2 Photonic Crystals

Perhaps the most documented application of MBI and IL has been in the formation of photonic crystal (PC) structures and is the subject of more than half of the references included in this thesis. PC technology has many important possible commercial applications [225,226] with the possibility of lossless control of light propagation at a size scale near the order of the wavelength of light. This technology has the potential to produce the first truly dense integrated photonic circuits and systems (DIPCS). Individual components that are being developed include resonators, antennas, sensors, multiplexers, filters, couplers, and switches. The integration of these components would produce DIPCS to perform functions such as image acquisition, target recognition, image processing, optical interconnections, analog to digital conversion, and sensing. Further, the resulting DIPCS would be very compact in size and highly field portable. Applications using light at telecommunications wavelengths require structures to be fabricated with nano-sized dimensions. Despite the advantages and benefits of using such a technology in commercial devices, the practical commercial development of PC structures has been very slow.

To date, research has not fully developed a methodology for the large-scale and cost-effective integration of these impressive PC-based devices into manufacturable DIPCS. No rapid and inexpensive systematic fabrication procedure has been developed for the reliable and reproducible fabrication of nano-sized PC structures. IL has been proposed as one method to overcome this deficiency. In the late 1990s, IL was used to produce 2D [20] PC lattices exhibiting a photonic bandgap and later three dimensional (3D) face-centered cubic [19] PC structures as depicted in Fig. 2.1(a). Since then, IL has been

studied extensively, optimized, and used to fabricate PCs [11-18] with ongoing efforts to develop PC-based devices through a combination of lithography techniques such as the PC waveguide depicted by the scanning electron microscope (SEM) image in Fig. 2.1(b). In fact, the design rules for MBI-defined PC waveguide devices have been established when IL is combined with direct laser writing [227]. Recently, nanoscale PC-band-edge lasers were fabricated with the use of IL, paving the way for the integration of electrically driven PC lasers [228] as depicted in Fig. 2.1(c). Other proposed PC-based devices relying on IL include optical add-drop multiplexers [229], organic light-emitting diodes (LEDs) [230], coupled PC resonator arrays [231], and PC distributed feedback quantum cascade lasers [232].

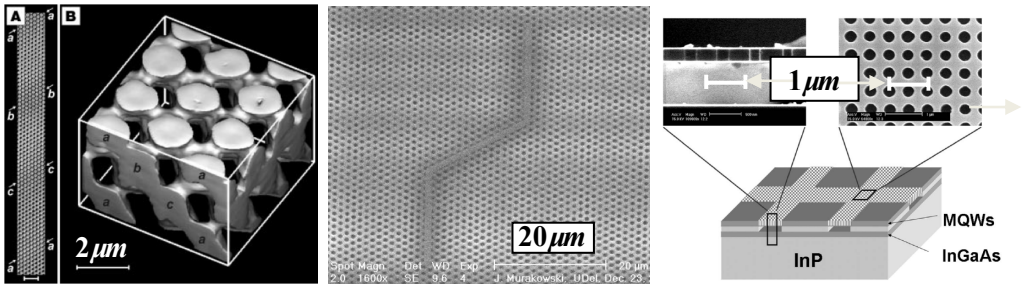

Figure 2.1: Photonic crystals. (a) 3D face-centered-cubic PC structure created by four-beam IL. Inset A shows an SEM image of the bottom surface of the PC, while B depicts the reconstructed 3D surface [19]. (b) PC waveguide created by electron-beam lithography in a 2D hexagonal lattice formed by IL [212]) (c) Schematic view of an air-bridge type PC band-edge laser with SEM images of the square lattice PC structure fabricated using IL [228].

2.3 Metamaterials

Like PCs, metamaterial technology offers the control of light propagation, only now at a size scale much smaller than the wavelength of light. Accordingly, metamaterial-based devices have many important possible commercial applications [233-236]. Ultra-

compact objective lenses, frequency-doubling devices, parametric amplifiers, electromagnetic cloaking, and parametric oscillators all become possible with metamaterials. The integration of these components would produce DIPCS that are very compact in size and highly field-portable.

In natural materials, atoms are arranged in a regular pattern with periods of approximately half of a nanometer. In these natural materials, the electric field component of the incident light excites the electric dipoles of the material. These dipoles re-radiate with some phase retardation. Thus, the electric relative permittivity, ε_r, is not equal to unity. In contrast, the magnetic dipoles do not interact appreciably with the magnetic field component of the incident light. Thus the relative magnetic permeability , μ_r, is unity. Metamaterials overcome this lack of magnetic dipole through subwavelength-sized artificial magnetic dipoles (e.g. split-ring resonator structures). The index of refraction, in general, is $n = \pm(\varepsilon_r \mu_r)^{1/2}$. For the case when both ε_r and μ_r are less than zero, the refractive index is negative. That is, $n = -(\varepsilon_r \mu_r)^{1/2}$. The index is *not* $n = +(\varepsilon_r \mu_r)^{1/2}$. This result was first reported and discussed by Veselago [237].

The subwavelength-sized magnetic dipoles needed to make a metamaterial, can be produced by making microscopic split-ring resonators (SRR's). These SRR devices have also been called "slotted-tube resonators" or "loop-gap resonators" in the literature. If SRR devices are produced in subwavelength arrays, they behave as "magnetic atoms" and thus metamaterials become possible. Metamaterials have been developed successfully at microwave frequencies [238-240]. However, the production of metamaterials at optical frequencies has been much more challenging [241,242]. Further, current technologies lack the ability to produce these precise nanostructure devices

rapidly and at low cost. Again, IL provides a potential solution to this critical shortcoming [32]. To produce a large area split-ring array template for magnetic metamaterials, IL has been proposed as a mechanism to form single-slit and double-slit split-ring arrays in 2D triangular and square lattice arrays [37]. Others have used IL to demonstrate high-throughput experimental fabrication of metal-dielectric-metal "magnetic atoms" [33,34] as depicted in Fig. 2.2(a), as well as cylindrical nanoshell, U-shaped, and double-split ring resonator array metamaterials [35] as depicted in Fig. 2.2(b). In some cases, IL may be used in conjunction with other methods to facilitate the economical fabrication of metamaterials. For example, IL can be used to form a 1D array of trenches to serve as a template for the self-directed assembly of a silver nanocluster metamaterial [36].

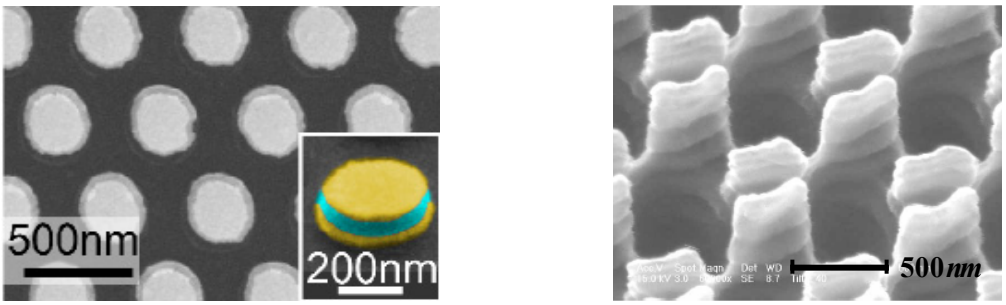

(a) **(b)**

Figure 2.2: Metamaterial examples. (a) SEM view of a "magnetic atom" defined by a three-beam-generating IL prism, with an oblique-incidence view of layered Au (golden), MgF_2 (blue), and Au [33]. (b) SEM view of double-split ring resonator array metamaterial fabricated via phase-modulated six-beam IL [35].

2.4 Subwavelength Structures

By utilizing the subwavelength periodic patterns produced by IL, numerous important structures can be realized for an increasing number of subwavelength structure applications, including guided-mode resonant elements [243], synthesized-index elements, form-birefringent polarization elements, field-emission devices, plasmonic

structures, surface texturing, magnetic nanostructures, and numerous other nanotechnology efforts.

2.4.1 Guided-Mode Resonant Elements

Guided-mode resonant gratings are utilized widely for their very narrowband filter characteristics [244-246]. Such subwavelength-grating filters represent important devices in dense-wavelength-division multiplexed communications and in chemical, biological, toxicological, and environmental sensing applications. Recently, broadband versions of these resonant gratings have also been demonstrated [247].

2.4.2 Synthesized-Index Elements

Synthesized-index elements include one-dimensional (1D) and 2D periodic surface structures for use as antireflection surfaces. Simple 1D binary surface-relief gratings on dielectrics can exhibit zero-reflectivity at optical wavelengths [248,249]. For example, IL has been used to record subwavelength gratings on the surface of diffractive beam splitters, reducing surface reflections, thereby improving efficiency [250]. Similarly, IL was used to fabricate subwavelength antireflective coatings to improve the performance of optoelectronic LEDs [251]. More recently, subwavelength antireflection patterns were recorded in a Si substrate using IL, providing broadband (250-1200nm), wide angle (0 – 45°) operation [252] as depicted in Fig. 2.3(a). Such antireflection surfaces have been extended to lossy, even metallic, materials [253,254]. Two-dimensional crossed gratings have also been implemented to provide polarization-independent antireflection behavior, mimicking the effect of a "moth's eye" [183,255-258]. Periodic and quasi-period surfaces have been applied widely to increase the efficiency of solar cells [259,260]. To this end, IL was used recently to fabricate antireflective gratings on thin-film solar cells

[261]. Other example applications include a 100*nm* period grating in an amorphous silicon thin film used to stabilize the linear polarization of vertical-cavity surface-emitting laser operating at 850*nm* [262], and a critical angle transmission grating facilitated by the use of scanning-beam IL [263].

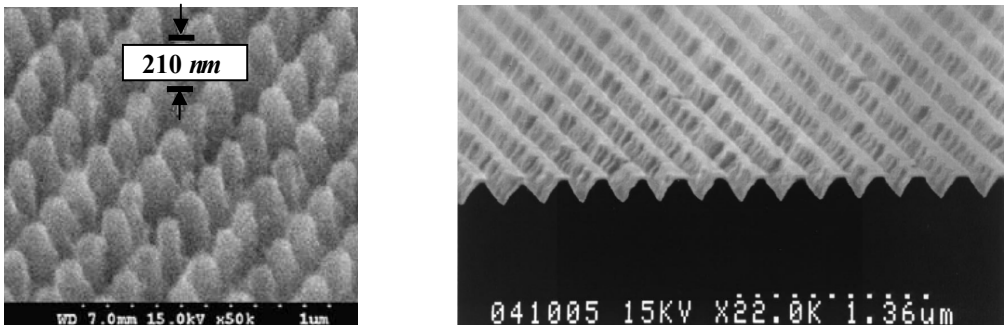

(a) **(b)**

Figure 2.3: Subwavelength optical structures. (a) SEM view of synthesized-index anti-reflective Si post array defined by multi-exposure IL [252]. (b) SEM image of a form-birefringent polarization grating retarder fabricated via two-beam interference [61].

2.4.3 Form-Birefringent Polarization Elements

Form-birefringent polarization elements include retardation plates, polarizers, and beam-splitters. Retarders can behave as quarter-waveplates, half-waveplates, full-waveplates, etc. and thus convert linearly polarized light to circular polarization, rotate linear polarization, provide narrowband filtering, etc. Subwavelength grating retarders have been made using IL for use in the visible and in infrared regions of the spectrum [264] as depicted in Fig. 2.3(b). Similarly, subwavelength-grating polarizers have also been reported [61]. Two-beam IL has been demonstrated as a cost-effective fabrication process to generate these subwavelength structures [249].

2.4.4 Field-Emission Devices

The process of field emission ejects electrons from a metal surface or a doped semiconductor material under the influence of an applied electric field. Traditionally, field emission is generated from micro-structured tips used as the cathodes for electron extraction. Field emission devices have found applications in field-emission displays, vacuum microelectronics, satellite subsystems, mass spectrometers, and even electrodynamic space tethers [265,266]. As early as 1995, IL was used to manufacture high density micro-field emitter arrays with submicron emitter spacing to improve field emission display performance and reduce manufacturing costs [189,267]. Recent efforts have focused on the use of IL, combined with catalytic etching, to produce the nanocones used in field emission as depicted in Fig. 2.4(a), eliminating the need for other more complicated lithography techniques [268]. Others have employed IL to produce carbon nanotubes as depicted in Fig. 2.4(b) that could prove useful in field emission display applications [269].

(a) **(b)**

Figure 2.4: Field emission structures. (a) SEM view of silicon-etched nanowires defined by two-beam, multiple-exposure IL [268]. (b) Tilted SEM view of vertically-aligned carbon nanofibers, where a multi-exposure Lloyd's mirror configuration provides the Ni catalyst patterning for nanofiber growth [269].

2.4.5 Plasmonic Structures

Surface plasmon resonances occur for a range of frequencies when an electromagnetic field excites oscillations of free electrons on the surface of metallic nanostructures [270]. Near-field coupling effects on the plasmon resonance of these metal nanostructures, called localized surface plasmons, can be used in biosensing applications, surface enhanced Raman spectroscopy, and novel photonic devices [128,271,272]. The mechanism of plasmonic resonance is directly related to the refractive index variation in the metallic film nanostructures, often fabricated using self-assembly methods. As an alternative to self-assembly methods, IL has been used as a mechanism to produce plasmonic metallic nanostructures including silver dot arrays [270,273], gold particle arrays [128,271], and bimetallic dot structures [104,272] depicted in Figs. 2.5(a)-(c).

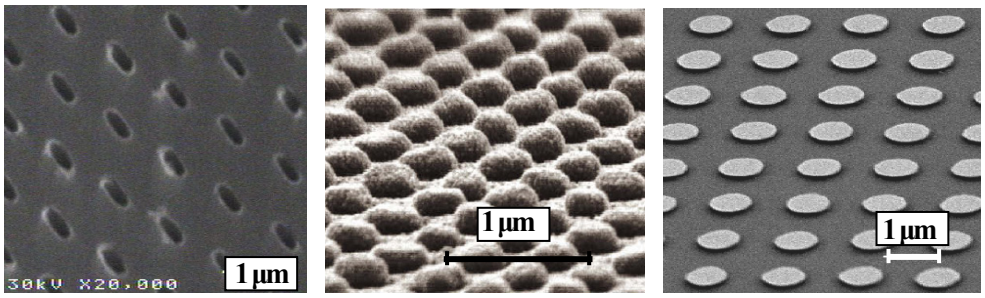

Figure 2.5: Plasmonic structures. (a) SEM image of MBI-defined hexagonal lattice of elliptical holes in a 100*nm* thick silver film [273]. (b) 3D view of gold nano-particle array with a lattice constant of 400*nm*, defined by two-beam, multi-exposure MBI [128]. (c) SEM image at a 50*deg* tilt of bimetallic (Ag/Au) dots on a quartz substrate fabricated using a Lloyd's mirror configuration [272].

2.4.6 Surface Texturing

Surface patterning has been the subject of much study, with applications across numerous areas, including microelectromechanical systems, automotive, aviation, defense, and biological areas [209,274]. Laser surface texturing using MBI is of particular interest to

tribology technologies including textured surfaces for mechanical seals, piston rings, and thrust bearings. In one study, laser interference metallurgy was employed to improve lubrication film lifetimes and the tribological behavior of various surface textured materials as depicted in Fig. 2.6(a) [209]. Others have studied the wetting properties and superhydrophobicity of surfaces, patterned by laser interference, for such applications as corrosion inhibition, microfluidic technology, self-cleaning window glass, and evaporation-driven nanopatterning [185,275]. Similarly, interference patterning has been used to create biomemetic structures as depicted in Fig. 2.6(b), mimicking natural sub-micron patterns [276] such as bone material and shells exhibiting advantageous mechanical stability and dynamic surface properties [274].

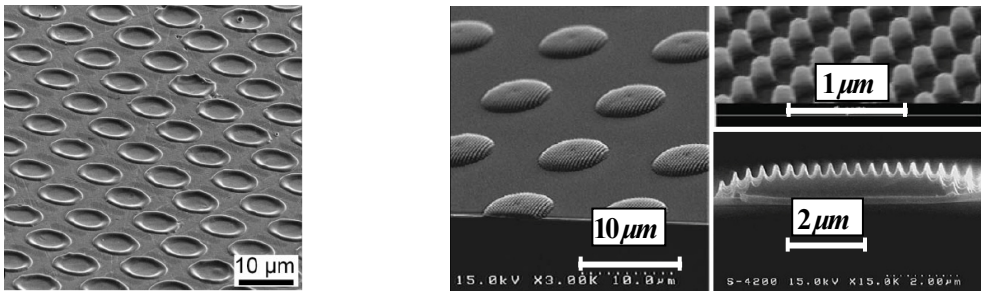

Figure 2.6: Surface texturing. (a) SEM view of laser interference metallurgy defined dot-like structures, recorded directly on a metallic surface with low laser fluence to change the tribological behavior of the surface [209]. (b) MBI-defined nanopillar arrays are patterned in a hierarchical structure, mimicking the surface of a lotus leaf, for enhanced hydropholic phenomenon [276].

2.4.7 Magnetic Nanostructures

Magnetic nanostructures, often called "nanomagnets," have been proposed as an alternative technology for information storage [277,278]. In this application, discrete nanomagnets with uniaxial magnetic anisotropy store binary information when magnetized in one of two possible antiparallel directions. To generate these magnetic

nanostructures, IL has been used to generate a nanoscale array of dots that are, in turn, transferred to a magnetic film using ion beam etching as depicted in Fig. 2.7(a) [277,278]. Others have employed IL in the fabrication of cobalt magnetic arrays for use in magnetic random access memory devices as depicted in Fig. 2.7(b) [279]. Most recently, IL was used to create magnetic patterns in Co/Pd multilayer systems with favorable magnetic properties as depicted in Fig. 2.7(c) [280].

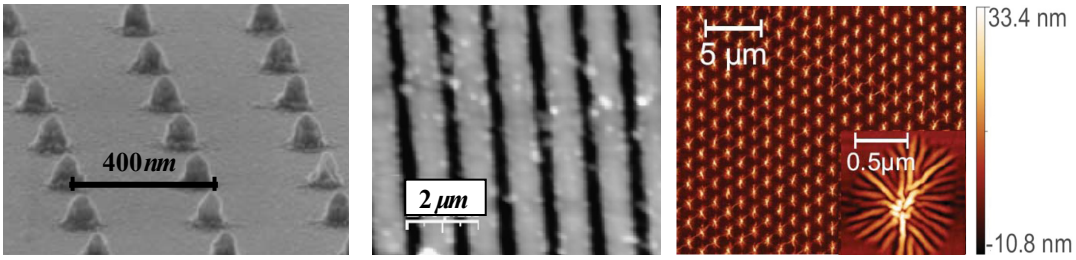

(a) **(b)** **(c)**

Figure 2.7: Magnetic nanostructures. (a) SEM profile image of a nanomagnet array with a periodicity of 400*nm*, defined by multiple MBI exposures [278]. (b) 1D cobalt array fabricated using two-beam MBI [279]. (c) Atomic force microscopy image of a Co/Pd multilayer system structured with three-beam IL [280].

2.5 Biomedical Structures

Periodic or quasi-periodic structures are critically important in a wide variety of biomedical areas. Some representative example applications are described here to help gauge the potential impact that MBI may have in biomedicine. In regenerating nerves, arrays of microchannels are needed to guide nerve growth [281]. In facilitating bone regrowth, periodic meshes are needed to retain and sequester bone morphogenetic protein [282]. In forming, maintaining, and repairing of tissue, engineered surfaces are needed that present controlled densities of peptides to direct the assembly of extracellular matrices [283]. In measuring the strength of cell adhesion to the extracellular matrix,

meshes are needed to control the size and position of cells to be able to determine the individual contributions of the various structures present [284]. In identifying genetic biomarkers for human disease, high density microarrays are needed for the detection of dozens of polymorphisms in a single analysis [285]. In the study of cell functions (gene expression, adhesion, migration, proliferation, and differentiation), micropatterning of the cells is needed since the cell functions are affected by the microscale and nanoscale environment [286]. In enhancing bone formation *in vivo*, it is necessary to microstructure the titanium implant surfaces. For example, $100\mu m$ cavities are found to produce osteoblast attachment and growth [287].

Common to all of these biomedical applications is the requirement for appropriate periodic or quasi-periodic structures that can be made by IL. This fact has led several to turn to IL for numerous biomedical applications in recent years. For example, micro-structured particles have been produced using a combination of IL and stop-flow lithography (a microfluidic process that enables optical lithography to be performed in a flowing stream of oligomer) as depicted in Fig. 2.8(a) with several potential applications including cell growth, tissue engineering, and biosensors [21]. To immobilize proteins in a square array of anchor sites, nano-scale lattices were formed by IL. This application assists in the analysis of biomaterials and the study of interactions of living cells with biomolecules [22,24]. As an example, Fig. 2.8(b) depicts a scanning electron microscope image of square lattice of submicron domains to provide selective absorption of protein fibronectin, leading to advanced studies in the influence of protein organization in adhesion complex formation and function. In the development of neural prosthetic devices, phase mask IL was used to fabricate 3D hydrogels with controlled geometries

and sub-micron feature sizes as depicted in Fig. 2.8(c). This application could lead to advances in drug delivery, tissue engineering and improved material-device interactions [25]. In the field of antibacterial research, IL was used to create a 2D pore-array to immobilize silver nanoparticles, known for their antibacterial properties. In a study of this application, the fabricated antibacterial nanocomposition proved effective against the *E. coli* bacteria [23]. Based on these recent examples, IL could become an important tool in the development of the next generation of biomedical structures.

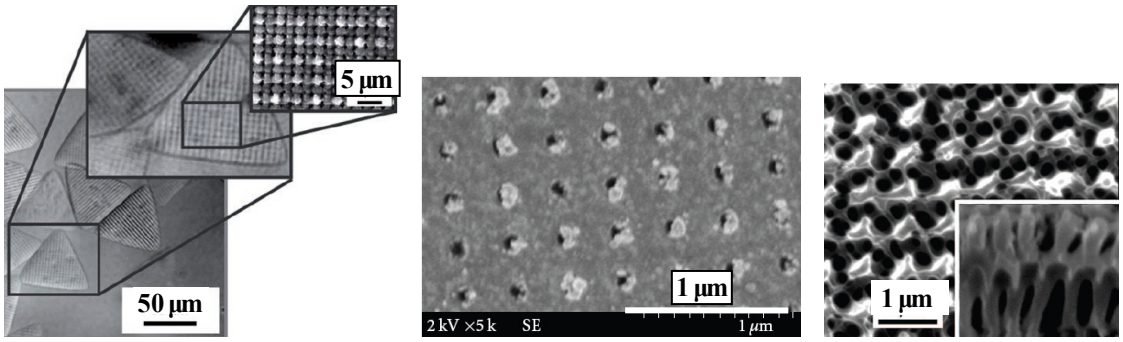

(a) **(b)** **(c)**

Figure 2.8: Biomedical applications. (a) SEM image of micro-structured particles formed using a combination of phase-mask IL and stop-flow lithography [21]. (b) SEM image of square lattice of submicron domains indicate selective absorption of protein fibronectin that is confined to the MBI-defined 100*nm* domains indicated by a gold-enhanced solution [22]. (c) SEM image of 3D hydrogel structure with interconnected nanopores fabricated using an IL phase mask and cross-sectional interconnects [25].

2.6 Optical Trapping

The periodic pattern produced by MBI need not always be recorded in a photosensitive material. For example, an MBI optical-intensity distribution may be used directly in optical trapping. Traditionally, optical trapping relies on the increased electrical field associated with the localized optical intensity of a focused beam. A dielectric particle is, in turn, guided by the increased electric field force to the point of the highest light intensity. By this mechanism, optical traps have been used to manipulate a range of

particles including polymer spheres, metallic particles, and biological specimens [288]. Recently, holographic optical tweezers have been used to trap and manipulate multiple suspended micro- and nano-scale particles simultaneously, where focused beams are replaced by computer-defined beam arrays generated by a spatial light modulator [289]. Sophisticated algorithms have been developed to provide updates to the computer generated array to control dynamically particle orientation. Recently, this techniques was used to control and study rod-shaped bacteria [290] and zeolite L crystals [291].

As an alternative to computer generated holographic optical tweezers, MBI may provide similar optical arrays along with dynamic control of light intensity and orientations in two- and three dimensions, easing the requirement for complicated computer control algorithms. MBI optical trapping was first realized in the 1990's with a two-beam interferometric trap to hold polystyrene beads of a few microns in diameter as depicted in Fig. 2.9(a) [28]. Later, 2D and 3D interference patterns were used to trap, sort, and manipulate trapped particles on a small scale using focused interfering beams [27,29-31,292] as depicted in Fig. 2.9(b). Recently, large-area 3D arrays of optical traps have been demonstrated through the use of MBI, without the need for iterative computational algorithms, as depicted in Fig. 2.9(c) [26].

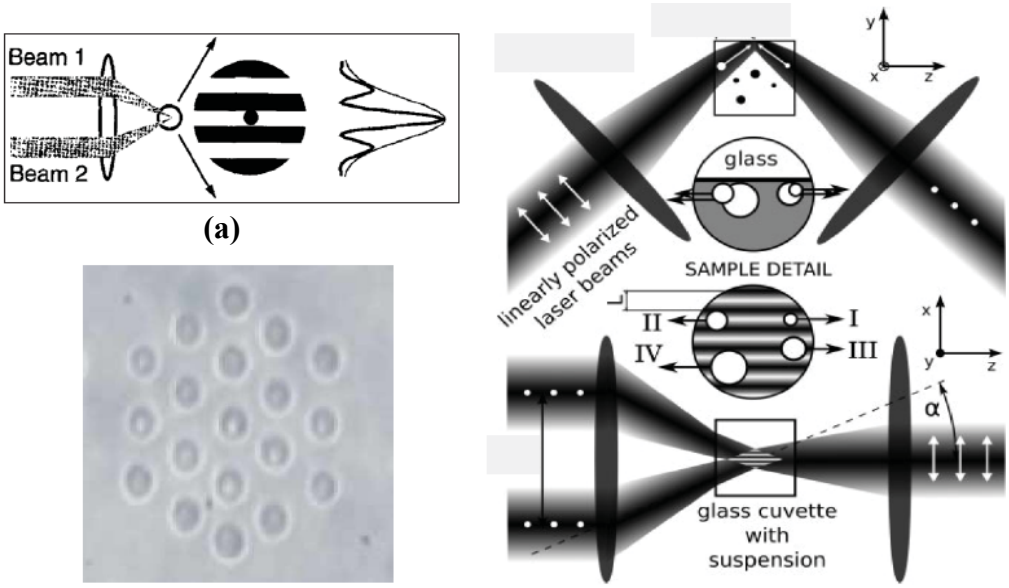

Figure 2.9: Optical trapping. (a) Two-beam interferometric optical trap [28]. (b) Experimental configuration for optical sorting in three-beam interference. The interference pattern is formed at the top of the glass curvette. Roman numerals indicate four different types of object sorting [293]. (c) Image of a 19-sphere array of $2\mu m$ diameter silica spheres trapped in a hexagonal interference pattern formed by three-beam interference [26].

CHAPTER 3

TWO-DIMENSIONAL MOTIF GEOMETRIES

For each of the application areas presented Chapter 2, the individual motif geometries of the periodic interference patterns often play a significant role in the performance characteristics of a device fabricated using multi-beam interference (MBI) [25,48-50,52,53,93-110]. Accordingly, several studies report methods to select individual beam parameters to change the motif orientation and shape for a specific MBI-defined pattern [48,53,294,295]. To facilitate these efforts and ensure maximum patterning capability in the Pattern-Integrated Interference Exposure System (PIIES), a general model is presented here for the optimized 2D motif geometries resulting from linearly polarized three-beam interference for both square- and hexagonal-lattice translational symmetries, under the conditions for primitive-lattice-vector-direction equal contrast [58]. This research has resulted in one journal paper [78] and one conference paper [77].

3.1 Motif Geometry Modeling

An understanding of the exact geometrical shape of the 2D interference-pattern motifs begins by first solving the time-independent optical-intensity distribution given by Eq. (1.2) for three linearly-polarized beams. The resulting distribution is

$$I_T(\mathrm{r}) = I_o\left\{1 + V_{12}\cos\left[\left(\mathrm{k}_2 - \mathrm{k}_1\right)\cdot\mathrm{r}\right] + V_{13}\cos\left[\left(\mathrm{k}_3 - \mathrm{k}_1\right)\cdot\mathrm{r}\right] + V_{23}\cos\left[\left(\mathrm{k}_3 - \mathrm{k}_2\right)\cdot\mathrm{r}\right]\right\}. \quad (3.1)$$

This equation may be used to plot and simulate the optical-intensity distribution of the resulting periodic pattern as depicted in Fig. 3.1.

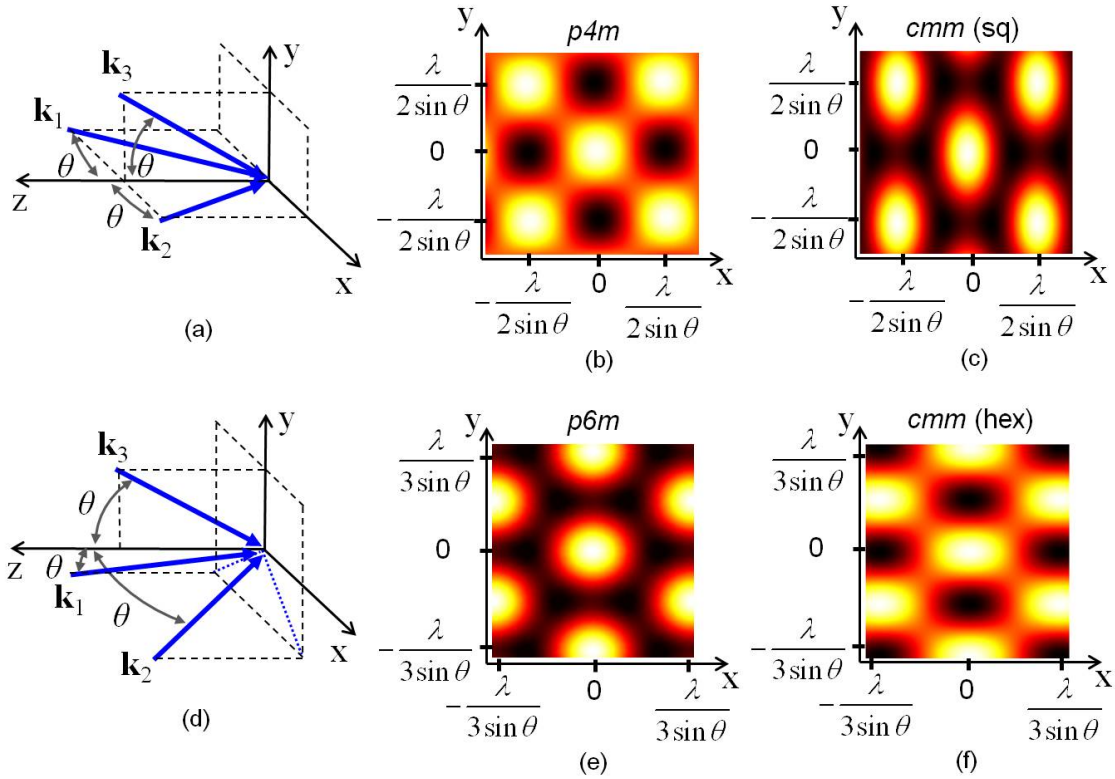

Figure 3.1: Example three-beam interference wavevector configurations. (a) A square-lattice interference pattern with (b) *p4m* or (c) *cmm* plane-group symmetry is produced by three beams, where $\mathbf{k}_3$ is contained in the *y*-*z* plane while $\mathbf{k}_1$ and $\mathbf{k}_2$ are contained in the *x*-*z* plane, each at a common incidence angle, θ. (d) A hexagonal-lattice interference pattern with (e) *p6m* or (f) *cmm* plane-group symmetry is produced by three beams, where $\mathbf{k}_3$ is contained in the *y*-*z* plan and $\mathbf{k}_1$ and $\mathbf{k}_2$ are arranged such that the projections of all three vectors are separated by exactly 120*deg* in the *x*-*y* plane.

The two common three-beam wavevector configurations depicted in Figs. 3.1(a) and (d) are used to form lattices with square and hexagonal translational symmetry, respectively. For a lattice with square translation symmetry as depicted in Figs. 3.1(b) and (c), the three beams, represented by wavevectors $\mathbf{k}_1$, $\mathbf{k}_2$, and $\mathbf{k}_3$, intersect at the x-y plane at a common incidence angle, θ, with respect to the z axis, where $\mathbf{k}_3$ is contained in the *y*-*z* plane while $\mathbf{k}_1$ and $\mathbf{k}_2$ are contained in the *x*-*z* plane. In this configuration,

$$\mathbf{k}_{1,sq} = -\sin\theta\hat{\mathrm{x}} + \cos\theta\hat{\mathrm{z}}, \tag{3.2}$$

$$\mathbf{k}_{2,sq} = \sin\theta\hat{\mathrm{x}} + \cos\theta\hat{\mathrm{z}}, \tag{3.3}$$

and

$$\mathbf{k}_{3,sq} = \sin\theta\hat{\mathrm{y}} + \cos\theta\hat{\mathrm{z}}. \tag{3.4}$$

The periodicity or lattice constant, a_{sq}, of the interference pattern is then given by

$$a_{sq} = \frac{\lambda}{\sqrt{2}\sin\theta}. \tag{3.5}$$

For a lattice with hexagonal translation symmetry as depicted in Figs. 3.1(e) and (f) the wavevectors are again arranged at a common incidence angle with $\mathbf{k}_1$ contained in the *y-z* plan, and now $\mathbf{k}_2$ and $\mathbf{k}_3$ are arranged such that the projections of all three vectors are separated by exactly $120\,deg$ in the *x-y* plane. In this configuration

$$\mathbf{k}_{1,hex} = -\sqrt{3}/2\sin\theta\hat{\mathrm{x}} - 1/2\sin\theta\hat{\mathrm{y}} + \cos\theta\hat{\mathrm{z}}, \tag{3.6}$$

$$\mathbf{k}_{2,hex} = \sqrt{3}/2\sin\theta\hat{\mathrm{x}} - 1/2\sin\theta\hat{\mathrm{y}} + \cos\theta\hat{\mathrm{z}}, \tag{3.7}$$

and

$$\mathbf{k}_{3,hex} = \sin\theta\hat{\mathrm{y}} + \cos\theta\hat{\mathrm{z}}. \tag{3.8}$$

The periodicity or lattice constant, a_{hex}, of the resulting interference pattern is given by

$$a_{hex} = \frac{2\lambda}{3\sin\theta}. \tag{3.9}$$

3.1.1 Circle to Square: *p4m* Plane-Group Symmetry

When the beam amplitudes and polarizations are selected to satisfy the conditions for maximum absolute contrast and primitive-lattice-vector-direction equal contrasts for the *p4m* plane-group symmetry ($|\mathbf{a}| = |\mathbf{b}|$, $\mathbf{a}\cdot\mathbf{b} = 0$, $V_{13} = V_{23}$, and $V_{12} = 0$) the resulting continuous optical-intensity distribution produces circular lattice motifs at the intensity maxima and minima as depicted in Fig. 3.2(a). Figure 3.2(b) depicts the same intensity profile plotted as isocontours representing specific fractions of the maximum intensity

$I_T(\mathrm{r})/I_{T,\max}$. Here, it can be seen that the actual motif shape changes from that of a circle near the center of a motif to that of a square as the contour intervals progress radially outward from the intensity maxima.

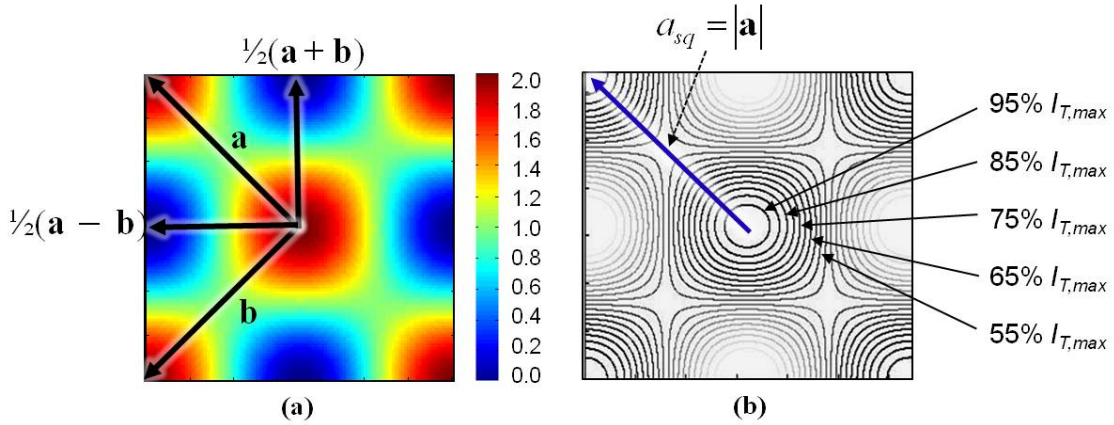

Figure 3.2: Simulated square-lattice interference pattern with *p4m* plane-group symmetry. (a) The continuous intensity profiles depict circular lattice motifs at the intensity maxima and minima. (b) Intensity isocontours at 5% intervals of the maximum intensity $I_{T,max}$ result in lattice motifs that change between circular and square geometries.

Recently, an analytical expression was reported that described the shape of a diffraction pattern that changes between a circle and square using a modified form of a superellipse equation [296]. This transformation is described by

$$s^2 \frac{x^2 y^2}{r^4} - \left(\frac{x^2}{r^2} + \frac{y^2}{r^2} \right) + 1 = 0, \tag{3.10}$$

where r is the radius of a circle and s is a parameter that describes the degree to which the shape resembles a circle (s = 0) or a square (s = 1). The derivation for this equation begins with an equation for a square given by

$$\left(1 - \frac{x^2}{r^2}\right)^{1/2} \left(1 - \frac{y^2}{r^2}\right)^{1/2} = 0. \tag{3.11}$$

If Eq. (3.11) is restricted to real values, solutions to this equation are $x = \pm r$ for $y^2 \le r^2$ and $y = \pm r$ for $x^2 \le r^2$, thereby forming a square. Equation (3.11) may be factored to

$$\frac{x^2 y^2}{r^4} - \left(\frac{x^2}{r^2} + \frac{y^2}{r^2} \right) + 1 = 0. \tag{3.12}$$

An s^2 term may now be added to the first term of Eq. (3.12), resulting in the form given in Eq. (3.10).

To determine the radial and *s*-parameter values in Eq. (3.10), the square-lattice intensity profile may be solved along the **a**, **b**, ½(**a** + **b**), and ½(**a** − **b**) lattice-vector directions by substituting the wavevector definitions given by Eqs. (3.2)-(3.4) into the three-beam intensity distribution given by Eq. (3.1) and solving along the radial directions, $\hat{x} + \hat{y}$, $\hat{x} - \hat{y}$, $\hat{x}$, and $\hat{y}$ respectively. The resulting square-lattice vector intensity profiles are given by

$$I_{T,sq,\mathrm{a}}(r) = I_o \left[1 + V_{12} \cos\left(\frac{2\pi}{\lambda} r \sin\theta \right) + V_{13} \cos\left(\frac{2\pi}{\lambda} r \sin\theta \right) + V_{23} \right], \tag{3.13}$$

$$I_{T,sq,\mathrm{b}}(r) = I_o \left[1 + V_{12} + V_{13} \cos\left(\frac{2\pi}{\lambda} r \sin\theta \right) + V_{23} \cos\left(-\frac{2\pi}{\lambda} r \sin\theta \right) \right], \tag{3.14}$$

$$I_{T,sq,1/2(\mathrm{a}+\mathrm{b})}(r) = I_o \left[1 + V_{12} \cos\left(\frac{\sqrt{2}\pi}{\lambda} r \sin\theta \right) + V_{13} \cos\left(\frac{\sqrt{2}\pi}{\lambda} r \sin\theta \right) + V_{23} \cos\left(-\frac{\sqrt{2}\pi}{\lambda} r \sin\theta \right) \right], \tag{3.15}$$

and

$$I_{T,sq,1/2(\mathrm{a}-\mathrm{b})}(r) = I_o \left[1 + V_{12} \cos\left(\frac{\sqrt{2}\pi}{\lambda} r \sin\theta \right) + V_{13} + V_{23} \cos\left(\frac{\sqrt{2}\pi}{\lambda} r \sin\theta \right) \right]. \tag{3.16}$$

Equation (3.10) may now be used to describe the transformation of an interference-pattern motif with *p4m* plane-group symmetry, where the radius of the circle, *r*, (or half side of the square when *s* = 1) is equivalent to the radial distance $r_{½(\mathbf{a}+\mathbf{b})}$ or $r_{½(\mathbf{a}-\mathbf{b})}$ from the

center of the motif to the specific isocontour along the ½(**a** + **b**) lattice vector directions depicted in Fig. 3.2(a). Equation (3.10) becomes

$$s^2 \frac{x^2 y^2}{r_{1/2(\mathrm{a}+\mathrm{b})}^4} - \left(\frac{x^2}{r_{1/2(\mathrm{a}+\mathrm{b})}^2} + \frac{y^2}{r_{1/2(\mathrm{a}+\mathrm{b})}^2} \right) + 1 = 0. \tag{3.17}$$

The *s* parameter may be determined by evaluating the *p4m* optical-intensity distribution along the $\hat{x} + \hat{y}$ and $\hat{y}$ directions, corresponding to the **a** and ½(**a** + **b**) lattice vectors. Here, the radial distance along the **a** and ½(**a** + **b**) lattice-vector directions, for a specific intensity fraction of the maximum intensity, $I_{T,max}$, may be found by solving Eqs. (3.13) and (3.15) to obtain

$$r_{\mathrm{a}} = \cos^{-1}\left[\left(\frac{I_{T,\max}}{I_o} T_{contour} - 1 \right) / V \right] \frac{\lambda}{2\pi \sin\theta}, \text{ and} \tag{3.18}$$

$$r_{1/2(\mathrm{a}+\mathrm{b})} = \cos^{-1}\left[\left(\frac{I_{T,\max}}{I_o} T_{contour} - 1 \right) / 2V \right] \frac{\lambda}{\sqrt{2}\pi \sin\theta}, \tag{3.19}$$

where the common interference coefficient, *V*, is given by Eq. (1.14) and $T_{contour}$ is the fraction of the maximum intensity at a specific isocontour. Finally, Eq. (3.17) may be solved to determine the *s* parameter value as given by

$$s = 2r_{1/2(\mathrm{a}+\mathrm{b})}^2 / r_{\mathrm{a}}^2 \sqrt{r_{\mathrm{a}}^2 / r_{1/2(\mathrm{a}+\mathrm{b})}^2 - 1}. \tag{3.20}$$

Equations (3.19) and (3.20) may now be used to define the parameters in Eq. (3.17) at specific intensity isocontours as depicted in Fig. 3.3. The resulting analytical model given by Eq. (3.17) is plotted in Figs. 3.3(b)-(d) along with the Matlab [297] simulated interference-pattern intensity distribution at isocontours of 95%, 75%, and 55% of $I_{T,max}$ respectively. Here, is it clear that Eq. (3.17) provides an excellent representation of the

motif geometry as it changes from a circle to a square radially from the center of the lattice point, as reflected in the increasing s parameter values.

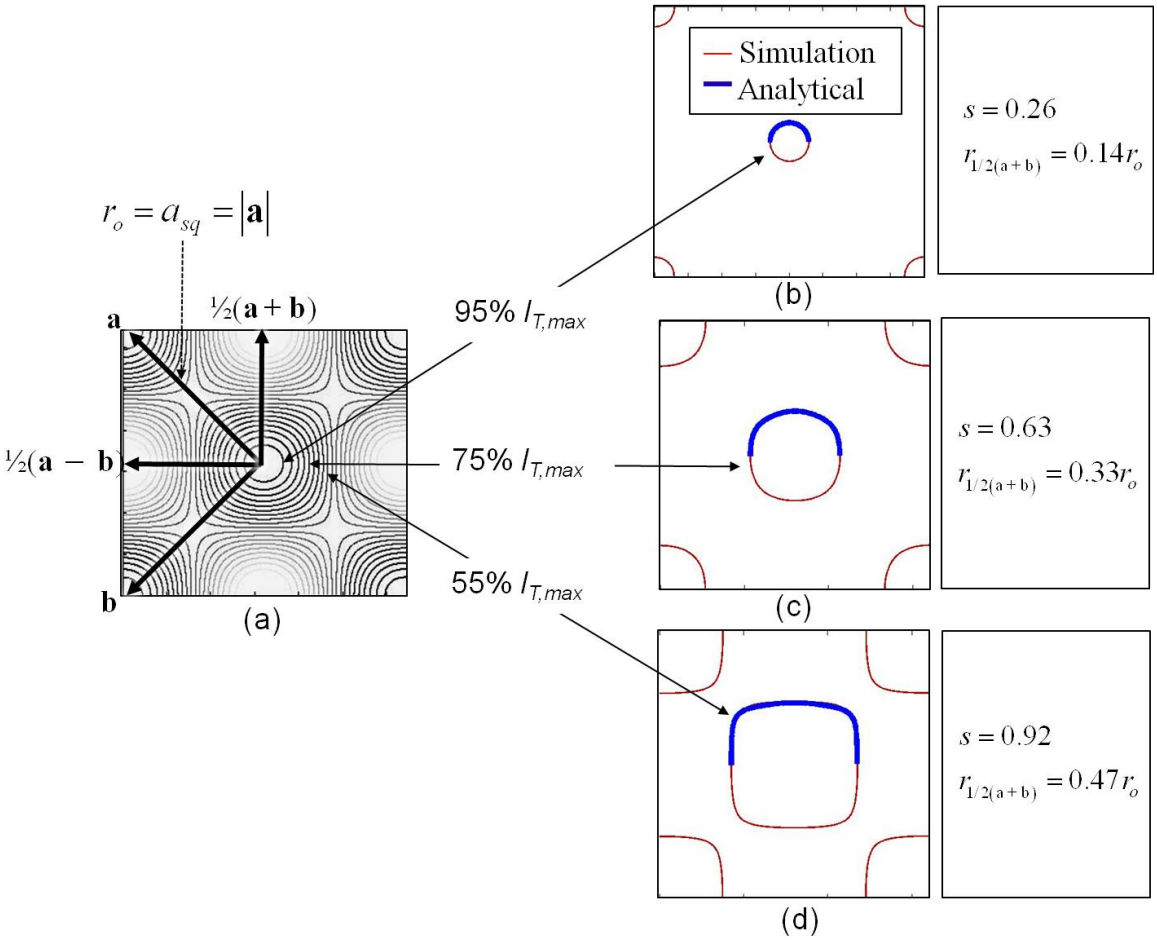

Figure 3.3: Motif geometry for a square-lattice interference pattern with *p4m* plane-group symmetry. (a) Intensity isocontours at 5% intervals of the maximum intensity, $I_{T,max}$, result in lattice points that change between circular (s = 0) and square (s = 1) motif geometries characterized by the radial distances along the **a** and ½(**a** + **b**) lattice-vector directions. Equation (3.17) is plotted against the simulated intensity isocontours at (b) 95%$I_{T,max}$, (c) 75%$I_{T,max}$, and (d) 55%$I_{T,max}$.

3.1.2 Ellipse to Rhombus: *pmm* Plane-Group Symmetry

When interference coefficient constraints are relaxed for the *p4m* symmetry, a square lattice with *pmm* plane-group symmetry emerges provided $V_{23} = 0$. At first glance, the motifs appear to become elliptical and rotated to align with the beam pair producing the

larger interference coefficient value for V_{13} or V_{23}. Typically, these shapes are approximated as a circle, ellipse, rectangle, or rhombus [48,53,108,111,112,294,295]. However, the motif actually changes geometrically between and ellipse and a rhombus as depicted in Fig. 3.4. A more precise analytical model is needed to describe these unique shapes that have the characteristics of both an ellipse and rhombus, to differing degrees.

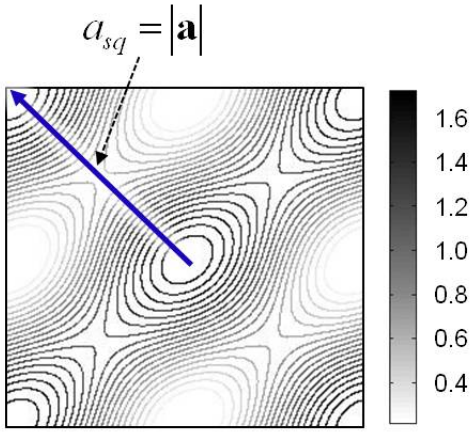

Figure 3.4: Simulated square-lattice interference pattern with *pmm* plane-group symmetry. Intensity isocontours at 5% intervals of the maximum intensity, $I_{T,max}$, result in lattice points that change between elliptical and rhombic geometries.

Using the same methodology presented in the previous section for the *p4m* plane-group motif, the development of an analytical expression for the square-lattice *pmm* motif geometry begins with an equation for a rhombus given by

$$\left[1-\frac{(x-my)^2}{r_x^2}\right]^{1/2}\left[1-\frac{(y-mx)^2}{r_y^2}\right]^{1/2}=0, \tag{3.21}$$

where m is now the slope of the parallel sides of the rhombus when the equation is restricted to real values of $x = my \pm r_x$ for $(y-mx)^2 \le r_y^2$ and $y = mx \pm r_y$ for $(x-my)^2 \le r_x^2$. Equation (3.21) may then be factored as before to obtain an expression for a shape that changes between an ellipse (s = 0) and a rhombus (s = 1) as given by

$$s^2\frac{(x-smy)^2(y-smx)^2}{r_a^2 r_b^2}-\left[\frac{(x-smy)^2}{r_a^2}+\frac{(y-smx)^2}{r_b^2}\right]+1=0. \qquad (3.22)$$

Equation (3.22) now contains two defining parameters, m and s. To solve for these two parameters, Eq. (3.22) may evaluated using the $r_{\mathbf{a}}$, $r_{\mathbf{b}}$, and $r_{½(\mathbf{a}+\mathbf{b})}$ radial distances to solve for the m and s parameter values using Matlab. The resulting geometric equation is depicted in Fig. 3.5 and plotted against the simulated interference-pattern intensity at isocontours of 95%, 75%, and 67% of $I_{T,max}$ respectively.

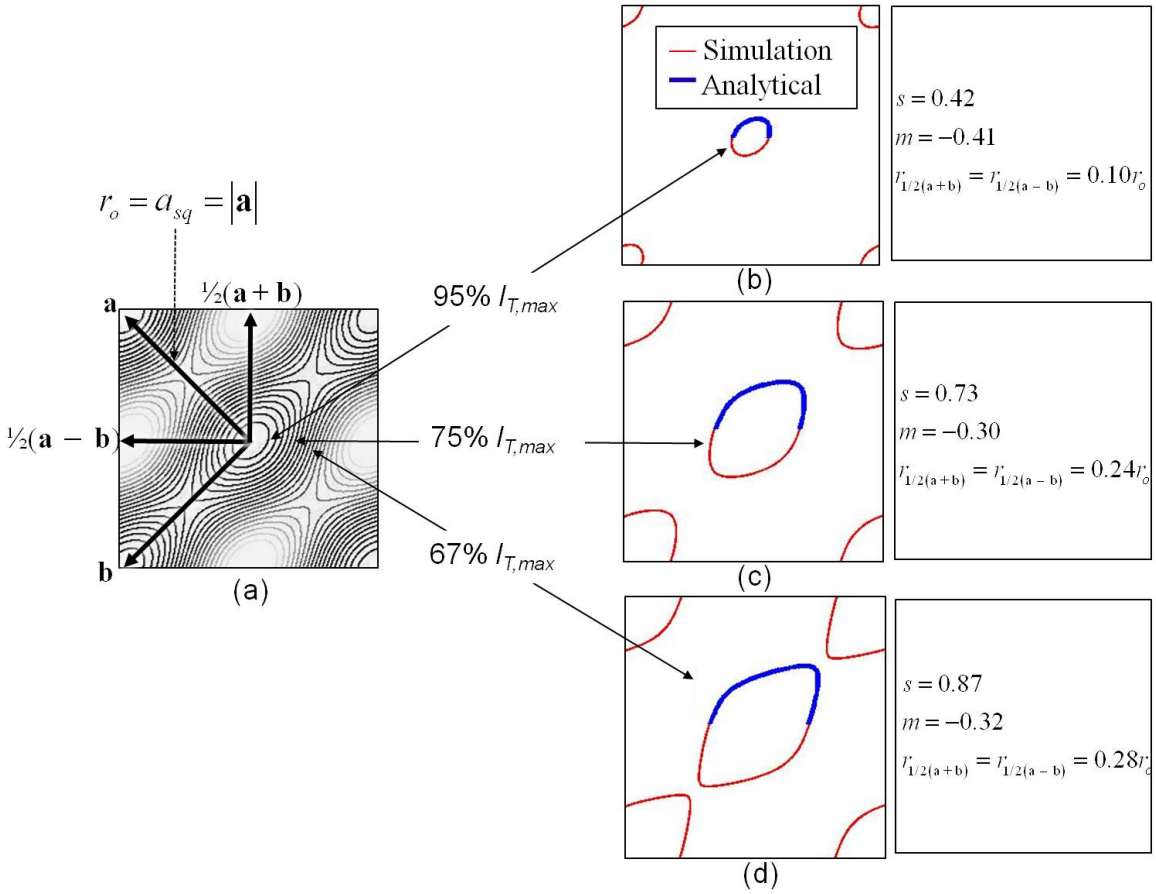

Figure 3.5: Motif geometry for a square-lattice interference pattern with *pmm* plane-group symmetry. (a) Intensity isocontours at 5% intervals of the maximum intensity $I_{T,max}$ results in motif geometries that change between an ellipse (s = 0) and a rhombus (s = 1) characterized by the radial distances along the **a**, **b**, and ½(**a** ± **b**) lattice-vector directions. Equation (3.22) is plotted against the simulated intensity isocontours at (b) 95%$I_{T,max}$, (c) 75%$I_{T,max}$, and (d) 67%$I_{T,max}$.

3.1.3 Ellipse to Hexagon: *p6m*, *p4m* and *cmm* Plane-Group Symmetries

When the beam amplitudes and polarizations are selected to satisfy the conditions for maximum absolute contrast and primitive-lattice-vector-direction equal contrasts for the *p6m* plane-group symmetry ($|\mathbf{a}| = |\mathbf{b}|$, $\mathbf{a}\cdot\mathbf{b} = 0.5$, $V_{12} = V_{13} = V_{23}$), the resulting intensity profile given by Eq. (3.1) is depicted in Fig. 3.6(a). Here, it can be seen that the motif shape changes from that of a circle near the center of a motif to that of a regular hexagon as the contour intervals progress outward radially. When a lattice with square translational symmetry is considered ($|\mathbf{a}| = |\mathbf{b}|$, $\mathbf{a}\cdot\mathbf{b} = 0$) *cmm* plane-group symmetry is again possible under the conditions for optimal absolute contrast and primitive-lattice-vector-direction equal contrasts when $V_{12} = V_{13} = V_{23}$. Again, the motif shape changes from that of a ellipse to that of a general hexagon as depicted in Fig. 3.6(b).

An analytical expression for this transformation between an ellipse and a hexagon begins with an equation for a general hexagon with symmetry about the *y* axis given by

$$\left(1-\frac{x^2}{l^2}\right)^{1/2}\left[1-\frac{\left(y-mx\right)^2}{R^2}\right]^{1/2}\left[1-\frac{\left(y+mx\right)^2}{R^2}\right]^{1/2}, \tag{3.23}$$

where *m* is now the slope of the parallel sides of the top and bottom of the hexagon, *l* is the apothem of the hexagon, and *R* is the circumradius of the hexagon as depicted in Fig. 3.6(e). Based on the geometries of the characteristic hexagon for each motif in Fig. 3.6 (indicated by thick solid lines) expressions for each of the parameters in Eq. (3.23) may be defined by

$$m = \tan\left[\frac{1}{2}\frac{V_{12}}{V_{13}, V_{23}}\cos^{-1}(\mathbf{A}\cdot\mathbf{B})\right], \tag{3.24}$$

$$l = a_{sq,hex}\cos\left[1/2\cos^{-1}\left(\mathbf{A}\cdot\mathbf{B}\right)\right], \tag{3.25}$$

and

$$R = l\left\{m + \tan\left[1/2\cos^{-1}\left(\mathbf{A}\cdot\mathbf{B}\right)\right]\right\}, \tag{3.26}$$

where **A** and **B** are the reciprocal lattice vectors given by Eq. (1.4). Next, Eq. (3.23) may be factored to

$$1 - \frac{x^2}{l^2} - \frac{\left(C_1^{\,2} + C_2^{\,2}\right)}{R^2} + \frac{x^2}{l^2R^2}\left(C_1^{\,2} + C_2^{\,2}\right) + \frac{C_1^{\,2}C_2^{\,2}}{R^4}\left(1 - \frac{x^2}{l^2}\right) = 0, \tag{3.27}$$

where $C_1 = y - mx$ and $C_2 = y + mx$. In this form, Eq. (3.27) may also be used to define rectangular geometries when $m = 0$. For example, when the conditions for *cmm* plane-group symmetry ($V_{12} = V_{13}$, $V_{23} = 0$) are satisfied for the hexagonal translation symmetry as depicted in Fig. 3.6(c), the motif shape changes from that of an ellipse to that of a rectangle. In fact, this same equation may also be used to model the *p4m* plane group symmetry discussed previously in Sec. 3.1.1. In this case $m = 0$ and $l = R$ and the hexagon collapses into a square as depicted in Fig. 3.6(d).

To allow for a transformation to an ellipse, an s parameter may again be incorporated into Eq. (3.27) and C_1 and C_2 to obtain

$$1 - \frac{x^2}{l^2} - \frac{1}{2}\frac{\left(C_1^{\,2} + C_2^{\,2}\right)}{R^2} + s^2\left[\frac{x^2}{l^2R^2}\left(C_1^{\,2} + C_2^{\,2}\right) + \frac{C_1^{\,2}C_2^{\,2}}{R^4}\left(1 - \frac{x^2}{l^2}\right) - \frac{1}{2}\frac{\left(C_1^{\,2} + C_2^{\,2}\right)}{R^2}\right] = 0, \tag{3.28}$$

and

$$C_1 = y - smx \text{ and } C_2 = y + smx. \tag{3.29}$$

Equation (3.28) now represents a general expression that describes the motif shapes in Fig. 3.6 that change between an ellipse ($s = 0$) and a hexagon ($s = 1$) with mirror symmetry about the x and y axes. In this form, the l and R parameters are given by

$$l = r_{1/2(a\,-\,b)} \text{ and } R = r_{1/2(a\,+\,b)}. \tag{3.30}$$

Equation (3.28) may be evaluated using the radial distances $r_{\mathbf{a}}$ or $r_{\mathbf{b}}$ to determine the required s parameter value.

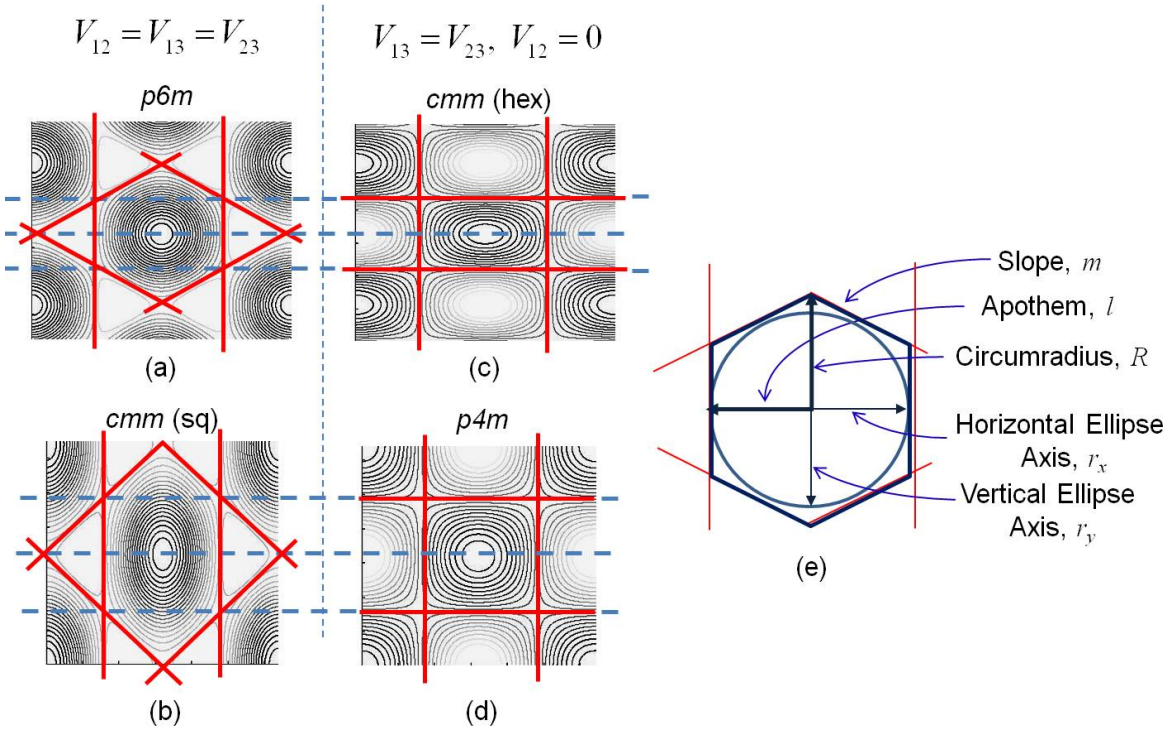

Figure 3.6: Simulated interference patterns with *p6m,* c*mm*, and *p4m* plane-group symmetries. Intensity isocontours at 5% intervals of the maximum intensity $I_{T,max}$ result in motif geometries that change between elliptical and hexagonal for the (a) *p6m* and (c) *cmm* plane group symmetries for a lattice with hexagonal symmetry. Lattice point geometries also change between an ellipse and a hexagon for the (b) *cmm* and (d) *p4m* plane group symmetries associated with a lattice with square translational symmetry. Solid lines depict the orientations of the characteristic hexagon for each motif while dashed lines indicate points of symmetry between patterns with a common translational symmetry. (e) The basic hexagonal geometry is defined by the apothem l along the x axis, the circumradius R along the y axis, and the slope m of the top and bottom parallel sides of the hexagon.

Equation (3.28) is plotted against the simulated interference-pattern intensity at specific isocontours as a percentage of $I_{T,max}$ for the hexagonal-lattice *p6m* and *cmm* symmetries and the square-lattice *cmm* symmetry in Figs. 3.7-3.9, respectively. Again, it is clear that Eq. (3.28) provides an excellent representation of the motif geometry as it changes from an ellipse (s = 0) to a hexagon or rectangle (s = 0).

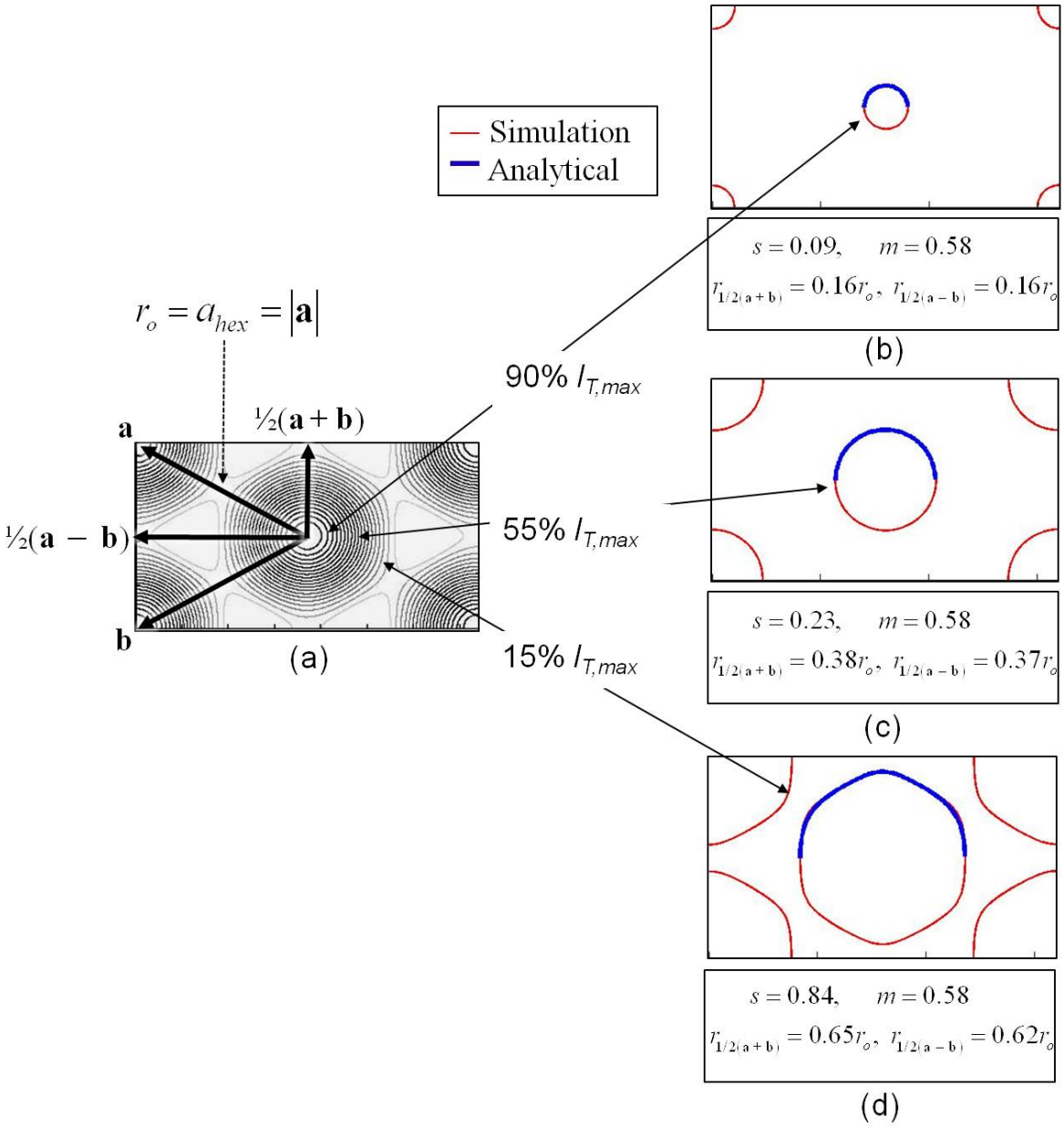

Figure 3.7: Motif geometry for a hexagonal-lattice interference pattern with *p6m* plane-group symmetry. (a) Intensity isocontours at 5% intervals of the maximum intensity $I_{T,max}$ results in motif geometries that change between an circle (s = 0) and a regular hexagon (s = 1) characterized by the radial distances along the **a**, ½(**a** + **b**), and ½(**a** − **b**) lattice-vector directions. Equation (3.28) is plotted against the simulated intensity isocontours at (b) 90%$I_{T,max}$, (c) 55%$I_{T,max}$, and (d) 15%$I_{T,max}$.

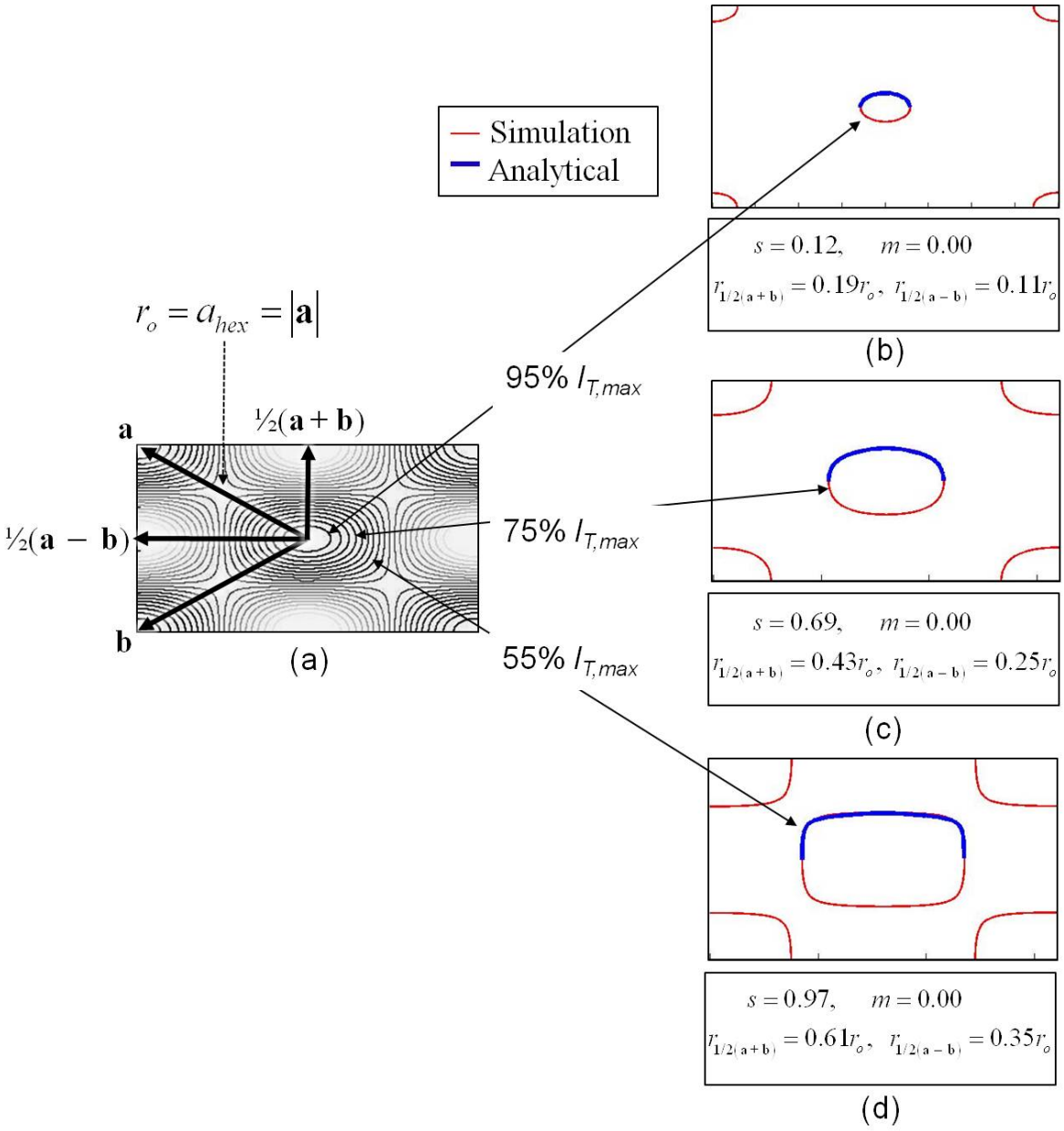

Figure 3.8: Motif geometry for a hexagonal-lattice interference pattern with *cmm* plane-group symmetry. (a) Intensity isocontours at 5% intervals of the maximum intensity $I_{T,max}$ results in motif geometries that change between an ellipse (s = 0) and a hexagon (s = 1) characterized by the radial distances along the **a**, ½(**a** + **b**), and ½(**a** − **b**) lattice-vector directions. Equation (3.28) is plotted against the simulated intensity isocontours at (b) 95%$I_{T,max}$, (c) 75%$I_{T,max}$, and (d) 55%$I_{T,max}$.

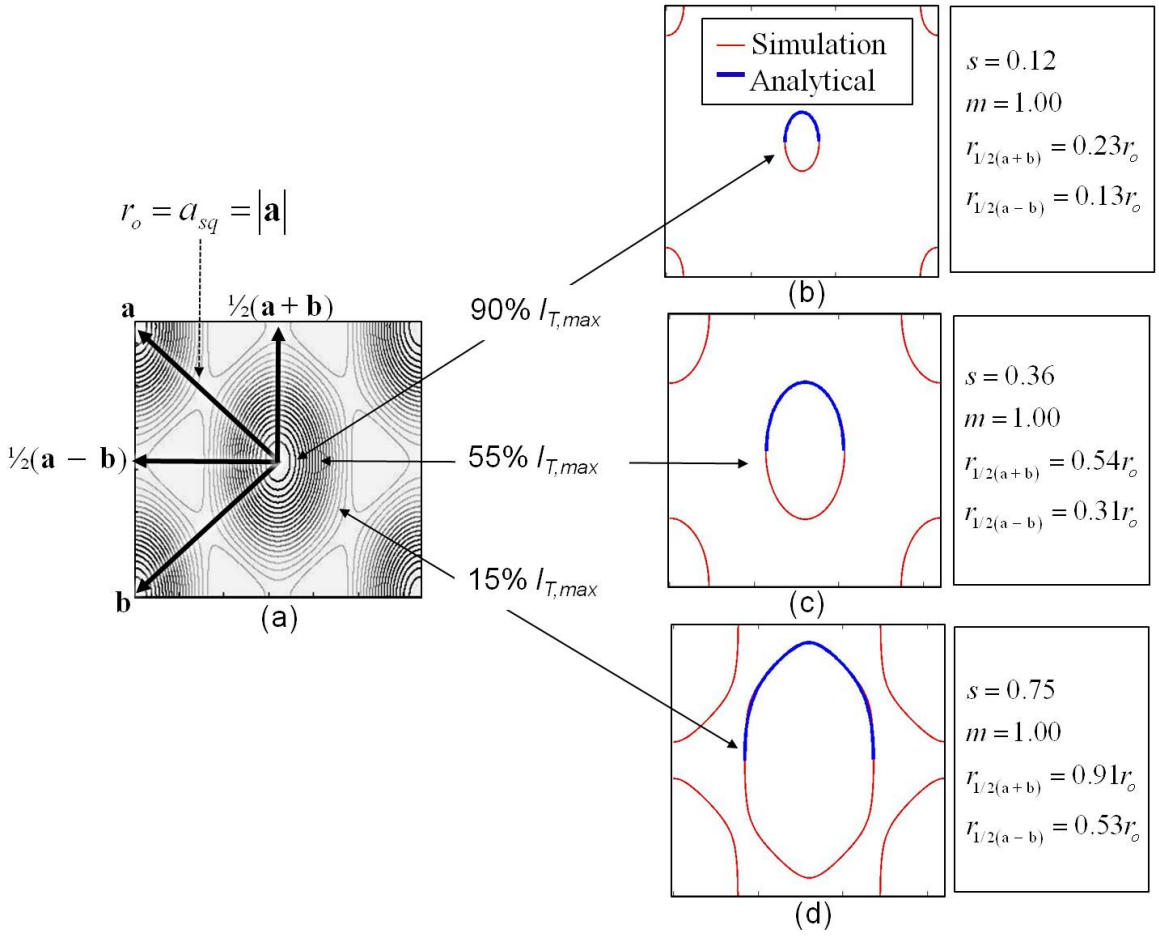

Figure 3.9: Motif geometry for a square-lattice interference pattern with *cmm* plane-group symmetry. (a) Intensity isocontours at 5% intervals of the maximum intensity $I_{T,max}$ results in motif geometries that change between an ellipse (s = 0) and a hexagon (s = 1) characterized by the radial distances along the **a**, ½(**a** + **b**), and ½(**a** − **b**) lattice-vector directions. Equation (3.28) is plotted against the simulated intensity isocontours at (b) 90%$I_{T,max}$, (c) 55%$I_{T,max}$, and (d) 15%$I_{T,max}$.

3.2 Experimental Demonstration

An experiment was conducted to determine the feasibility of recording an interference pattern with a specific motif geometry. For this experiment the multi-beam amplitude-splitting configuration reported previously by our group [69] was used to record a square-lattice interference pattern in a 2μm layer of SU-8 2002 photoresist polymer [298] on a UV-grade fused silica sample. For this configuration, a 40x Newport microscope

objective [299] was placed at the intersection of the three interfering beams such that the beams entered at the front of the lens assembly, serving to enlarge the interference-pattern periodicity by reducing the angle of incidence, θ [152]. The larger interference pattern was used to allow for more accurate images of the individual motifs. For this experiment, the resulting incidence angle was calculated to be $\theta = 2.46 deg$, resulting in a lattice constant, a_{sq}, of approximately $6 \mu m$.

Samples were prepared, exposed, and developed using procedures reported previously by our group [82]. The processed samples were coated with approximately $30 nm$ of Au using the Hummer 6 Sputterer [300] and imaged using the LEO 1530 scanning electron microscope (SEM) [301] located in the Pettit Microelectronics Building Cleanroom. Figures 3.10(a) and (b) depict the Matlab simulated interference pattern and the resulting experimental SEM pattern image respectively. For this experiment, each interfering beam was adjusted for equal amplitude and a common beam polarization angle of $90 deg$. While the experimental sample did not form idealized motifs, the shapes did allow a general comparison with the models developed in this section.

The analytical motif geometry model is plotted in Fig. 3.11(a) at a intensity threshold of 19% of $I_{T,max}$ representing an approximate match to the fabricated motif dimensions depicted in Fig. 3.11(b). Here, the actual motif radial values match the predicted values within 5% of the predicted analytical model value. These basic experimental results suggest that the analytical motif geometry equations developed in the research presented here provide a simple and accurate model to predict the actual motifs possible with three-beam interference.

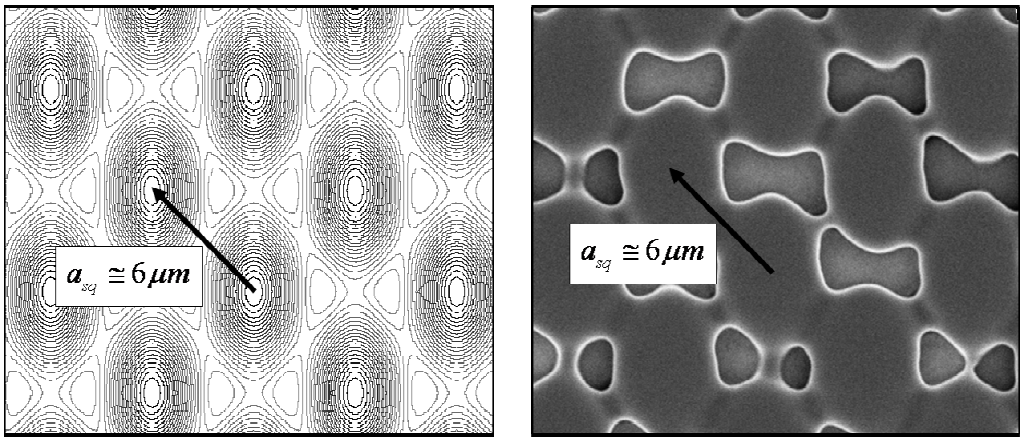

Figure 3.10: Motif geometry experimental pattern. (a) A Matlab simulation depicts a square-lattice with $6\mu m$ periodicity. (b) An SEM image depicts an interference pattern recorded in SU-8 2002 on a fused silica sample and sputtered with $30nm$ of Au.

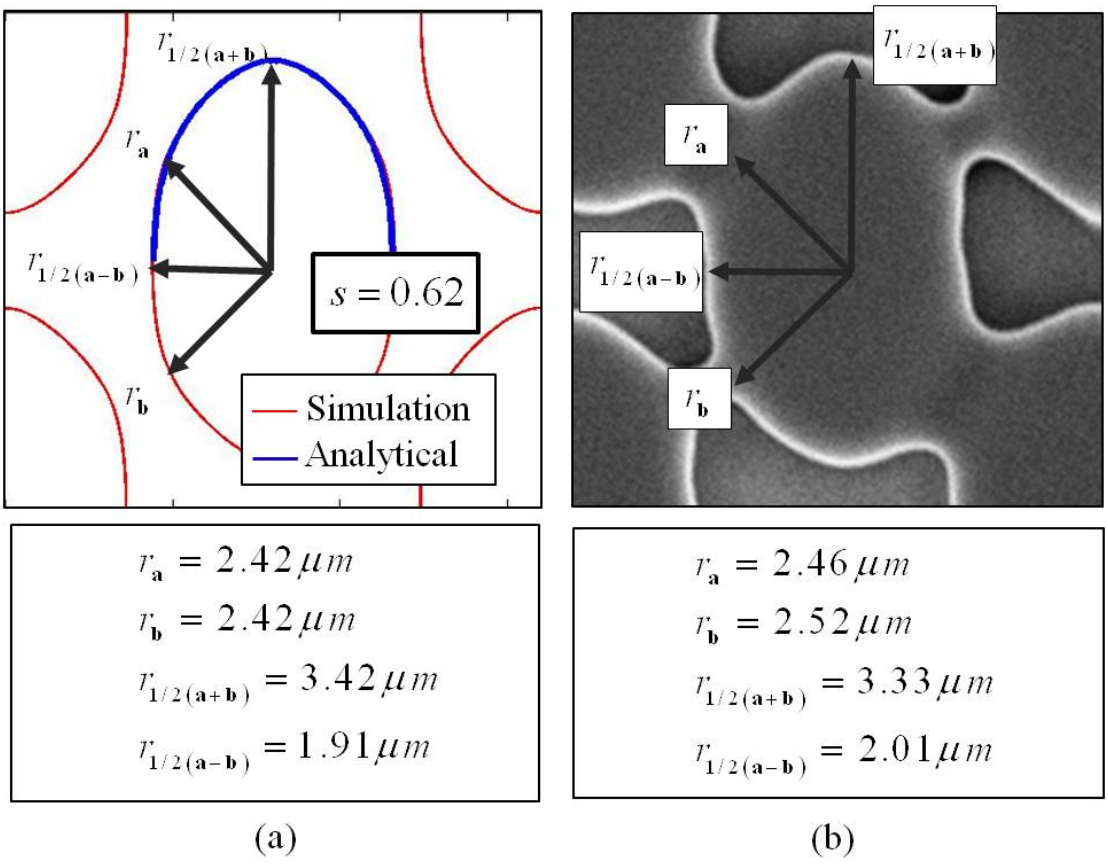

Figure 3.11: Motif geometry experimental results. (a) A Matlab simulation depicts a square-lattice with $6\mu m$ periodicity at $19\%I_{T,max}$ intensity isocontours. The analytical motif model is plotted over the contour line with a *s*-parameter value of 0.62. (b) An SEM image depicts an interference pattern recorded in SU-8 2002. The radial values for the experimental motif match within 5% of the analytical model predicted values.

3.3 Summary

In this chapter, analytical models were developed for the motif geometries associated with the four higher-order plane-group symmetries possible for both square and hexagonal lattices, under the conditions for primitive-lattice-vector-direction equal contrasts in linearly-polarized, three-beam interference. The two fundamental geometric equations and the relationships between the plane-group symmetries are depicted in Fig. 3.12.

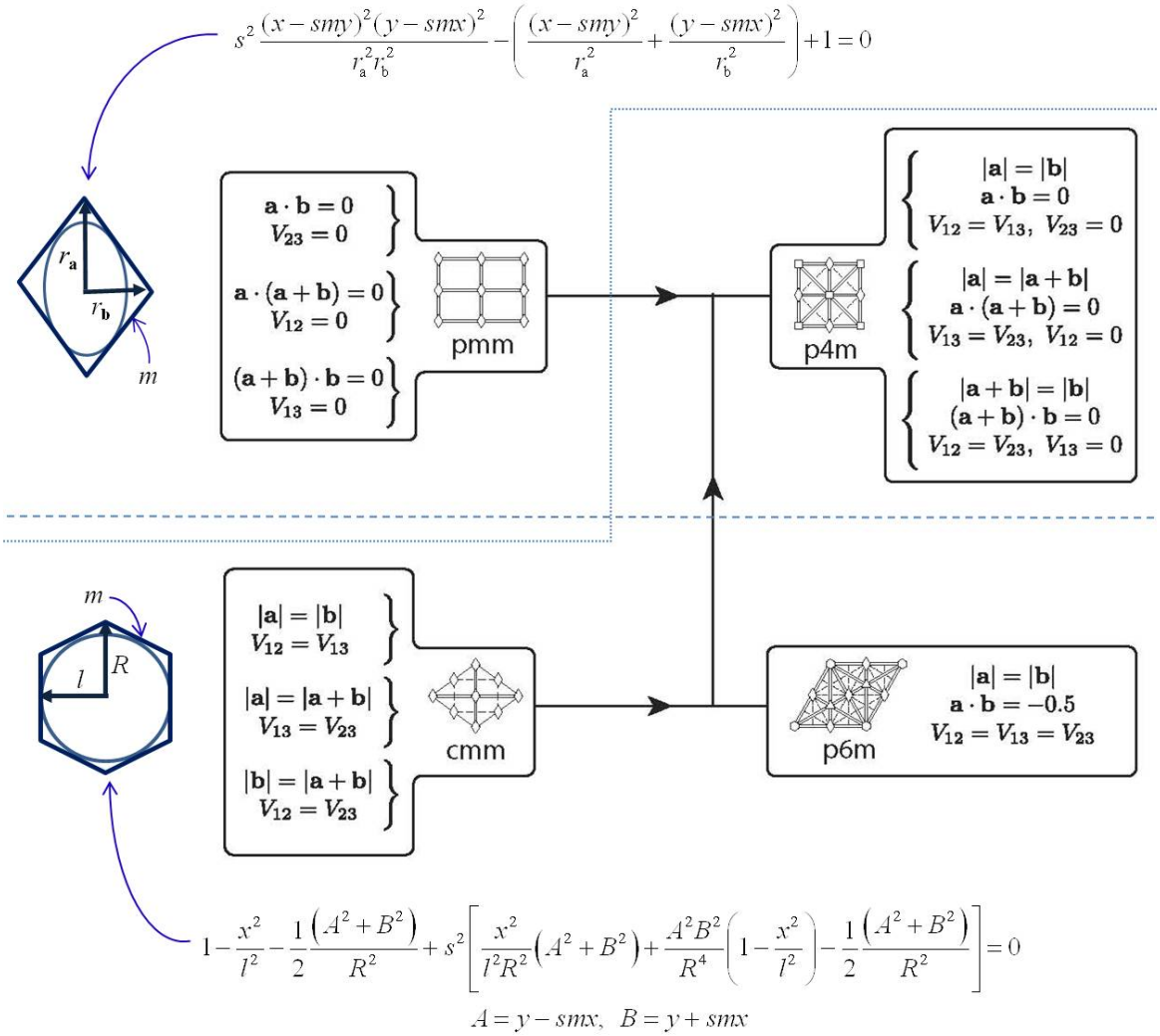

Figure 3.12: Motif geometry models for higher-order symmetries under the conditions for primitive-lattice-vector-direction equal contrasts in linearly-polarized, three-beam interference.

Of course, the lowest order plane-group symmetry, *p2*, is always possible with three-beam interference. The methodology and fundamental models developed as a part of this research may be further modified or combined to describe these motif geometries that change from the shape of an ellipse to that of an irregular polygon. Given these new analytical descriptions of the motif geometries, researchers may analyze directly the effects of wide range of motif geometries for a particular application using the analytical model alone, without the need for complicated experimentation or computer simulations.

CHAPTER 4

CONSTRAINED PARAMETRIC OPTIMIZATION

With a thorough understanding of three-beam plane-group symmetries and accurate descriptions of the motif geometries provided by the present research, it is important to understand fully the effects of constraints on individual beam parameters for a particular given multi-beam interference (MBI) configuration. Here, this information will inform the design of the Pattern-Integrated Interference Exposure System (PIIES).

The important characteristics of the two main MBI configuration categories, wavefront-dividing and amplitude-splitting, are summarized in Table 4.1. As a result of the relatively short optical path lengths in wavefront-dividing configurations, these methods are essentially phase-locked, representing the most interferometrically stable option for MBI. However, in most wavefront-dividing schemes, control over individual beam amplitudes and polarizations is typically limited and wavevector configurations are generally fixed. By comparison, multiple-beam-splitting configurations typically provide the ability to reconfigure the wavevector configuration for a wide range of lattice constants and translational symmetries, while allowing for individual control over beam parameters. However, a common drawback of beam-splitting-based configurations is the potential for interferometric instability. Any perturbations to the optical components, optical path lengths, or relative phases of the interfering beams may result in a translation of the pattern or change in the symmetry of the unit cell. Thus, pattern stability is generally low for amplitude-splitting schemes.

Table 4.1: Comparison of MBI configuration categories.

Configuration Category	Configuration Characteristics			
	Interferometric Stability?	Reconfigurable?	Individual Beam Conditioning?	Full Patterning Capabilities?
Wavefront-Dividing	High	No	Limited	?
Beam-Splitting	Low	Yes	Yes	Yes

From Table 4.1 it is clear that the two MBI configuration categories have advantages and disadvantages. Although most MBI configurations are not easily reconfigured, they may all be designed to provide one of a wide range of periodicities and translational symmetries based on a fixed wavevector configuration. However, these same systems are characteristically limited in their ability to condition the individual beams. In this case, it is not clear that full patterning capability and sufficient contrast remain as constraints are placed on beam amplitudes and polarizations.

In the present work, constraints on individual beam amplitudes and polarizations are systematically considered to understand their effects on lithographically useful MBI periodic patterning possibilities. A method for analyzing parametric constraints is presented and used to compare the optimized optical-intensity distributions for representative constrained systems, under the conditions for primitive-lattice-vector-direction equal contrast [58]. Case studies are presented for both square and hexagonal-lattices produced via three-beam interference. Results demonstrate that constraints on individual-beam polarizations significantly impact patterning possibilities and must be considered in the systematic design of an MBI system. This research has resulted in three journal papers [69,71,79] and one conference paper [77].

4.1 Parametric Constraints

To optimize this contrast of the three-beam optical-intensity distribution given by Eq. (3.1), the conditions for primitive-lattice-vector-direction equal contrasts result in a constrained optimization problem to determine the polarization vector values for each recording wavevector [59]. Once the polarization vector orientations are determined, the required amplitudes may be determined. These constrained optimization requirements for beam amplitudes and polarizations are summarized in Table 4.2 for the *p4m*, *cmm*, and *p6m* plane-group symmetries possible with square and hexagonal-lattice translational symmetries as depicted earlier in Fig. 3.1. It is noted that *cmm* plane-group symmetry is possible for both square and hexagonal lattices. For this reason the two are differentiated here by *cmm*(sq) and *cmm*(hex), respectively. Of course, lower order symmetries are also satisfied under the conditions listed in Table 4.2. For example, *pmm* symmetry is satisfied with the *p4m* plane-group, while *p2* symmetry is satisfied for all cases. For the purposes of the research presented here, only the higher-order symmetries are analyzed.

Table 4.2: Constraints for maximum absolute contrast under the conditions for primitive-lattice-vector-direction equal contrasts.

Translational Symmetry	Plane-Group Symmetry	Optimization Constraints
Square	*p4m*	maximize $\frac{e_{13}e_{23}}{\sqrt{e_{13}^2+e_{23}^2}}$, $e_{12}=0,\ E_1=\frac{e_{23}}{e_{13}}E_2$
Hexagonal	*cmm*(hex)	$\left(V_{13}=V_{23},\ V_{12}=0\right)$
Square	*cmm*(sq)	maximize $\frac{2e_{12}e_{13}e_{23}}{e_{12}^2+e_{13}^2+e_{23}^2}$, $E_1=\frac{e_{23}}{e_{12}}E_3,\ E_2=\frac{e_{13}}{e_{12}}E_3$
Hexagonal	*p6m*	$\left(V_{13}=V_{23}=V_{12}\right)$

Under the conditions for primitive-lattice-vector-direction equal contrasts, the individual linear polarization vectors, $\hat{\mathbf{e}}_i$, are defined according to the polarization vector basis depicted in Fig. 4.1. Using this basis, each polarization vector is given by [56]

$$\hat{\mathbf{e}}_i = \mathbf{R}_z(-\varphi_i)\mathbf{R}_y(-\theta_i)\mathbf{R}_z(-\psi_i)\mathbf{R}_y(\theta_i)\mathbf{R}_z(\varphi_i)(\hat{\mathrm{z}}\times\mathbf{k}_i), \tag{4.1}$$

where θ_i and φ_i are the spherical coordinates of the wavevector $\mathbf{k}_i$, ψ_i is the counter-clockwise angular rotation of the polarization vector (looking antiparallel to the wavevector), and $\mathbf{R}_z(\beta)$ and $\mathbf{R}_y(\beta)$ are rotation matrices given by

$$\mathbf{R}_z(\beta) = \begin{pmatrix} \cos\beta & \sin\beta & 0 \\ -\sin\beta & \cos\beta & 0 \\ 0 & 0 & 1 \end{pmatrix}, \text{ and} \tag{4.2}$$

$$\mathbf{R}_y(\beta) = \begin{pmatrix} \cos\beta & 0 & -\sin\beta \\ 0 & 1 & 0 \\ \sin\beta & 0 & \cos\beta \end{pmatrix}. \tag{4.3}$$

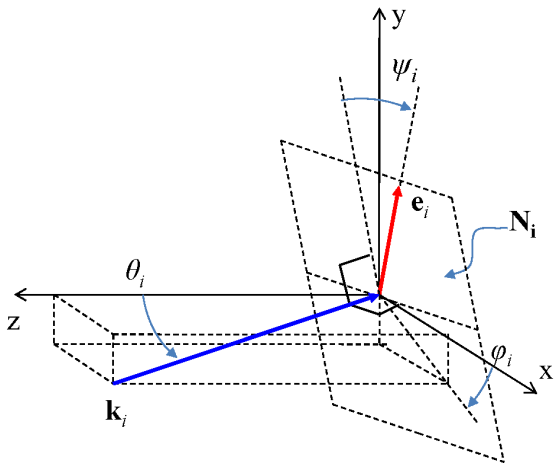

Figure 4.1: Orientation of basis vectors to define linear polarizations. θ_i and φ_i are the spherical coordinates of the wavevector, $\mathbf{k}_i$. The polarization vector, $\hat{\mathbf{e}}_i$, is contained in the plane $\mathbf{N}_i$ orthogonal to the wavevector, and defined by the counter-clockwise angular rotation, ψ_i, of the polarization vector (looking antiparallel to the wavevector).

To find the optimal set of polarization vectors for a given plane-group symmetry, objective functions were developed for each of optimization constraints listed in Table 4.2 to solve for the conditional maximum. In this method, Lagrangian multipliers, Ω, are used to implement constraints to the objective function [55] (λ is normally used as the symbol for a Lagrangian multiplier; however, Ω is used here to differentiate the multiplier from the freespace wavelength, λ). The resulting objective functions for maximum absolute contrast under the conditions for primitive-lattice-vector-direction equal contrasts are given in Table 4.3.

Table 4.3: Optimization functions for optimal absolute contrast and primitive-lattice-vector-direction equal contrasts assuming individual control over beam amplitudes and polarizations.

Plane-Group Symmetry	Objective Function
p4m, cmm(hex)	$f\left(\psi_1,...,\psi_3,\Omega_1\right)=e_{13}e_{23}/\sqrt{e_{13}^2+e_{23}^2}+\Omega_1 e_{12}$
p6m, cmm(sq)	$f\left(\psi_1,...,\psi_3\right)=2e_{12}e_{13}e_{23}/\left(e_{12}^2+e_{13}^2+e_{23}^2\right)$

4.1.1 Amplitude Constraints

Several representative three-beam interference configurations are depicted in Fig. 4.2. Figures 4.2(a) and (b) represent amplitude-dividing configurations as discussed in more detail in Chapter 2. In the case of the beam-splitting configuration in Fig. 4.2(c), a half-wave plate rotates the plane of the input linearly polarized light, thereby allowing control over the amplitude, E_i, of output beam from each polarizing cube beamsplitter [69]. In other configurations, individual-beam amplitudes may be controlled using attenuating-transmission materials in the path of each interfering beams.

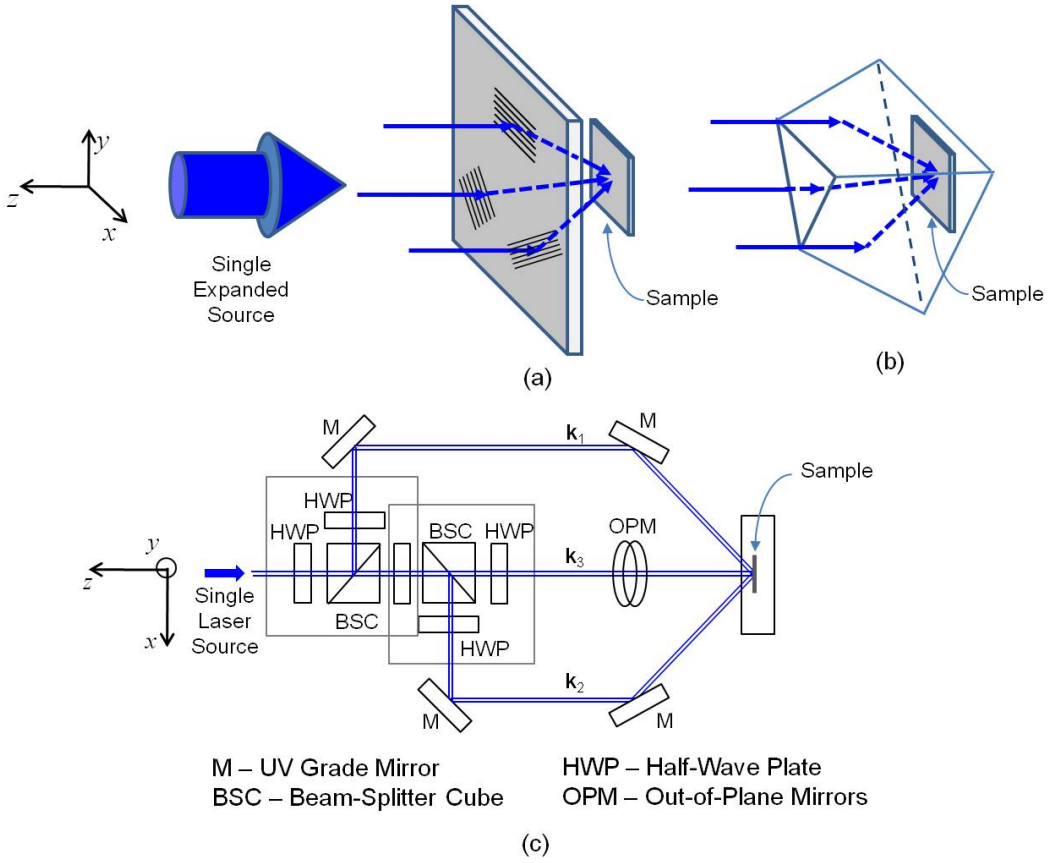

Figure 4.2: Three-beam interference configurations. (a) A diffractive-grating mask diffracts portions of the incident expanded beam such that the first-order diffracted beams intersect and interfere at the sample plane [62]. (b) A prism is used to divide and refract different portions of an incident collimated beam [70]. (c) A beam-splitter-based system provides individual control of beam amplitudes and polarizations [69].

In many configurations it is difficult to set specific amplitudes for each individual beam. For example, most wavefront-splitting schemes result in multiple beams with a common or a fixed ratio of amplitude values. Accordingly, the first constraint considered here is the case of *equal-individual-beam amplitudes*, $E_1 = E_2 = E_3$. Based on the amplitude constraints given by Table 4.2, an additional constraint of $e_{13} = e_{23}$ results for the *p4m* and *cmm*(hex) plane group symmetries. For *p6m* and *cmm*(sq) plane group

symmetries, the additional constraint is $e_{12} = e_{13} = e_{23}$. The resulting simplified objective functions for the case of *equal-individual-beam amplitudes* are given in Table 4.4.

Table 4.4: Optimization functions for optimal absolute contrast and primitive-lattice-vector-direction equal contrasts with *equal-individual-beam amplitudes*.

Plane-Group Symmetry	Objective Function
p4m, cmm(hex)	$f(\psi_1,...,\psi_3,\Omega_1,\Omega_2) = \frac{1}{3}e_{13} + \Omega_1(e_{13} - e_{23}) + \Omega_2 e_{12}$
p6m, cmm(sq)	$f(\psi_1,...,\psi_3,\Omega_1,\Omega_2) = \frac{2}{3}e_{13} + \Omega_1(e_{12} - e_{13}) + \Omega_2(e_{13} - e_{23})$

4.1.2 Polarization Constraints

In addition to the ability to set the individual beam amplitudes, the configuration of Fig. 4.2(c) allows for control over individual-beam linear polarizations as required for maximum absolute contrast and primitive-lattice-vector-direction equal contrasts. This is accomplished with the final half-wave plate in the path of each beam. However, in most MBI configurations it is usually difficult to set the polarization for each beam individually. Typically, a single linearly-polarized beam is divided into the multiple beams as depicted in Figs. 4.2(a) and (b), with each beam retaining the original linear polarization angle of the source beam, ψ_B. The individual-beam polarization is then defined by Eq. (4.1) where $\psi_1 = \psi_2 = \psi_3 = \psi_B$ representing the first polarization constraint considered here for *equal individual beam-set polarizations*.

Alternatively, it may be possible to improve patterning possibilities or absolute contrast through the use of a single polarizer just prior to the sample plane to set a common polarization for each beam as depicted in Fig. 4.3(a). For this case, the individual beam-polarization vectors are determined by finding the vector, $\mathbf{e}_i$,

perpendicular to the wavevector, $\mathbf{k}_i$, that is contained in the polarization plane, **R**, defined by the origin (0,0,0), the vector defining the pass axis of the polarizer, **P**, and the wavevector, $\mathbf{k}_i$, as depicted in Fig. 4.3(b). Here, the polarization pass axis vector is defined as

$$\mathbf{P} = \sin(-\alpha_P)\hat{x} + \cos(-\alpha_P)\hat{y}\,, \tag{4.4}$$

where $-\alpha_P$ is the angle of the pass axis of the polarizer with respect to the y axis. The polarization vector, $\mathbf{e}_i$, is then the intersection of the polarization plane, $\mathbf{R}_i$, and the plane orthogonal to the wavevector, $\mathbf{N}_i$. This intersection is found by taking the cross product of the normals, $\mathbf{n}_R$ and $\mathbf{n}_N$, for each of the planes. With this polarization vector basis, the individual-beam polarization vectors for each wavevector are given by

$$\mathrm{e}_i = \mathrm{k}_i \times \left(\left[\sin(-\alpha_i)\hat{x} + \cos(-\alpha_i)\hat{y} \right] \times \mathrm{k}_i \right), \tag{4.5}$$

where $\alpha_1 = \alpha_2 = \alpha_3 = \alpha_P$ for the second polarization constraint considered in this study, *equal sample-plane-set polarization*. For the two polarization constraints, the new polarization vector definitions and required constraints are presented in Table 4.5.

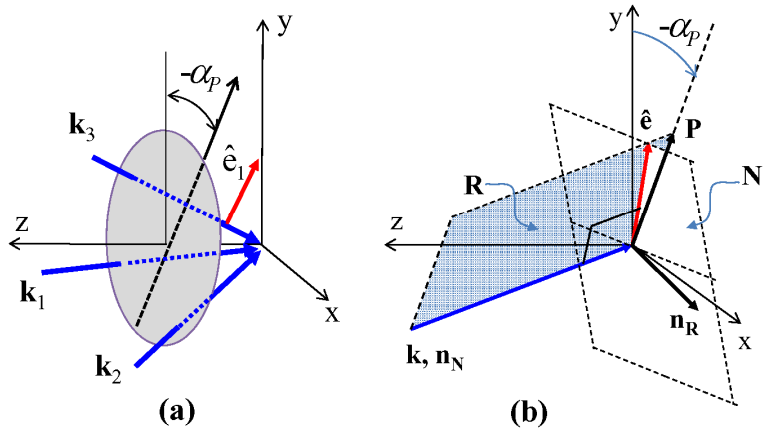

Figure 4.3: Orientation of basis vectors for sample-plane-set polarization. (a) A single linear polarizer, with a pass axis angle, $-\alpha_P$, may be placed just prior to the sample plane to improve contrast. (b) The plane, **R**, contains the wavevector, **k**, and the polarization pass axis vector, **P**. The polarization vector, **ê**, is then the intersection of the polarization plane, **R**, and the plane orthogonal to the wavevector, **N**.

Table 4.5: Polarization vector definitions and constraints for optimal absolute contrast and primitive-lattice-vector-direction equal contrasts for unconstrained, *equal individual beam-set polarization*, and *equal sample-plane-set polarization*.

Polarization Case	Polarization Vector Definition	Constraints
Optimal Individual Beam-Set Polarization	$\hat{\mathbf{e}}_i = \mathbf{R}_z(-\varphi_i)\mathbf{R}_y(-\theta_i)\mathbf{R}_z(-\psi_i)\mathbf{R}_y(\theta_i)\mathbf{R}_z(\varphi_i)(\hat{\mathrm{z}}\times\mathbf{k}_i)$	None
Equal Individual Beam-Set Polarizations		$\psi_1 = \psi_2 = \psi_3 = \psi_B$
Equal Sample-Plane-Set Polarizations	$\hat{\mathbf{e}}_i = \mathbf{k}_i \times \left(\left[\sin(-\alpha_i)\hat{x} + \cos(-\alpha_i)\hat{y} \right] \times \mathbf{k}_i \right)$	$\alpha_1 = \alpha_2 = \alpha_3 = \alpha_P$

4.2 Constrained Optimization Results

The constrained optimization functions in Table 4.3 and Table 4.4 were solved using the polarization definitions and constraints given in Table 4.5 for both square- and hexagonal-lattice space-group symmetries across the full range of common incidence angles. The optimized constrained parameter values were then used to evaluate the resulting optical-intensity distribution and maximum absolute contrast given by Eqs. (3.1) and (1.8) as a function of the common sample-plane incidence angle. For the unconstrained case of *optimal individual beam amplitudes* and *optimal individual beam-set polarization*, unity absolute contrast, $V_{abs} = 1$, is achieved across the full range of possible lattice constants for all plane-group symmetries as predicted by the conditions for primitive-lattice-vector-direction equal contrast [59]. For the *cmm*(sq) and *p6m* symmetries, unity contrast is possible when the intensity profile is inverted, that is, when

the points of intensity maxima become intensity minima. This result is obtained when the product of the three interference coefficients given by Eq. (1.3) are allowed to be negative in value. If the *cmm*(sq) and *p6m* symmetries are optimized for intensity maxima at the lattice points, the optimal absolute contrast varies from 0.6 to unity. Typically, optical lithography requires an absolute contrast 0.4 to 0.8 or higher to resolve the required features based on the photoresist properties, feature sizes, and coherence of the source [302]. With the unconstrained case as baseline for comparison, the various combinations of constraints considered in the present research are listed in Table 4.6.

Table 4.6: Summary of cases when each beam is set optimally for amplitude and polarization, constrained to an equal amplitude for all beams, constrained to an equal polarization for all beams, or constrained to an equal sample-plane-set polarization for all beams.

	Amplitude and Polarization Constraints				
	Optimal Individual Beam Amplitude	Equal Individual Beam Amplitudes	Optimal Individual Beam-Set Polarization	Equal Individual Beam-Set Polarizations	Equal Sample-Plane-Set Polarizations
Case 1	X		X		
Case 2		X	X		
Case 3	X			X	
Case 4		X		X	
Case 5	X				X
Case 6		X			X

4.2.1 Amplitude Constraints

When the *equal-individual-beam amplitudes* constraint is considered, all plane-group symmetries are again possible across the full range of common incidence angles. However, the maximum absolute contrast is now limited to $V_{abs} = 0.94$ for *p4m* and *cmm*(hex) symmetries, while the *cmm*(sq) is limited to a value ranging from 0.88 to

unity. The *p6m* absolute contrast remains unchanged. This stems from the fact that the unconstrained *p6m* optimization requires amplitude values of $\pm E_1 = E_2 = E_3$ [59].

4.2.2 Polarization Constraints

A significant reduction in patterning possibilities and absolute contrasts occurs when polarization constraints are considered. These limitations are made more constrictive when combined with the amplitude constraint. To demonstrate the effect of polarization constraints, Figs. 4.4(a)-(f) plot the maximum absolute contrast, V_{abs}, for the unconstrained case against the various constrained case combinations for *p4m*, *cmm*(hex), *p6m*, and *cmm*(sq) plane-group symmetries, respectively. In each graph, the absolute contrast is plotted as a function of the common wavevector incidence angle at the sample plane. The unconstrained and the amplitude-constrained case (labeled "Equal Amplitudes" for *equal-individual-beam amplitudes*) are plotted as a baseline for comparison.

Beginning with the *p4m* plane-group in Fig. 4.4(a), both polarization constraints (labeled "Equal Polarizations" for *equal individual beam-set polarizations* and "Sample-Plane-Set Polarizations" for the *equal sample-plane-set polarizations*) limit the range of incidence angles to $45\,deg$ and higher in order to produce this symmetry. Furthermore, the absolute contrasts drop off sharply from a unity value at $45\,deg$. In the case of *equal individual beam-set polarizations*, the contrast drops to zero at a common incidence angle near $\theta \approx 66\,deg$. If a conservative absolute contrast of $V_{abs} = 0.4$ is used a minimum threshold for optical lithography purposes, the range of angles for *p4m* symmetry is reduced to $45 \leq \theta < 57\,deg$ or $76 < \theta < 90\,deg$, and $45 \leq \theta < 68\,deg$ for the two polarization constraints, respectively. If a common UV i-line source is used at $\lambda =$

363.8 nm, the resulting range of periodicities, using Eq. (3.5), is then 363.8 ≥ a_{sq} > 306.7 nm or 265.1 > a_{sq} > 257.2 nm, and 363.8 ≥ a_{sq} > 277.4 nm. Finally, if the *equal-individual-beam amplitudes* is combined with either of the polarization constraints, the ability to achieve *p4m* symmetry is limited to a single incidence angle of $\theta = 45\,deg$ ($a_{sq} = \lambda$). Similar results are obtained for the *cmm*(hex) symmetry as depicted in Fig. 4.4(b). However, when the *equal-individual-beam amplitudes* is combined with either of the polarization constraints, the *cmm*(hex) symmetry (with $V_{13} = V_{23}$ and $V_{12} = 0$) is not possible.

For the *p6m* plot in Fig. 4.4(c) the maximum absolute contrast begins near unity at a zero *deg* incidence angle for both the *equal individual beam-set polarizations* and *equal sample-plane-set polarizations* cases and gradually reduces to lower contrast values, falling below $V_{abs} = 0.4$ near $\theta \approx 48\,deg$ and $54\,deg$ for the two cases, respectively. When negative (or inverted) intensity distributions (labeled "negative pattern") are considered, higher absolute contrasts may be achieved for the larger incidence angles as depicted in Fig. 4.4(d). When combined with *equal-individual-beam amplitudes*, the *p6m* symmetry is no longer possible (with $V_{13} = V_{23} = V_{12}$). Similar results are obtained for the *cmm*(sq) symmetry as depicted in Figs. 4.4(e) and (f). However, when the *equal-individual-beam amplitudes* is combined with *equal individual beam-set polarizations*, the *cmm*(sq) symmetry remains possible at a single incidence angle of $60\,deg$ with unity absolute contrast.

4.3 Summary

A systematic and comprehensive analysis of the effects of constraints on individual-beam amplitudes and polarizations has been presented for the unique 2D plane-group

symmetries possible using three linearly-polarized beams configured to produce an interference pattern with square- or hexagonal-lattice translational symmetry. These patterns were optimized for maximum uniform contrast while satisfying the conditions for primitive-lattice-vector-direction equal contrasts.

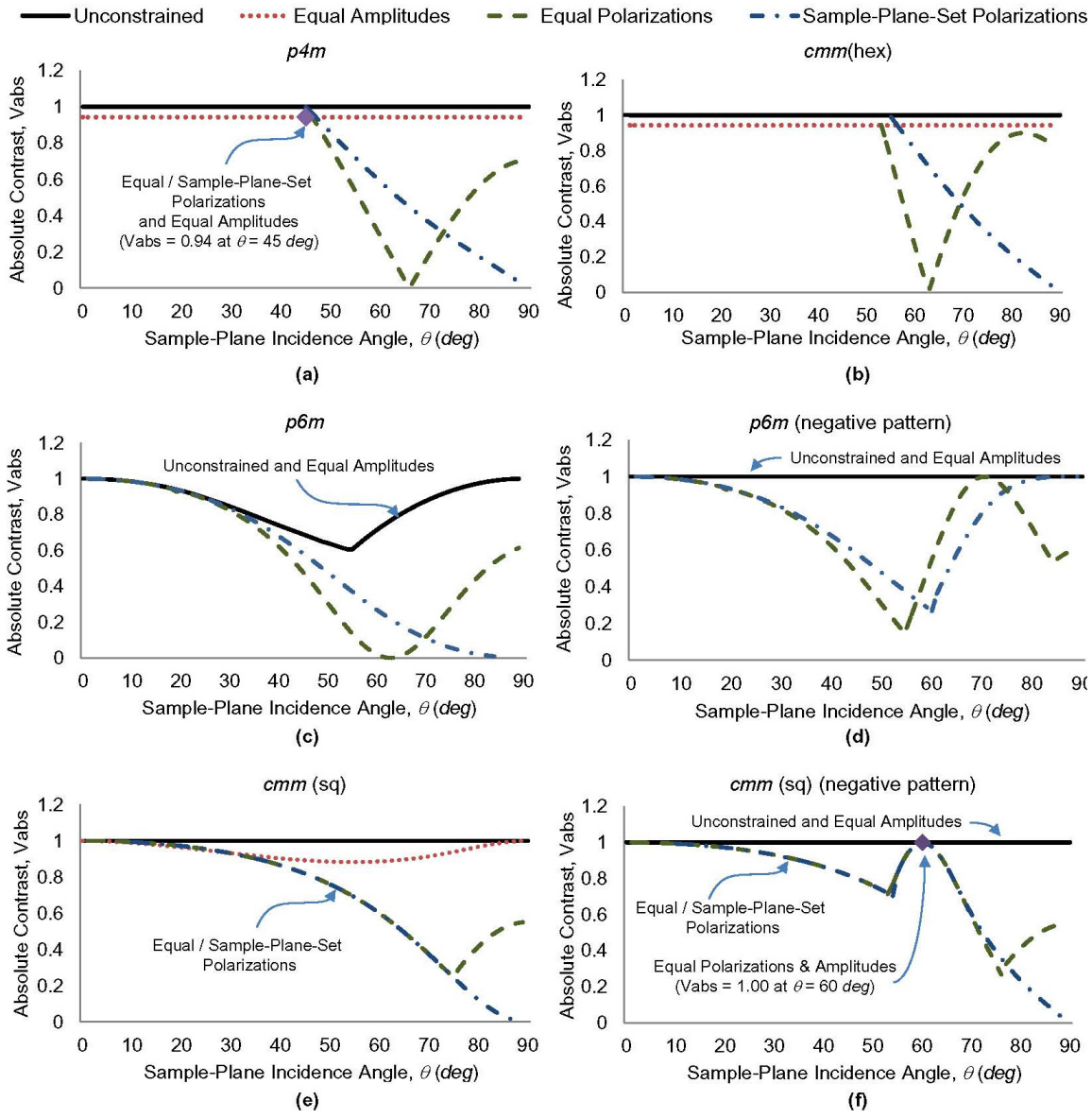

Figure 4.4: Optimized absolute contrasts for square and hexagonal lattices. The unconstrained maximum absolute contrast is compared to the those for the amplitude and polarization constraints as a function of the common wavevector incidence angle at the sample plane for (a) *p4m*, (b) *cmm*(hex), (c) *p6m*, (d) *p6m* (negative pattern), (e) *cmm*(sq), and (f) *cmm*(sq) (negative pattern) plane-group symmetries.

When only amplitude constraints are considered, the results demonstrate that all plane-group symmetries remain possible over the full range of lattice constants. While the absolute contrast is reduced to a minimum value of $V_{abs} = 0.88$, this value is still sufficient for optical lithography purposes.

When polarization constraints are introduced, significant reductions were noted for all plane-group symmetries. Based on the specific application requirements, it may be necessary to use an MBI configuration, such as the multiple-beam-splitting configuration in Fig. 4.2(c), that allows individual conditioning of beam polarizations to ensure a robust patterning capability.

Although numerous additional parametric constraint combinations are possible and may merit consideration, the cases presented here provide useful insight into the general design requirements for an MBI system. However, the optimization methodology presented here may be straightforwardly modified as necessary to model and predict the patterning possibilities of other constrained configurations to ensure that the a given MBI configuration meets the requirements for a specific patterning application.

As efforts to incorporate MBI into commercial fabrication processes continue, a complete understanding of the patterning possibilities is required in the systematic design of future MBI configurations. While the beam-splitting configuration in Fig. 4.2(c) allows for the widest range of high-contrast periodic pattern symmetries, future research will focus on increasing interferometric stability, to provide the potential for relatively simple, subwavelength, and cost-effective periodic patterning with integrated non-periodic functional elements.

CHAPTER 5

PATTERN-INTEGRATED INTERFERENCE LITHOGRAPHY

The results of the constrained parametric optimization study in the preceding chapter are relevant to the design of any optical system that employs multi-beam interference (MBI). In the research presented in this chapter a new methodology that incorporates MBI, Pattern-Integrated Interference Lithography (PIIL), is introduced. To ensure the full-range of optimized interference patterns, an amplitude-splitting configuration with individual beam conditioning capability developed previously by our group [69] as depicted in Fig. 1.7(b) was used to generate the multiple beams required for the system presented in this chapter.

As documented in Chapter 2, interference lithography (IL) has been used in a wide variety of applications. Each of these areas typically requires additional lithographic steps to modify an MBI-defined periodic interference pattern to create integrated functional elements. A new lithographic method is needed to integrate a non-periodic functional element pattern within an MBI-defined periodic lattice in a single-exposure step, thereby reducing the complexity, fabrication time, and associated costs, making this combination a potential option for large-volume commercial fabrication. In this chapter, PIIL is presented to address this need. PIIL is the integration of superposed pattern imaging with IL. The result is a complex optical-intensity distribution composed of an MBI-defined periodic lattice modified by an integrated mask pattern image to form

functional elements. To implement PIIL, a Pattern-Integrated Interference Exposure System (PIIES) is presented that incorporates a projection imaging capability in a novel three-beam interference configuration in order to fabricate, in a single-exposure step, a two-dimensional periodic photonic-crystal (PC) lattice with non-periodic functional elements integrated into the periodic pattern. The *ad hoc* design of the basic system is presented along with a model that simulates the resulting optical-intensity distribution at the system sample plane where the three beams simultaneously interfere and form a superposed integrated image of the projected mask pattern. Appropriate performance metrics are defined in order to quantify the characteristics of the resulting PC structure. These intensity and lattice-vector metrics differ markedly from the metrics used to evaluate traditional photolithographic imaging systems. This research has resulted in four journal papers [69,71,75,76], one conference paper [72], and two patent applications [73,74].

5.1 Pattern-Integrated Interference Exposure System

A conceptual three-beam PIIES configuration is depicted in Fig. 5.1 [73,74]. To demonstrate the functionality of the system, the PIIES configuration presented here is arranged to produce a square-lattice interference pattern depicted in Fig. 5.1(b) by implementing the wavevector configuration depicted in Fig. 5.1(a). The basic PIIIES configuration in Fig. 5.1(c) includes a ray trace of $\mathbf{k}_1$ and $\mathbf{k}_2$ ($\mathbf{k}_3$ is not shown for clarity but is parallel to $\mathbf{k}_1$ and $\mathbf{k}_2$ and lies out of the plane of the page). Initially, the multiple beams propagate parallel to the optical axis of the system at a common beam displacement, d_{beam}. To achieve the desired interference patterning capability the multiple optical components are positioned such that each interfering beam is collimated

at the exit of the final objective lens, intersecting at the sample plane at a specific common incidence angle, θ_S. The result is a uniform-periodic interference pattern with a lattice constant defined by θ_S as given by Eq. (3.5).

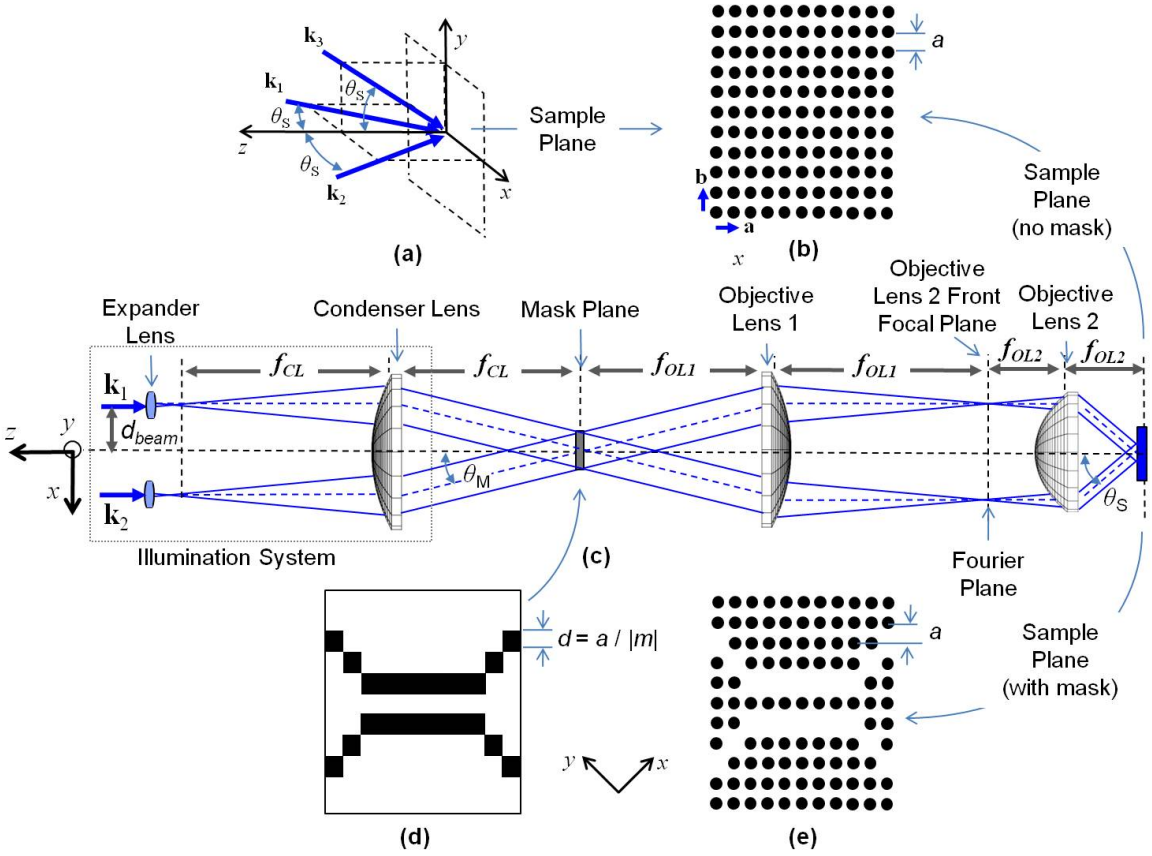

Figure 5.1: Three-beam pattern-integrated interference exposure system (PIIES) **[73]**. (a) The configuration of wavevectors $\mathbf{k}_1$, $\mathbf{k}_2$, and $\mathbf{k}_3$, produce (b) a square-lattice interference pattern. (c) A ray trace depicts the propagation of $\mathbf{k}_1$ and $\mathbf{k}_2$ through the PIIES optical configuration ($\mathbf{k}_3$ is not shown for clarity but is parallel to $\mathbf{k}_1$ and $\mathbf{k}_2$ and lies out of the plane of the page). The interfering beams are collimated and intersect at the sample plane forming a uniform square-lattice pattern. (d) A functional-element amplitude mask is placed at the mask plane with features sizes of $d = a/|m|$, where m is the magnification due to the compound objective lens. (e) The result is an optical-intensity distribution of an integrated non-periodic functional element in an all-surrounding, high-spatial-frequency periodic square lattice, enabling single-exposure fabrication of a functional device, such as a PC waveguide coupler [303].

While the multiple beams, expander lenses, and condenser lens are specifically positioned to produce collimated interfering beams at the sample plane, these same

components also serve as the illumination system for the integrated image projection capability as depicted in Fig. 5.1(c). In the present configuration, the PIIES mask plane is collocated at the condenser lens back focal plane (and the first objective lens front focal plane) where the three expanded beams intersect, providing coherent multi-beam off-axis illumination of an object such as the amplitude mask depicted in Fig. 5.1(d). The purpose of this mask is two-fold. First, the transparent areas of the mask allow the multiple beams to pass through and form the desired interference pattern at the sample plane. Second, the opaque areas of the mask block and diffract the illuminating beams, portions of which are collected by the objective lens and focused at the sample plane. These projected mask elements effectively block the multiple interfering beams at the sample plane, thereby preventing or altering the formation of portions of the interference pattern at areas corresponding to the functional elements defined by the mask features with dimensions, $d = a/|m|$, where m is the magnification due to the compound objective lens. The result is an optical-intensity distribution containing integrated non-periodic functional elements in an all-surrounding, high-spatial-frequency MBI-defined periodic pattern. This distribution may, in turn, be recorded in a photoresist, in a single-exposure step, to form functional devices, such as the PC waveguide coupler depicted in Fig. 5.1(e) [303].

The illumination system presented here differs from the traditional Köhler illumination in three subtle but important ways. First, the PIIES illumination system is positioned so that the mask plane is located at the condenser-lens back focal plane. With traditional Köhler illumination, the mask is typically placed closer to the condenser lens [304]. Second, the multiple illuminating beams are derived from point sources located at

the back focal plane of the expander lenses, resulting in approximately coherent off-axis illumination of the mask by each beam. In a Köhler illumination scheme, the diameter of the source is varied to obtain corresponding degrees of partial coherence, where the source may be thought of as a collection of point sources emanating from within the diameter of the source. Finally, the PIIES illumination system is adjusted such that the multiple beams are focused at the objective lens front focal plane to achieve collimated beams at the sample plane. With Köhler illumination, the source is focused at the objective lens entrance pupil [304]. For a single on-axis source, the Köhler illumination produces a partially coherent beam at the sample plane for each point within the diameter of the source. This results in numerous interference fringes for each beam-pair, differing in periodicity, orientation, and translational position. These interference fringes superpose and average to an approximately uniform intensity distribution. In fact, this is a desired result in traditional Köhler illumination. These subtle differences incorporated into the illumination scheme enable the PIIES to form an optical-intensity distribution that is the superposition of an integrated non-periodic functional element pattern (formed by the projected pattern-mask image) in a periodic lattice (formed by the multiple interfering beams).

5.1.1 System Design

The *ad hoc* design of the PIIES configuration begins with design of a novel lens-based system to implement three-beam interference. To ensure an interference pattern with uniform periodicity and sufficient area, the interfering beams should be collimated as depicted by the ray trace of $\mathbf{k}_2$ and $\mathbf{k}_3$ ($\mathbf{k}_1$ is not shown for clarity) in Fig. 5.2. Here it is seen that collimated beams are produced when the individual beams are focused at the

front focal plane of the objective lens. With collimated beams, the periodicity of the pattern is inversely proportional to the sine of θ_S, as given by Eqs. (3.5) and (3.9). A general relationship for θ_S may be given by

$$\theta_S \propto \tan^{-1} \frac{d_{FFP}}{f_{OL}}, \tag{5.1}$$

where d_{FFP} is the radial distance of the focused beam from the optical axis at the front focal plane and f_{OL} is the objective lens focal length. From the relationship in Eq. (5.1), it can be seen that the incidence angle, which determines the periodicity, is directly proportional to the beam displacement and inversely proportional to the objective lens focal length. This relationship suggests that an objective lens system with a large numerical aperture is desired for the PIIES configuration.

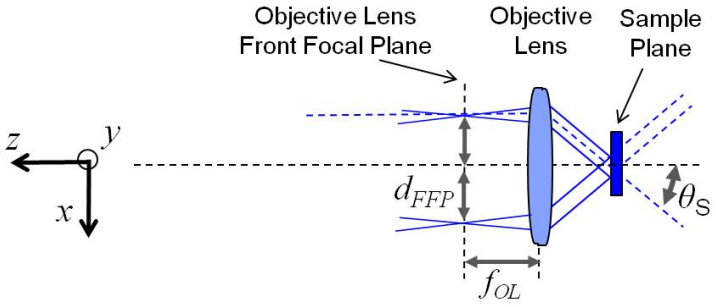

Figure 5.2: PIIES interfering beam collimation. The multiple beams are focused at the objective lens front focal plane to generate collimated beams. This ensures a large-area interference pattern with uniform periodicity at the sample plane. The angle of incidence at the sample plane θ_S is directly proportional to the beam displacement, d_{FFP}, and inversely proportional to the objective lens focal length, f_{OL}.

To obtain a large numerical aperture, thereby increasing the range of possible lattice constants and improving the projected image resolution, a two-lens configuration was selected as depicted in Fig. 5.3. This allows the power of the objective lens system to be divided between two lenses, thereby increasing the maximum possible incidence angle,

θ_S, while reducing lens aberrations for the integrated projection imaging system. Of course, modern projection objective lens designs often include numerous low-power lens elements to minimize several common aberrations including spherical, coma, astigmatism, field curvature, and distortion [305]. In the rudimentary design presented here, only on-axis aberrations were considered. Accordingly, aspheric lens were selected for the two objective lenses to reduce on-axis spherical aberration. Similarly, an aspheric lens was also selected for the condenser lens to minimize distortions to the collimated interfering beams.

Aspheric lenses are designed specifically to provide a common focal point for axial rays, regardless of their radial position, thereby reducing off-axis aberrations. To take advantage of this fact, the compound objective lens design included the requirement that the beams propagate parallel to the optical axis upon exiting the first objective lens and the entrance to the second objective lens as depicted in Fig. 5.3. Similarly, the design required that the beams incident on the condenser lens also be parallel to the optical axis. To satisfy these two conditions, the condenser lens and first objective lens are separated by the sum of the focal lengths, f_{CL} and f_{OL1}, of the two lenses as depicted in Fig. 5.3. As a result, Eq. (5.1) may be restated as

$$\theta_S \propto \tan^{-1} \frac{d_{beam}}{f_{OL2}}, \tag{5.2}$$

where d_{beam} is the radial distance of the individual beams from the optical axis incident on the condenser lens, and f_{OL2} is the focal length of the second objective lens.

To complete the basic PIIES design and integrate an image projection capability, the multiple beams must be conditioned such that they focus at the front focal plane of the second objective lens, while simultaneously illuminating a pattern mask located at the

front focal plane of the first objective lens as depicted in Fig. 5.4. This is accomplished through the selection and placement of one or more expander lenses prior to the condenser lens. It should be noted that more complex systematic optical system designs may be considered to produce collimated interfering beams while improving the system projection imaging capability. However, in the work presented here, a 6*f* configuration is chosen to satisfy the collimating requirements and provide a relatively simple low-cost prototype to demonstrate the PIIL method.

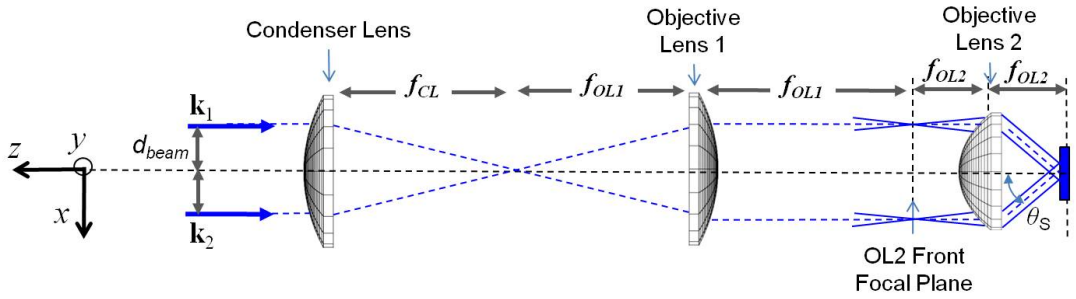

Figure 5.3: Basic PIIES lens configuration. Two axial beams at a radial distance, d_{beam}, from the optical axis are incident on an aspheric condenser lens. The first aspheric objective lens is placed at a distance from the condenser lens such that the beams again propagate parallel to the optical axis. The beams are then focused at the sample plane by the second aspheric objective lens.

The resulting relationship between the diameter of the collimated beam, D, which determines the area of interference, and the beam divergence, δ_{DIV}, at the condenser lens is given by

$$D \propto \delta_{DIV} \propto \frac{1}{f_{EL}}, \tag{5.3}$$

where f_{EL} is the effective focal length of the expander lens system. The relationships given by Eqs. (5.2) and (5.3) both suggest that a large diameter lens is preferred for both the condenser lens and the first objective lens. However, the focal length of these two lenses may be longer to reduce the power, and therefore the aberrations of the PIIES

configuration. Accordingly, appropriate commercially available large-diameter broadband antireflection coated aspheric lenses were used for the condenser and first objective lenses (ThorLabs, AL100200-B). To increase the numerical aperture of the compound objective lens system, a higher power lens with smaller focal length was selected for second objective lens (ThorLabs, AL7560-A).

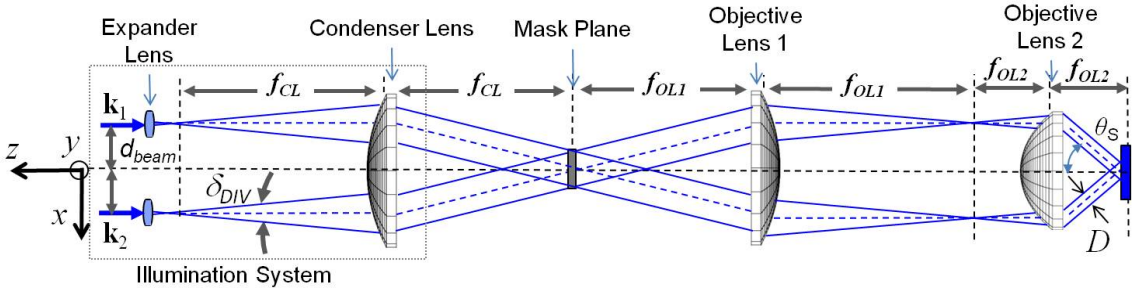

Figure 5.4: PIIES configuration. Expander lenses are added to ensure that the multiple beams are focused at the back focal plane of the compound objective lens, while providing coherent illumination of a pattern mask located at the mask plane.

The resulting prototype PIIES configuration of Fig. 5.4 allows for a wide range of lattice constants and translational symmetries that vary from square to hexagonal, as determined by the radial displacement and arrangement of the three beams with respect to the optical axis. Based on the relationship given by Eq. (5.2) and the equations for the square and hexagonal lattice constants given by Eqs. (3.5) and (3.9) respectively, the lattice constant may be increased or decreased by adjusting the radial distance of the individual beams from the optical axis.

5.1.2 Zemax System Optimization

To determine the positioning and alignment requirements for the various optical elements within the PIIES configuration, a ray-tracing simulation was performed using Zemax optical design software to model the beam propagation through the system [306]. Figure

5.5 depicts the Zemax-simulated ray trace for a single beam through the PIIES configuration.

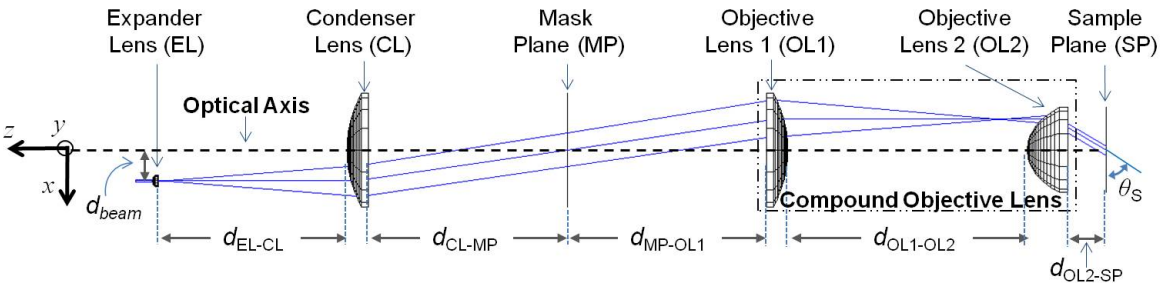

Figure 5.5: Zemax ray tracing of one beam through the PIIES configuration.

Using the lens specifications obtained from Thorlabs datasheets and the Zemax optimization algorithm described in Appendix A, the beam displacement, d_{beam}, and the inter-lens distances, $d_{\text{EL-CL}}$, $d_{\text{CL-MP}}$, $d_{\text{MP-OL1}}$, $d_{\text{OL1-OL2}}$, and $d_{\text{OL2-SP}}$, were set as variable parameters to optimize jointly the following:

1) Collimation of the beam at the mask plane,

2) Centering of the beam on the origin at the mask plane,

3) Axial beam propagation between first and second objective lenses,

4) Collimation of the beam at the sample plane,

5) Centering of the beam on the origin at the sample plane, and

6) Setting the specified value of θ_S at the sample plane.

Physical constraints of the opto-mechanical system presented here limited beam displacement to a minimum value of approximately $5\,mm$ from the optical axis. This value results in an approximate minimum incidence angle of $\theta_S \approx 5\,deg$. For θ_S larger than $30\,deg$, the beam becomes vignette due to clear aperture limitations of the second objective lens as depicted in Fig. 5.6. This limitation requires the beam diameter to be

reduced for larger incidence angles corresponding to the beam displacement from the optical axis. This, in turn, reduces the beam diameter at the sample plane, D_{beam}, resulting in a reduced area of interference. In the simulations presented here, the incidence angle at the sample plane ranges from $5 \leq \theta_S \leq 30\,deg$.

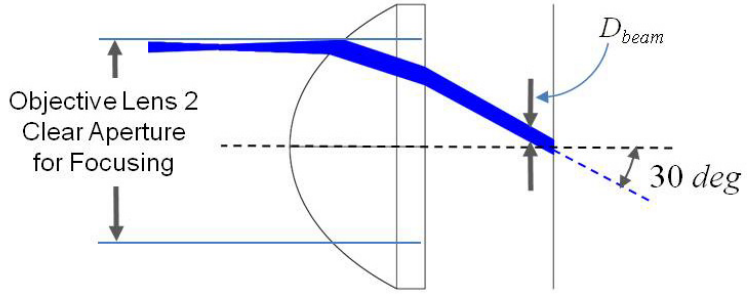

Figure 5.6: Clear aperture limitations. A relatively large beam diameter D_{beam}, corresponding to a large area of interference, is possible for incidence angles up to approximately $30\,deg$. At this point, clear aperture limitations begin to vignette the beam incident on the second objective lens.

Experimentally feasible values of d_{beam} and inter-lens distances were found that satisfy the above constraints. Of note, $d_{EL\text{-}CL}$, $d_{\text{OL1-OL2}}$, and the PIIES total length d_{total}, measured from the expander lens to the sample plane, were found to vary with θ_S. Figure 5.7 illustrates the change in axial length of $\Delta d_{\text{EL-CL}}$, $\Delta d_{\text{OL1-OL2}}$, and Δd_{total} as a function of θ_S. Here d_{total} decreases from $813.23\,mm$ to $761.61\,mm$ for θ_S ranging from 5 to $30\,deg$, resulting in a PIIES total length difference Δd_{total} of $-51.61\,mm$ for $\theta_S = 30\,deg$.

These results suggest that the condenser lens, mask mount, and first objective lens may be fixed relative to one another, while the beam displacing optics, expander lenses, second objective lens, and sample mount require adjustment for each desired lattice constant and translational symmetry. Accordingly, appropriate translation stages are required to mount the optics and adjust the lens positions as θ_S is changed. Comprehensive alignment procedures are presented in Chapter 6.

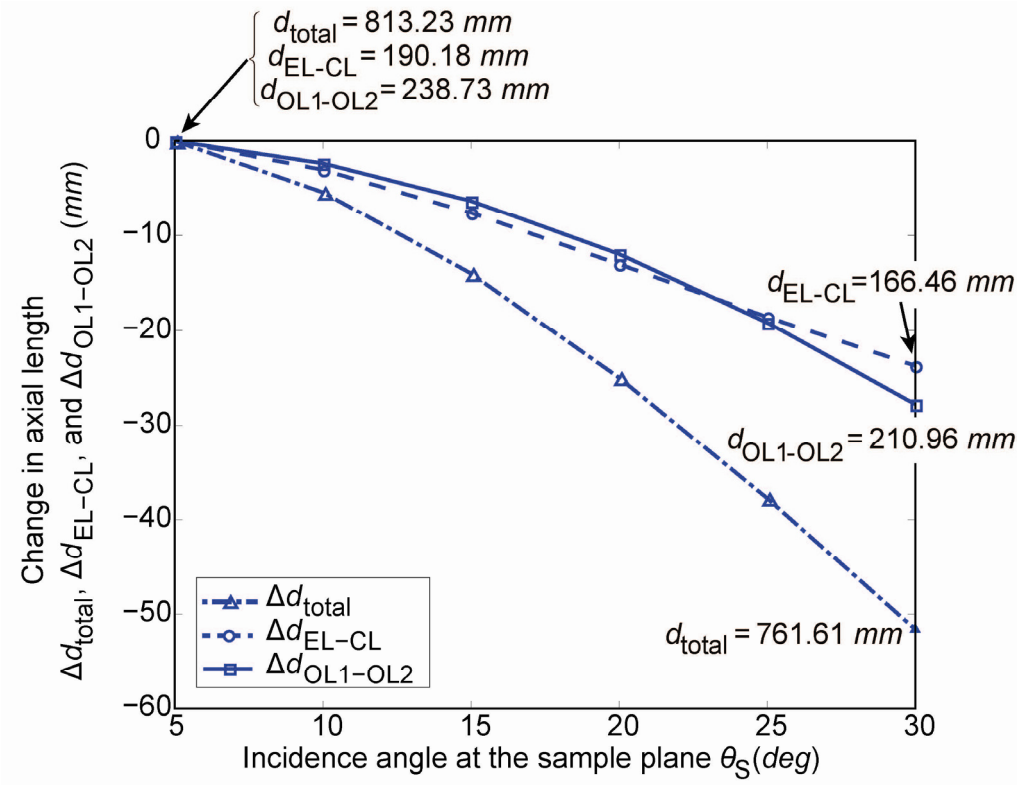

Figure 5.7: PIIES inter-lens distances. The key inter-lens distances between the lens surfaces as depicted in Fig. 5.5, $\Delta d_{EL\text{-}CL}$, $\Delta d_{OL1\text{-}OL2}$, and Δd_{total}, are plotted as a function of the incidence angle, θ_S, at the sample plane.

5.1.3 Predicted System Performance

Using the Zemax optimization routine described in the previous section, the simulated PIIES performance was analyzed for the full range of beam incidence angles for both the square and hexagonal wavevector configurations depicted in Fig. 3.1. For θ_S varying from 5 to 30 *deg*, the lattice constant for square-lattice translation symmetry measured at the origin of the sample plane, a_{sq0}, ranges from 2.952 to 0.514 μm. For hexagonal-lattice translation symmetry, the lattice constant measured at the origin of the sample plane, a_{hex0}, ranges from 2.78 to 0.485 μm. However, the beam is slightly divergent at the sample plane, resulting in a small range of incidence angles for the rays. Thus, the beam

produces a range of lattice constants, Δa_{sq} and Δa_{hex}, for both translational symmetries, ranging from 3.1% to 1.5%. In addition, the initial circular cross-section of the beam is inevitably modified during its propagation through the PIIES and its projection on the sample plane decreases as θ_S increases as well. Thus, the circular overlap area of the three beams A_{SP} ranges from 60.82 to $19.63 mm^2$, with an important drop of the overlap area as the incidence angle approaches $\theta_S = 30 deg$, where the beam starts to become vignetted by the second objective lens clear aperture. The resulting simulated d_{beam}, a_{sq0}, Δa_{sq}, a_{hex0}, Δa_{hex}, and A_{SP} values are presented in Table 5.1.

Table 5.1: Zemax simulated PIIES interference pattern performance.

θ_S (deg)	d_{beam} (mm)	Lattice Constants				A_{SP} (mm^2)
		a_{sq0} (μm)	Δa_{sq} (%)	a_{hex0} (μm)	Δa_{hex} (%)	
5	4.95	2.952	3.1	2.783	3.1	60.82
10	9.82	1.481	2.9	1.397	2.9	55.42
15	14.53	0.994	2.7	0.937	2.7	50.27
20	19.02	0.752	2.3	0.709	2.3	45.36
25	23.25	0.609	1.9	0.574	1.9	40.72
30	27.19	0.514	1.5	0.485	1.5	19.63

The resulting interference pattern simulated in Zemax is depicted in Fig. 5.8(a). For comparison, the equivalent Matlab-simulated square-lattice interference pattern is depicted in Fig. 5.8(b). Here, the pattern is optimized for *cmm* plane-group symmetry ($|\mathbf{a}| = |\mathbf{b}|$, $V_{12}=V_{13}=V_{23}$), where each beam-pair produces interference fringes with equal contrast. This result confirms that Zemax does not take into account polarization in the formation of an interference pattern, modeling the interference of any two beams with a common contrast. For this reason, the Zemax interference-pattern simulation cannot predict accurately the plane-group symmetries or precise motif geometries for individual beam-set polarizations and amplitudes. However, Zemax may

be used to verify the desired translational symmetry and periodicity of the resulting interference pattern.

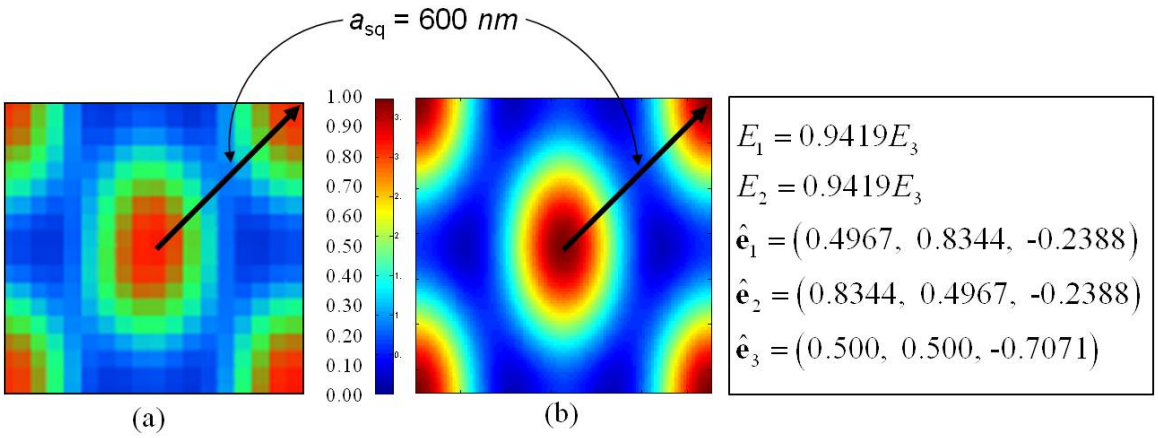

Figure 5.8: Simulated interference pattern. (a) The Zemax simulation produces a square-lattice interference pattern with a $600\,nm$ lattice constant for an incidence angle of $\theta = 25.39\,\text{deg}$. (b) The same pattern is simulated with Matlab, optimized for the *cmm* plane-group symmetry where each interference coefficient is equal in magnitude.

The Zemax simulations confirm that the PIIES design is capable of generating incident angles at the sample plane ranging from $5 < \theta_S < 30\,deg$. Furthermore, the PIIES is capable of producing photonic crystal structures varying between square and hexagonal translational symmetry, exhibiting sub-micron periodicity with good uniformity over a surface area of at least 40 mm^2.

While the basic PIIES MBI patterning may be verified in Zemax as presented here, the system also includes an integrated imaging system and should be modeled as well. The version of Zemax used in the current research provides coherent image predictions by conducting a Fourier analysis of the complex system optical transfer function, accounting for the finite pass band and other diffraction-related effects of the real optical system [306]. This method assumes a single extended coherent illumination source and approximates the coherent transfer function to form the predicted image. However,

Zemax does not provide a means to model multi-beam off-axis mask illumination. Due to the unique design of the PIIES, Zemax, as well as other commercial image simulation software, are not able to simulate simultaneously the MBI-defined interference pattern with integrated functional elements resulting from the projected mask image.

A new model is required to analyze the quality of the pattern-integrated optical-intensity distribution of the PIIES presented here.

5.2 System Model

The time-average optical-intensity distribution given by Eq. (3.1) may be modified to

$$I_T(\mathbf{r}) = I_0(\mathbf{r})\left\{1 + V_{12}(\mathbf{r})\cos\left[(\mathbf{k}_2 - \mathbf{k}_1)\cdot\mathbf{r}\right] + V_{13}(\mathbf{r})\cos\left[(\mathbf{k}_3 - \mathbf{k}_1)\cdot\mathbf{r}\right] + V_{23}(\mathbf{r})\cos\left[(\mathbf{k}_3 - \mathbf{k}_2)\cdot\mathbf{r}\right]\right\}, \tag{5.4}$$

where the intensity term, $I_0(\mathbf{r})$, and interference coefficients, $V_{ij}(\mathbf{r})$, are defined as

$$I_0(\mathbf{r}) = \sum_{i=1}^{3} 1/2E_i(\mathbf{r})^2 \quad \text{and} \quad V_{ij}(\mathbf{r}) = \frac{E_i(\mathbf{r})E_j(\mathbf{r})(\hat{\mathbf{e}}_i \cdot \hat{\mathbf{e}}_j)}{I_0(\mathbf{r})}, \tag{5.5}$$

and $E_i(\mathbf{r})$ is the complex electric-field amplitude of the i^{th} beam [56].

If no mask is present in the PIIES configuration of Fig. 5.1(c), the constant intensity term and interference coefficients become simple scalar values, I_0 and V_{ij}, and Eq. (5.4) simplifies to the familiar equation for the interference pattern formed by three linearly-polarized, monochromatic plane waves given by Eq. (3.1). However, when a mask is placed at the mask plane, the constant intensity term and interference coefficients become complex as defined by Eq. (5.5). To understand the effects of integrating a pattern mask, the PIIES compound objective lens of Fig. 5.1(c) is arranged as a 4*f* optical system that

can be modeled using Fourier optics. In this configuration, the complex electric field for the i^{th} beam at the sample plane can be expressed as

$$E_i(x,y) = \mathcal{F}^{-1}\left[M_i(f_x,f_y)P(f_x,f_y)\right], \tag{5.6}$$

where $\mathcal{F}^{-1}$ is the inverse Fourier transform, f_x and f_y are the spatial frequencies, $M_i(f_x,f_y)$ is the electric field at the Fourier plane, and $P(f_x,f_y)$ is the objective-lens pupil function [307].

5.2.1 Mask Function

For a thin binary or grayscale complex amplitude mask, illuminated by a single coherent on-axis beam, the electric field at the Fourier plane is given by

$$M(f_x,f_y) = \iint t(x,y)\exp\left[-i2\pi(f_x x+f_y y)\right]dxdy = \mathcal{F}[t(x,y)], \tag{5.7}$$

where $t(x,y)$ is the amplitude transmittance of the mask and $\mathcal{F}$ is the Fourier transform [307]. For on-axis mask illumination, the amplitude pattern at the Fourier plane is centered at the origin. However, in the PIIES configuration, three off-axis beams illuminate the mask at a common incidence angle, θ_M, as illustrated in Fig. 5.1(c). As a result, the amplitude patterns associated with each beam are shifted in spatial frequency from the origin by an amount

$$(f'_{x,i},\, f'_{y,i}) = \left(\frac{\sin\theta_M\cos\varphi_i}{\lambda}, \frac{\sin\theta_M\sin\varphi_i}{\lambda}\right), \tag{5.8}$$

where φ_i is the azimuthal angle of the i^{th} beam [307]. As a consequence, each off-axis beam creates a unique complex electric field at the Fourier plane, $M_i(f_x - f'_{x,i}, f_y - f'_{y,i})$, that results in unique complex electric fields, $E_i(x,y)$, for each

beam at the sample plane as defined by Eq. (5.6). The electric field amplitude, $E_i(\mathbf{r})$, for each beam is then the magnitude of the complex electric field.

5.2.2 Pupil Function

For an aberration-corrected lens, the ideal pupil function describes the light collected and transmitted by the objective lens and is defined as

$$P(f_x, f_y) = \begin{cases} 1, \text{ if } \sqrt{f_x^{\,2} + f_y^{\,2}} < \dfrac{CA_2/2}{\lambda f_2} \\ 0, \text{ if } \sqrt{f_x^{\,2} + f_y^{\,2}} > \dfrac{CA_2/2}{\lambda f_2} \end{cases}, \tag{5.9}$$

where CA_2 is the clear aperture and f_2 is the focal length of the second objective lens [308].

When the magnification, *m*, of the optical system is considered, the angles of incidence in the mask plane and in the sample plane are not the same for every spatial frequency. Consistent with energy conservation, an obliquity factor must be included in the pupil function. In the spatial frequency domain, the obliquity factor can be expressed as [304]

$$O(f_x, f_y) = \left[\frac{1 - m^2\lambda^2\left(f_x^2 + f_y^2\right)}{1 - \lambda^2\left(f_x^2 + f_y^2\right)} \right]^{\frac{1}{4}}. \tag{5.10}$$

Next, wavefront aberrations in the optical system may be included by using the 37-term Zernike polynomial, W(x,y). The fringe Zernike coefficients for the compound objective lens may be found using Zemax [309] optical system design software. In the spatial-frequency domain, the wavefront aberrations can be expressed as [307]

$$Z\left(f_x, f_y\right) = \exp\left[i \frac{2\pi}{\lambda} W\left(\lambda f_2 f_x, \lambda f_2 f_y\right) \right]. \tag{5.11}$$

The total pupil function of the PIIES is then given by

$$P\left(f_x, f_y\right) = P_{ideal}\left(f_x, f_y\right) O\left(f_x, f_y\right) Z\left(f_x, f_y\right). \tag{5.12}$$

Together, the mask and pupil functions provide a full scalar model using Eq. (5.6). However, the current model does not include full polarization considerations as it has been demonstrated that the nonparaxial scalar model remains applicable for numerical apertures up to approximately 0.6 [310]. With a maximum numerical aperture of 0.62 for objective lens 2, polarization effects are not included here, and individual beam polarizations are assumed to remain linear throughout the optical system. Full polarization considerations should be the subject of future work as larger numerical apertures are considered.

5.2.3 Aerial Optical-Intensity Distribution Simulation

Using Eq. (5.4) and representative optical system parameters described in Appendix B, the aerial optical-intensity distribution at the PIIES sample plane was simulated using Matlab [297] as depicted in Fig. 5.9. Figure 5.9(a) illustrates the interference pattern of three beams with no mask present, matching the predictions of Stay *et al.* for a *p4m* plane-group symmetry [59]. When the functional-element mask of Fig. 5.1(d) is placed at the mask plane and illuminated by a single off-axis beam, the resulting projected aerial intensity distribution at the sample plane is depicted in Fig. 5.9(b). Despite diffraction effects and lens aberrations, the projected functional-element image remains well defined. Figure 5.9(c) shows the complete optical-intensity distribution at the sample plane when the mask is illuminated by all three off-axis interfering beams. Here, the combination of

MBI and the projected functional-element mask pattern produces an overall distribution that very closely resembles the desired pattern for the example PC wavguide coupler depicted in Fig. 5.1(e). A closer inspection of Fig. 5.9(c) reveals some slight amplitude variations and lattice-point distortions near the functional element. Accordingly, a discussion of PIIL perfomance metrics follows.

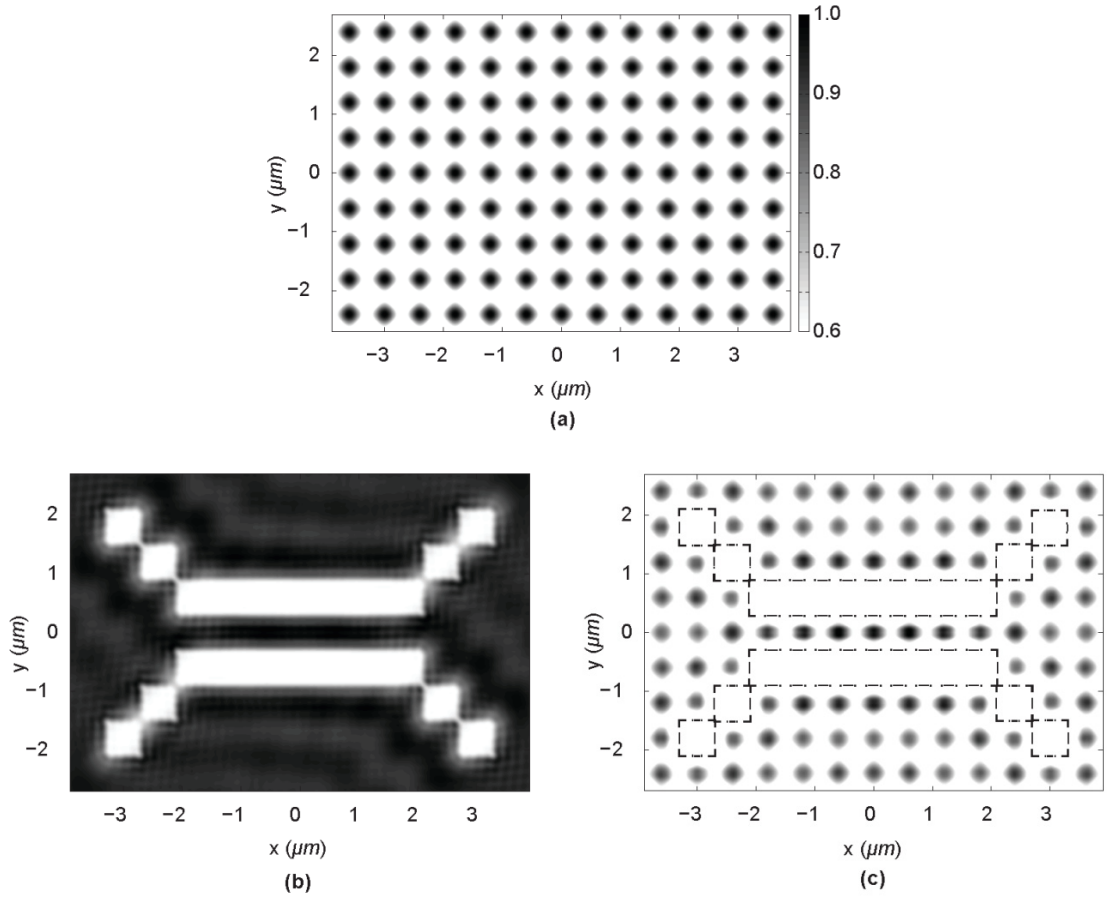

Figure 5.9: Simulated aerial optical-intensity distribution at the PIIES sample plane. (a) With no mask present, the normalized intensity plot depicts a uniform periodic three-beam interference pattern. (b) When a mask is illuminated by a single off-axis beam, the projected aerial intensity distribution at the sample plane is defined by the mask pattern. (c) When the mask is illuminated by all three off-axis interfering beams, the simulated optical-intensity distribution at the sample plane includes interference and projection patterning (outlined by a dashed line), allowing for the single-exposure formation of a PC device.

5.3 Pattern Metrics

In optical lithography for microelectronic and nanoelectronic circuitry, the conventional quality metrics for the resulting pattern include 1) the minimum feature size (often the half pitch of a DRAM cell), 2) distortion (also called tilt) (magnification varying with distance from the axis of the optical system producing placement error as a function of field position), 3) corner rounding, 4) line edge roughness (deviations from a smooth sidewall of a feature in the depth direction), 5) sidewall angle (angle of photoresist sidewall), 6) presence of an "open" at a location where two conductors should be connected (represents a fatal fault), and 7) presence of a "short" where two conductors should be separated (also a fatal fault). These metrics are very appropriate for conventional integrated electronic circuits where the electrical characteristics are of paramount importance.

However, in optical integrated circuits, a waveguide, coupler, resonator, or modulator functions satisfactorily if it meets or exceeds its operational performance specifications. In general, there is a gradual degradation of optical device performance with fabrication errors. An optical waveguide, for example, may transmit light in a completely satisfactory manner even though there are refractive index variations within the waveguiding region due to nonideal photolithography. On the other hand, specific patterns of low-level refractive index changes may produce unacceptably large scattering losses in the waveguide. Figure 5.10 depicts the simulated PIIES optical-intensity distribution for the PC waveguide coupler presented in Fig. 5.9(c) with detailed views of several individual lattice points. The first motif depicted in Fig. 5.10(b), representing an unperturbed lattice point, is obtained when no mask is present or alternatively at locations

in the optical-intensity distribution that are sufficiently removed from functional elements. Figures 5.10(c) and (d) represent motifs in close proximity to the functional element, yet these motifs are still relatively unperturbed. In some cases, the projected functional element has a noticeable effect on some individual motifs immediately adjacent to the functional element as depicted in Figs. 5.10(e)-(g).

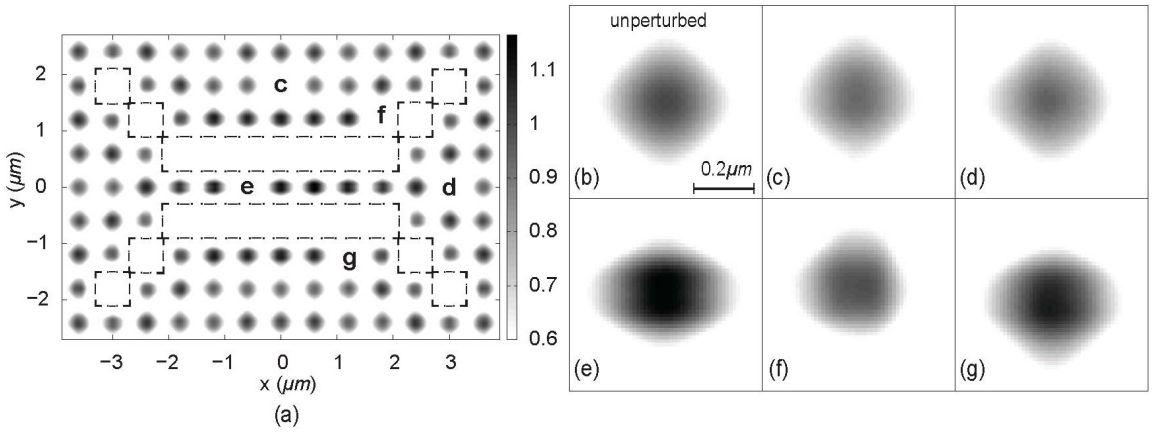

Figure 5.10: Simulated PIIES aerial optical-intensity distribution for a PC waveguide coupler. (a) The normalized intensity depicts a projected functional element (outlined by a dashed line) that prevents the formation of interference lattice points to define a PC waveguide coupler in a single-exposure. (b) An unperturbed PC lattice point in the absence of a pattern mask forms a motif with *p4m* plane group symmetry. (c),(d) Most motifs in close proximity to the functional element remain relatively unperturbed, while (e)-(g) the projected functional element has a noticeable effect on some of the PC motifs immediately surrounding PC device.

While the qualitative observations provided by Fig. 5.10 are instructive, quantitative measures will become important and should be defined to enable specifications and tolerances on the design, fabrication, and performance of functional optical integrated circuits created using PIIL. Photonic-crystal device and circuit development is still a relatively young field. Correspondingly there are a myriad of additional issues to be addressed. At this early stage of progress, it is particularly important to define a relatively complete set of pattern metrics in terms of the aerial optical-intensity distribution being produced. These metrics can then be extended in a straightforward

manner to the subsequent 1) developed photoresist pattern characteristics and then to the 2) fabricated device characteristics. As with the electronic metrics, statistical distributions of these optical pattern metrics would provide an overall description of the quality of a resulting pattern and aid in the design and optimization of lithographically useful PIIL patterning.

5.3.1 Intensity Performance Metrics

The intensity at various positions within the PC device pattern needs to be quantified. To facilitate comparison, the intensity values are normalized to the intensity at a lattice point in the unperturbed periodic lattice (no functional elements present) as depicted in Fig. 5.10(b). In the PIIES, this periodic pattern would be produced with the mask absent (flood exposure or open frame exposure) so that only the periodic pattern exists (no functional elements). Even though in practice the mask can be a binary or gray-scale amplitude and/or phase mask, for simplicity it will be taken here to be a binary amplitude mask for the purpose of defining the intensity metrics below.

Mask-Unaltered-Lattice-Unit-Cell-Intensity Metrics, In1-4: These metrics give the normalized intensities at locations within the unit cells where (based on the mask pattern) the periodic PC pattern should be unaltered.

Mask-Altered-Lattice-Unit-Cell-Intensity Metrics, In5-8: These metrics give the normalized intensities at locations within the unit cells where (based on the mask pattern) the intensity should be zero, corresponding to functional elements.

The eight intensity metrics, In1-8, are defined in Table 5.2. From these metrics, a wide range of contrast ratios can therefore be defined as needed.

5.3.2 Lattice-Vector Performance Metrics

Lattice-vector performance metrics provide information about variations in the fundamental lattice vectors, which may become "distorted" due to a nearby functional element.

Mask-Unaltered-Lattice-Vector Metrics, LV1-8: These metrics give the normalized lengths and angular deviations of the fundamental lattice vectors in the principal axis directions, **a** and **b**, as depicted in Fig. 5.1(b). The metrics are referenced to the lengths and angles of the fundamental lattice vectors in the unperturbed (no functional elements) PC lattice. The eight lattice-vector metrics, LV1-8, are defined in Table 5.2.

Table 5.2: Intensity and lattice-vector metrics for unaltered PC lattice points and altered (zero amplitude) functional element locations.

Metric	Metric Description		
	Pattern Element	Location within Unit Cell	Normalized Intensity
In1	Photonic Crystal	Center	Highest
In2			Lowest
In3		Any location	Highest
In4			Lowest
In5	Functional Element	Center	Highest
In6			Lowest
In7		Any location	Highest
In8			Lowest
		Lattice-Vector Direction	Normalized Length
LV1	Photonic Crystal	**a**	Longest
LV2			Shortest
LV3		**b**	Longest
LV4			Shortest
			Angular Deviation
LV5	Photonic Crystal	**a**	Max CCW
LV6			Max CW
LV7		**b**	Max CCW
LV8			Max CW

For the example PC waveguide coupler, the simulated maximum and minimum pattern metric locations and values are depicted in Fig. 5.11. The values for metrics In1-

In4 reveal that the PC lattice point intensities remain very close to the desired unperturbed values with maximum perturbations of 20% or less for this case. One notable deviation is In7 at a value of 0.20 representing an unwanted, yet significantly attenuated lattice point within the functional element. This value is well below the levels of the surrounding PC lattice points, suggesting that normal lithographic processing techniques would prevent the formation of lattice points within the functional element. For example, the intensity plot of Fig. 5.10 only depicts normalized intensity values above 0.6, well above the In7 value of 0.20.

The lattice-vector metrics given in Fig. 5.11 also show minimal effects of the pattern mask with normalized vector lengths varying by less than 6% and angular deviations of less than 5*deg* at locations near the functional element. To gain a better appreciation for the lattice-vector perturbations across the entire optical-intensity distribution, Fig. 5.12 provides a comprehensive view of the lattice-vector metrics distributed between adjoining PC lattice points with normalized lattice-vector length perturbations (LV1-4) depicted in Fig. 5.12(a) and angular deviations (LV5-8) depicted in Fig. 5.12(b).

Beyond the amplitude and lattice-vector metrics presented here, the shapes and therefore the symmetries of the unit cells in the PC pattern will vary due to deviations from the unperturbed lattice geometry. For example, the unperturbed circular motifs of an original square or hexagonal symmetry lattice will become altered when a functional element mask is introduced as depicted in Figs. 5.10(e)–(g). An ideal square lattice with *p4m* plane group symmetry may locally become *cmm*, *pmm*, *p2*, or *p1* plane group symmetry. An ideal hexagonal lattice with *p6m* plane group symmetry may locally become *cmm*, *p2,* or *p1* plane group symmetry. If the motif becomes elliptical, the

change can be described generally by its ellipticity. If more accurate models of the motif are required, the distorted motif shape may be defined by a modified super-ellipse equation to describe a shape that varies from an ellipse to a more complex rectilinear geometry as described in Chapter 4 of this thesis [77,78]. In some situations, this symmetry information may be useful in describing deviations in the resulting optical-intensity pattern, while providing more accurate models to analyze PC device performance.

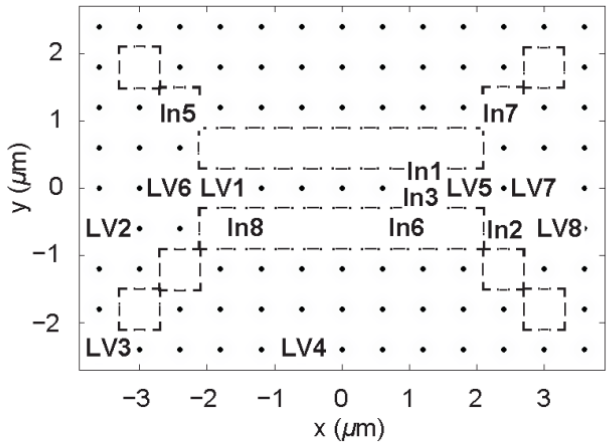

In1=1.16	In2=0.92	In3=1.17	In4=5.03 x 10^{-7}
In5=4.60 x 10^{-3}	In6=9.07 x 10^{-4}	In7=0.20	In8=1.70 x 10^{-5}
LV1=1.06	LV2=0.94	LV3=1.04	LV4=0.94
LV5=3.43°	LV6=-3.43°	LV7=4.67°	LV8=-4.67°

Figure 5.11: Simulated PIIES aerial optical-intensity distribution pattern metrics for a PC waveguide coupler. Single points represent the PC lattice with the projected functional element defined by a dashed line. Maximum and minimum locations for the intensity and lattice-vector metrics are labeled with their corresponding values.

5.4 Summary

In this chapter, the *ad hoc* design, optimization, and modeling of the PIIES, using a novel three-beam interference system with an integrated projection imaging capability, indicate the potential of PIIL for single-exposure fabrication of uniform PC lattices with

integrated functional elements. Zemax optimization and simulation results suggest that wafer-scale uniform periodic patterning is possible. The ability to create this large-area high-spatial-frequency pattern through IL should reduce the diffraction limitations of using traditional projection lithography alone, especially when the desired integrated pattern contains regular underlying grid patterns, such as seen in PC devices.

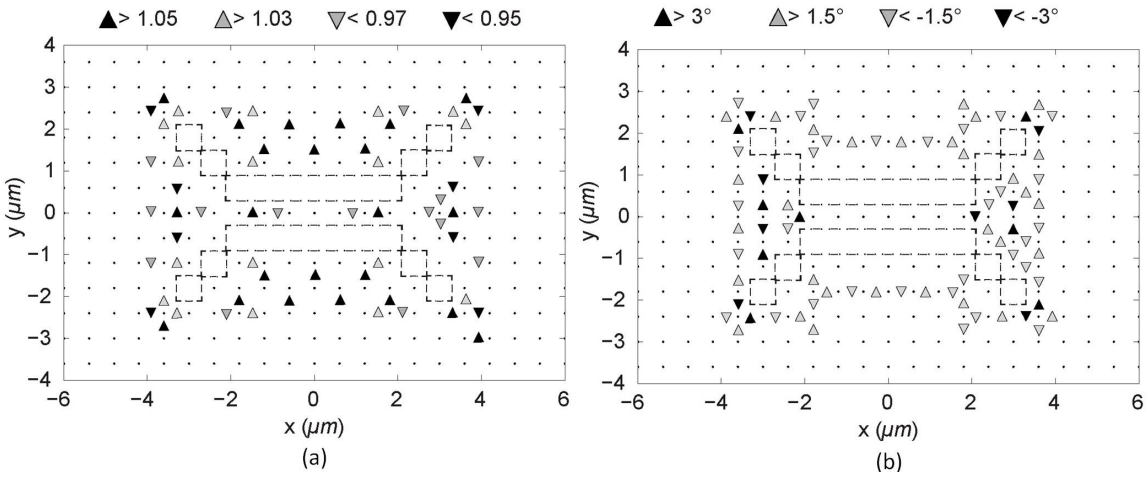

Figure 5.12: Simulated PIIES aerial optical-intensity distribution lattice-vector metrics for an example PC waveguide coupler. (a) The normalized lattice-vector lengths vary by 6% or less with (c) angular deviations of less than 5*deg*.

To understand and predict better the pattern-integrated imaging capabilities of the PIIES configuration presented in this chapter, a new Fourier model was developed by modifying the three-beam plane-wave intensity distribution to include a complex description of each interfering beam that includes the integrated projected mask pattern information. Using this model, new performance metrics were developed to characterize the functional element and surrounding lattice point amplitudes and lattice vectors. Even with relatively low-cost commercially available optics, simulations suggest that the prototype PIIES will produce the desired photonic crystal structures.

CHAPTER 6

FABRICATION OF PHOTONIC-CRYSTAL STRUCTURES

To demonstrate the Pattern-Integrated Interference Lithography (PIIL) method and validate the Pattern-Integrated Interference Exposure System (PIIES), design and modeling in the preceding chapter, a prototype PIIES was constructed in the Optics Laboratory located in Pettit Microelectronics Building 260 as illustrated in Fig. 6.1. Simulation and experimental results presented in this chapter demonstrate the fabrication of well-defined representative photonic-crystal (PC) cavity and waveguide structures in a single-exposure step. This research has resulted in two journal papers [75,76], one conference paper [72], and two patent applications [73,74].

6.1 Experimental Configuration

A Spectra-Physics argon-ion UV laser was used as the PIIES source, operating at a single-line wavelength of $363.8\,nm$ with an output power of $75\,mW$ and a beam diameter of $1.7\,mm$. To ensure a high-contrast interference pattern for a wide range of periodic-lattice symmetries, a combination of half-wave plates and beam-splitter cubes were used to control individual-beam linear polarizations and amplitudes [69,77]. To minimize spherical aberration for on-axis pattern-integrated imaging, three large-diameter commercially available broadband antireflection-coated aspheric lens were used for the condenser and first objective lens (Thorlabs, AL100200-B) and the second objective lens

(Thorlabs, AL7560-A). The condenser lens was mounted on a two-axis (x and z axis) translational stage. The first objective lens was mounted on a one-axis (z axis) translation stage, and the final objective lens was mounted on a three-axis (x and z axis) translational stage. Mounted small diameter aspheric lenses (Thorlabs, A220TM-A) were used for the three expander lenses, each mounted on compact dovetail three-axis linear-translation platforms. A four-inch chrome pattern mask was positioned using a three-axis translating pattern-mask mount. Similarly, a two-axis (x and z) translating sample mount was used to position the sample for exposure. A custom sample holder and multiple lens mount adapters were designed and fabricated, as depicted in Fig. 6.2, to assist with system alignment and experimental fabrication.

As pictured in Fig. 6.1(b), the experimental configuration included an optional pre-exposure real-time monitoring capability [69] to confirm MBI patterning symmetries, facilitate system alignment, and establish initial focusing of integrated pattern-mask features. For real-time mask-image monitoring and initial focusing, a 3.2 Megapixel Olympus Q-Color3 Imaging System digital charge-coupled device (CCD) camera [311] was placed at the sample plane (in place of the sample mount) to capture the pattern-integrated optical-intensity distribution. An example CCD image capture of a Greek cross, used for alignment and focusing, is pictured in Fig 6.3. Camera resolution limitations prevent the formation of a well-focused image. However, the CCD image does allow for initial system focusing prior to experimental fabrication as described later in this chapter.

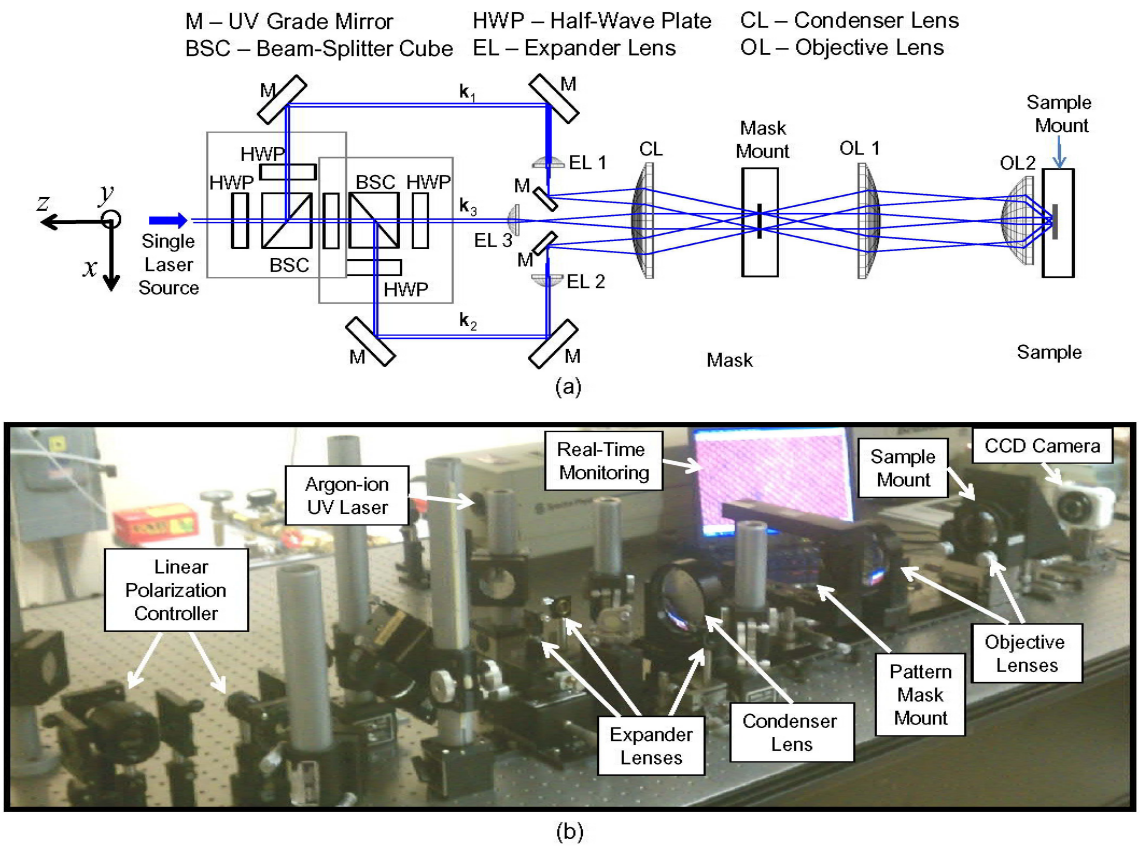

Figure 6.1: Experimental configuration. (a) The basic PIIES optical configuration includes the ability to set individual-beam amplitudes and linear polarizations. (b) Large diameter aspheric lenses are employed for the condenser and objective lenses. Three-axis translational stages allow for precise placement of the mask features and the sample plane to assist in the alignment and focusing of the integrated mask patterns.

For real-time interference pattern monitoring, a 60x Newport microscope objective was placed at the intersection of the three interfering beams such that the beams entered at the front of the lens assembly, serving to enlarge the interference pattern by decreasing the common incidence angle. The CCD camera was then placed at the exit of the objective lens at an approximate tube length of $160mm$ as depicted in Fig. 6.1(b) allowing for real-time monitoring of the interference pattern [69]. For comparison, a Matlab simulation in Fig. 6.4(a) depicts the predicted square-lattice interference pattern

based on an incidence angle of θ_S = 0.4deg. A CCD image of the actual PIIES interference pattern is depicted in Fig. 6.4(b).

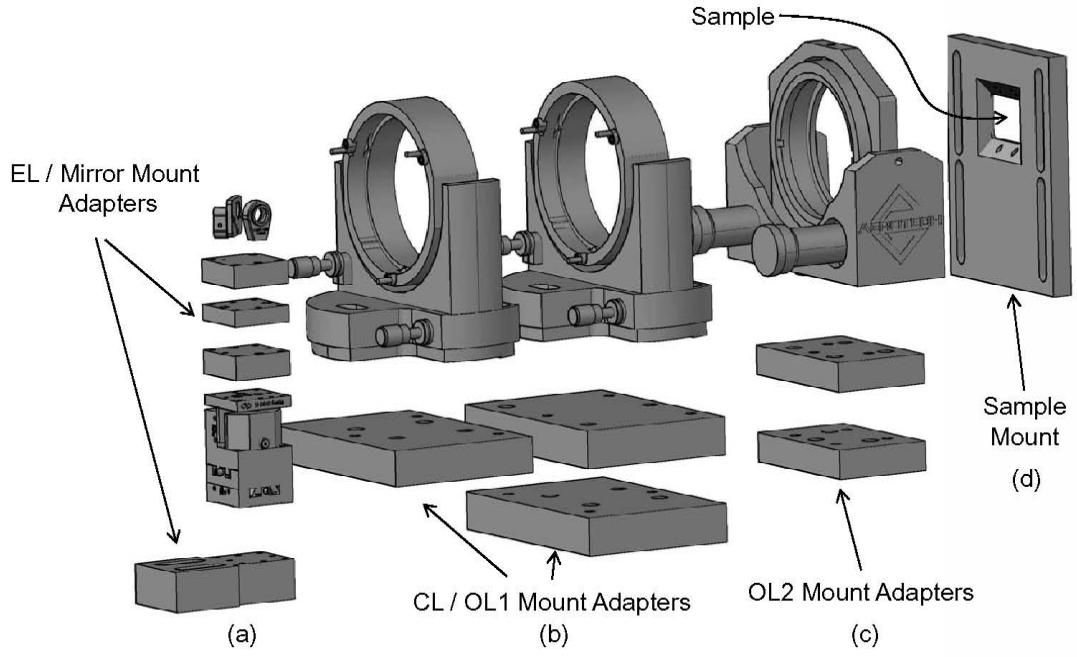

Figure 6.2: Custom PIIES fabricated components. (a) Expander lens / mirror mount adapters. (b) Condenser and first objective lens mount adapters. (c) Second objective lens mount adapter. (d) Sample mount.

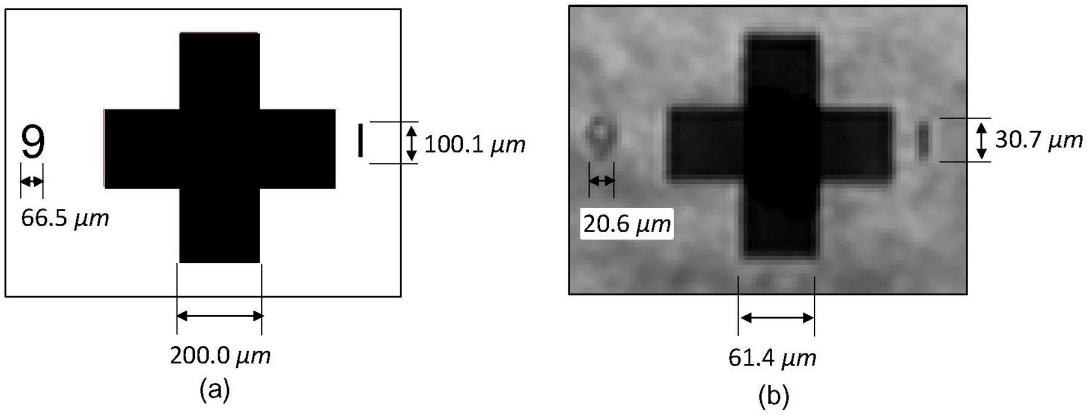

Figure 6.3: Real-time pattern-integrated image monitoring. (b) A CCD camera is used to capture a pattern-integrated image of a (a) Greek cross and fiduciary mark used to facilitate initial focusing.

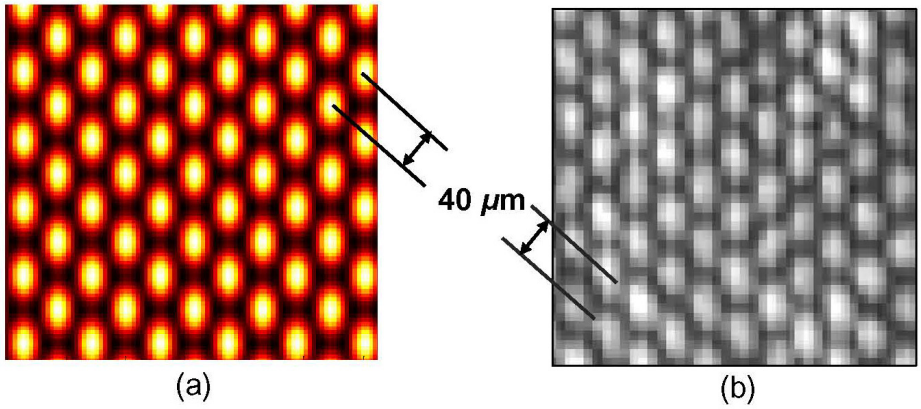

Figure 6.4: Real-time interference pattern monitoring. (a) A Matlab simulation depicts a square-lattice interference pattern based on a $0.4 deg$ incidence angle required for a $40 \mu m$ lattice constant. (b) A CCD image capture depicts the PIIES inference pattern after passing through a 60x microscope objective.

6.2 System Alignment

Both MBI and projection imaging systems present unique implementation challenges. Specifically, opto-mechanical stability and individual beam control are paramount in interferometric systems, while precise objective lens alignment and sample plane positioning are required for successful projection imaging. These implementation challenges are compounded in the PIIES prototype presented here. Accordingly, specific system alignment techniques were developed to ensure proper PIIES functionality. A basic flowchart describing the various steps required to align the system is depicted in Fig. 6.5. Each alignment execution procedure is described in more detail later in this section. In the alignment presented here, the first requirement is to establish the optical axis of the system. Once the physical axis is established, the subsequent sequential alignment steps may be performed. Of note, the experimental fabrication process described in the next section may require that an alignment execution step be repeated. For this reason, multiple starting points are included in the flowchart.

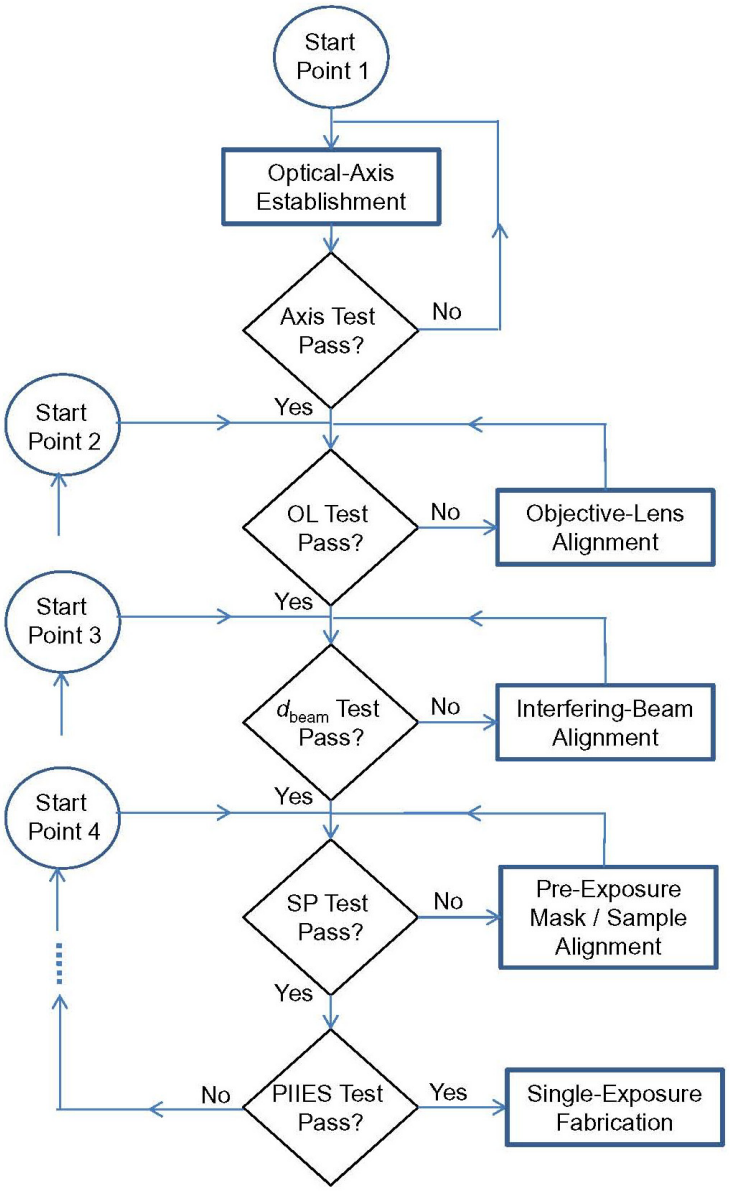

Figure 6.5: PIIES alignment flowchart. After all of the alignment tests are successfully passed, the system is ready for a PIIL exposure.

6.2.1 Optical-Axis Establishment

A rough alignment of all optical components is completed by securing the bases of all components to the table at the approximate locations specified by the Zemax optimization described in Chapter 5. Next, an optical system axis is established with a single beam from the UV laser source. This axis beam is adjusted such that it remains parallel to the

table, propagating in the $-z$ direction, as depicted in Fig. 6.6(a). Next, a mask is secured in the mask mount and positioned such that a single diffractive feature, such as the Greek cross in Fig. 6.7(a), is positioned in the center of the axis beam. The Greek cross creates a diffraction pattern that resembles a crosshair as depicted in Fig. 6.7(b) allowing for easy identification of the optical axis of the system. Next, appropriate opto-mechanical guides are established for an alignment card as depicted in Fig. 6.8 such that the diffraction pattern is centered on the alignment card as it translates along the length of the table (z axis), identified by the alignment card range (ACR) arrow in Fig. 6.6(a). The alignment card and opto-mechanical guides now define the optical axis of the system when the diffractive pattern from the mask that remains centered on the alignment card along the length of the table (*Axis Test* in Fig. 6.5).

Before the lenses are added to the configuration, it is prudent to perform an initial alignment of the three interfering beams along the ACR as depicted in Fig. 6.6(a) ($\mathbf{k}_3$ is not shown for clarity but is parallel to $\mathbf{k}_1$ and $\mathbf{k}_2$ and lies out of the plane of the page and is distinct from the axis beam). This will aid in the final alignment of the interfering beams as discussed in more detail later in this section. To perform the initial interfering-beam alignment, the beam-directing mirrors are adjusted such that the multiple beams are incident on the desired radial beam displacement (d_{beam}) marks on the alignment cards for a square lattice as depicted in Fig. 6.8(a) or a hexagonal lattice in Fig. 6.8(b). For example, a square-lattice with a lattice constant of $a_{\text{sq}} = 1.0\,\mu m$ ($\theta_{\text{S}} = 14.9\,deg$) is obtained when the three beams are adjusted such that they intersect the horizontal and vertical radial lines at $d_{\text{beam}} = 14.4\,mm$ as determined by the Zemax optimization described in Chapter 5. The initial interfering-beam alignment is complete when the beams remain

stationary at the desired beam displacement marks on the alignment card along the length of the ACR.

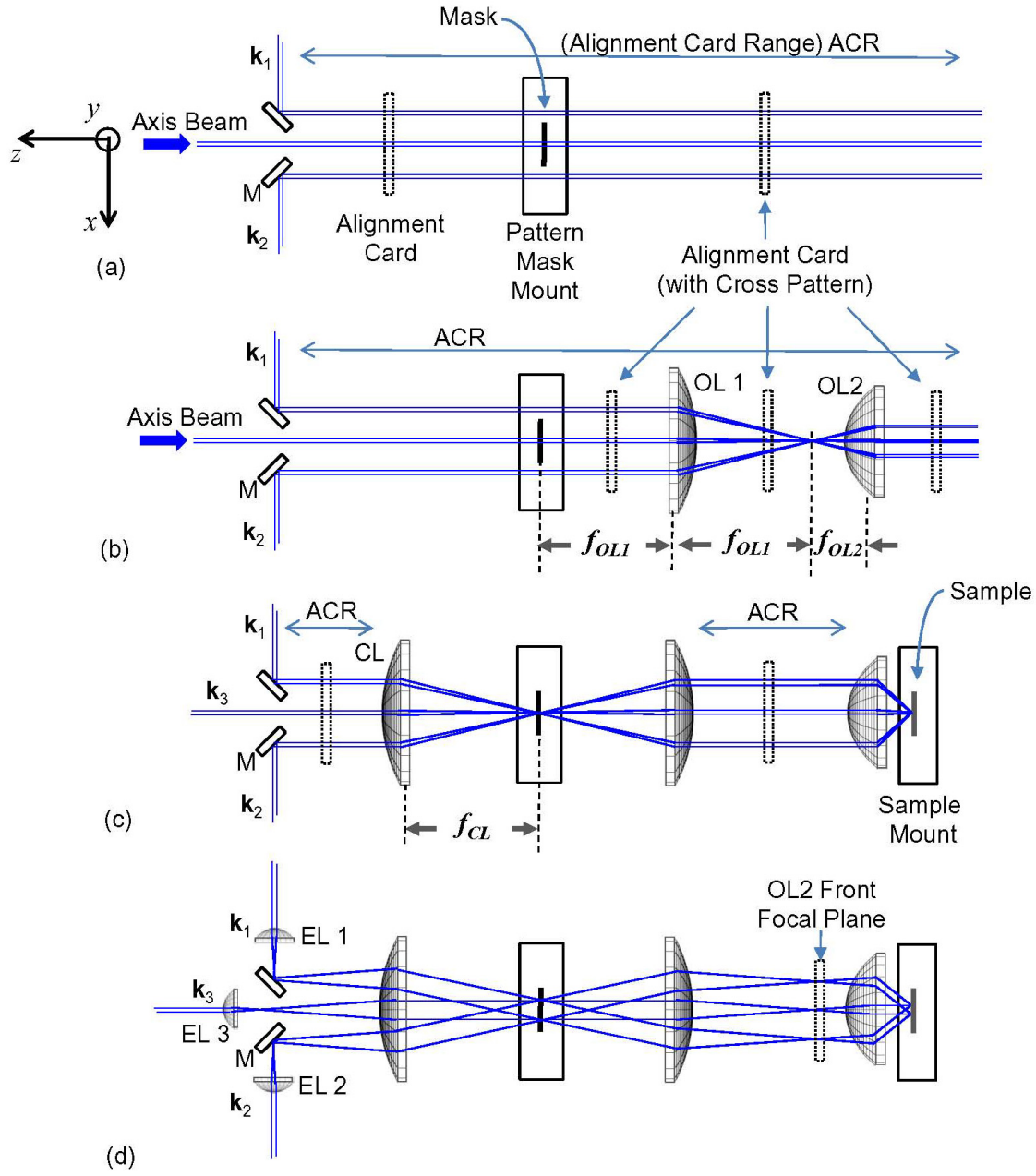

Figure 6.6: PIIES alignment and build sequence. (a) The optical axis is established with an alignment card and a diffractive mask element centered on the axis beam. (b) The two objective lenses are centered on the optical axis using the diffraction pattern from the mask element (c) The condenser lens is positioned and the interfering beams are aligned to the required positions on the alignment card. (d) Expander lenses are added to provide collimated beams at the sample plane and coherent illumination of the pattern mask.

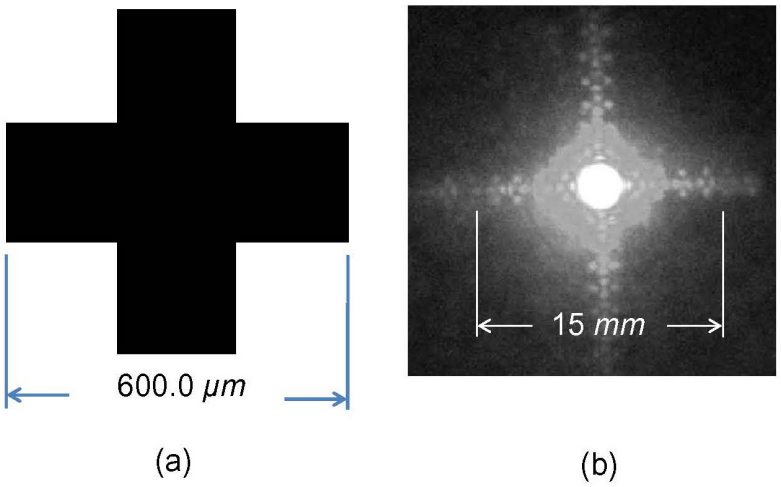

Figure 6.7: Diffractive mask feature. (a) A Greek cross on the pattern mask is centered on the axis beam to create a unique diffraction pattern. (b) The resulting crosshair pattern is used to establish the optical axis of the system and align the objective lenses.

6.2.2 Objective-Lens Alignment

In a properly aligned objective lens system, the Greek cross diffraction pattern remains centered on the alignment card before and after each objective lens, and all beams enter and exit the objective lens system parallel to the optical axis (*OL Test* in Fig. 6.5).

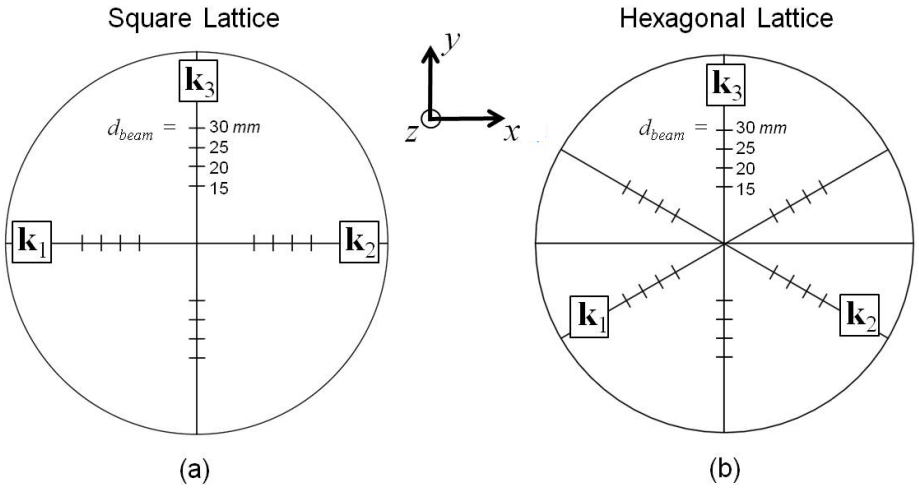

Figure 6.8: Alignment cards for (a) a square and (b) a hexagonal lattice.

After establishing the optical axis, the first objective lens (OL1) is placed after the mask at a distance such that the mask is at the front focal plane of OL1, as depicted in Fig. 6.6(b). All tilt and decentration are removed from the lens such that it is orthogonal to and centered on the optical axis of the system. When properly aligned, the diffractive pattern of Fig. 6.7(b) remains centered on the alignment card along the ACR after the lens. Next, the spacing between the lens and the mask is adjusted using the axial translational stage by 1) obtaining a focused image of the cross at some distance after OL2, and 2) using the lens equation to make the final axial adjustment of the lens to focus the image of the cross at infinity.

To complete the objective lens system build, the second objective lens (OL2) is added to the system. Again, all tilt and decentration are removed from OL2 such that it is orthogonal to and centered on the optical axis of the system, and the diffraction pattern remains centered on the alignment card along the ACR after OL2. Next, OL2 is adjusted such that the spacing between the two objective lenses is equal to the sum of the focal lengths of OL1 and OL2 as depicted in Fig. 6.6(b). In this configuration, the two previously aligned beams on the horizontal axis ($\mathbf{k}_1$ and $\mathbf{k}_2$) enter and exit the objective lens system parallel to the optical axis and in the same relative position on the alignment card. Of course, the beam displacements after the second objective lens will be adjusted according to the ratio of focal lengths of the two objective lenses.

6.2.3 Interfering-Beam Alignment

In a properly aligned PIIES, all three off-axis beams remain centered on the correct radial points on the alignment card, corresponding to the required beam displacement d_{beam}, along the ACR before the CL and between OL1 and OL2, (*SP Test* in Fig. 6.5).

To ensure that the multiple beams are centered on origin at the mask plane (second optimization requirement in Chapter 5), the condenser lens (CL) is added to the system with the mask plane located the CL back focal plane as depicted in Fig. 6.6(c). All tilt and decentration are removed from the lens such that it is orthogonal to and centered on the optical axis of the system. To satisfy the positioning requirements, the CL is adjusted such that all three interfering beams are focused to a common on-axis point at the mask plane. In the configuration presented here, all three focused beams will be blocked by the on-axis Greek cross when the CL is properly aligned.

To ensure axial propagation of the beams between OL1 and OL2 (third optimization requirement in Chapter 5) and set the specific value of θ_S at the sample plane (sixth optimization requirement in Chapter 5), OL1 is adjusted along the optical axis such that the three beams are incident on the alignment card at the correct positions along the ACR between OL1 and OL2 as depicted in Fig. 6.6(c). Of note, the beam positions are now inverted but at the same required radial d_{beam} distances.

Finally, to ensure collimation of the beams at the mask plane (first optimization requirement in Chapter 5) and collimation of the beams at the sample plane (fourth optimization requirement in Chapter 5), each expander lens is added and adjusted such that each beam is incident on the alignment card at the required position for the desired lattice constant and focuses to a point at the front focal plane of OL2 as depicted in Fig. 6.6(d).

6.2.4 Pre-Exposure Mask / Sample Alignment

The PIIES is aligned for the first exposure in the experimental process when the sample plane is positioned approximately at the image plane of the objective lens system (*SP*

Test in Fig. 6.5). As discussed earlier in this section, a CCD camera may be used to confirm the basic pattern-integrated imaging properties of the system. This is particularly useful in gaining an appreciation for the effects of adjustments to various components on the pattern-integrated image in real-time. However, prior to any experimental fabrication it is important to determine an appropriate initial starting position for the sample mount with the surface of the sample positioned approximately at the in-focus image plane.

As a final step before PIIES exposure, the sample plane mount is positioned such the multiple beams intersect at a common point centered on the origin at the sample plane (fifth optimization requirement in Chapter 5). In this step, the expander lenses are temporarily removed from the system and the sample mount is placed after OL2, as depicted in Fig. 6.6(c). Next, an opaque glass slide with the same dimensions as the sample that will be used in the exposure is placed in the sample mount as depicted in Fig. 6.2(d). The sample mount is then adjusted along the z-axis such that all three beams focus to a point at the front plane of the opaque glass slide. The micrometer position for the sample mount axial translation stage, z_{SP0}, is recorded and will serve as the initial-focused position in the experimental procedures presented in the following section. The expander lenses are placed back into the system and the PIIES is now properly aligned for an experiment.

6.3 Experimental Procedures

6.3.1 Fabrication Procedures

A basic lithographic exposure procedure was used to record the PIIES optical-intensity distribution in a thin layer of positive photoresist on a $31.75 mm$ square UV-grade fused quartz slide. First, each slide was chemically cleaned and layered with one micron of

Shipley SC1813 positive photoresist using a SCS G3P8 Spin Coater. After a four-minute soft bake, each slide was exposed for $0.7 sec$ with the PIIES configuration depicted in Fig. 6.1(b). The *x*-axis translation stage for the sample mount allowed for multiple exposures on one prepared slide by adjusted the horizontal position of the slide between exposures. Typically, this procedure allowed for up to eight exposures on one slide. Once the final exposure was complete the slide was developed with a $30 sec$ agitation bath of Microposit MF-319 Developer.

6.3.2 Pattern-Integrated Image Focusing Procedures

To find the precise location of the plane of best focus, two basic experimental procedures were followed. First, a set of initial coarse-focusing exposures was conducted at $2.5 \mu m$ intervals centered around the initial-focused position, z_{SP0}, obtained during the pre-exposure alignment. For example a set of seven exposures would include micrometer positions of z_{SP0}+7.5, z_{SP0}+5.0, z_{SP0}+2.5, $z_{SP0,}$ $z_{SP0} - 2.5$, $z_{SP0} - 5.0$, and $z_{SP0} - 7.5 \mu m$. The initial coarse-focusing exposures were conducted with a relatively large mask feature on axis, such as the Greek cross in Fig.6.3 (a). The exposed slide was then developed and evaluated using an Olympus NC60 microscope with a maximum of 100X magnification in the reflected-light brightfield observation mode. Figure 6.9 depicts example CCD image captures of the Greek cross at various axial sample-mount micrometer positions. From this initial set of coarse-focusing exposures, a new coarse-focused micrometer position, z_{SP1}, is established. For example, the series of CCD images in Fig. 6.9 would establish a course-focused position of approximately $z_{SP1} = z_{SP0} + 1.5 \mu m$.

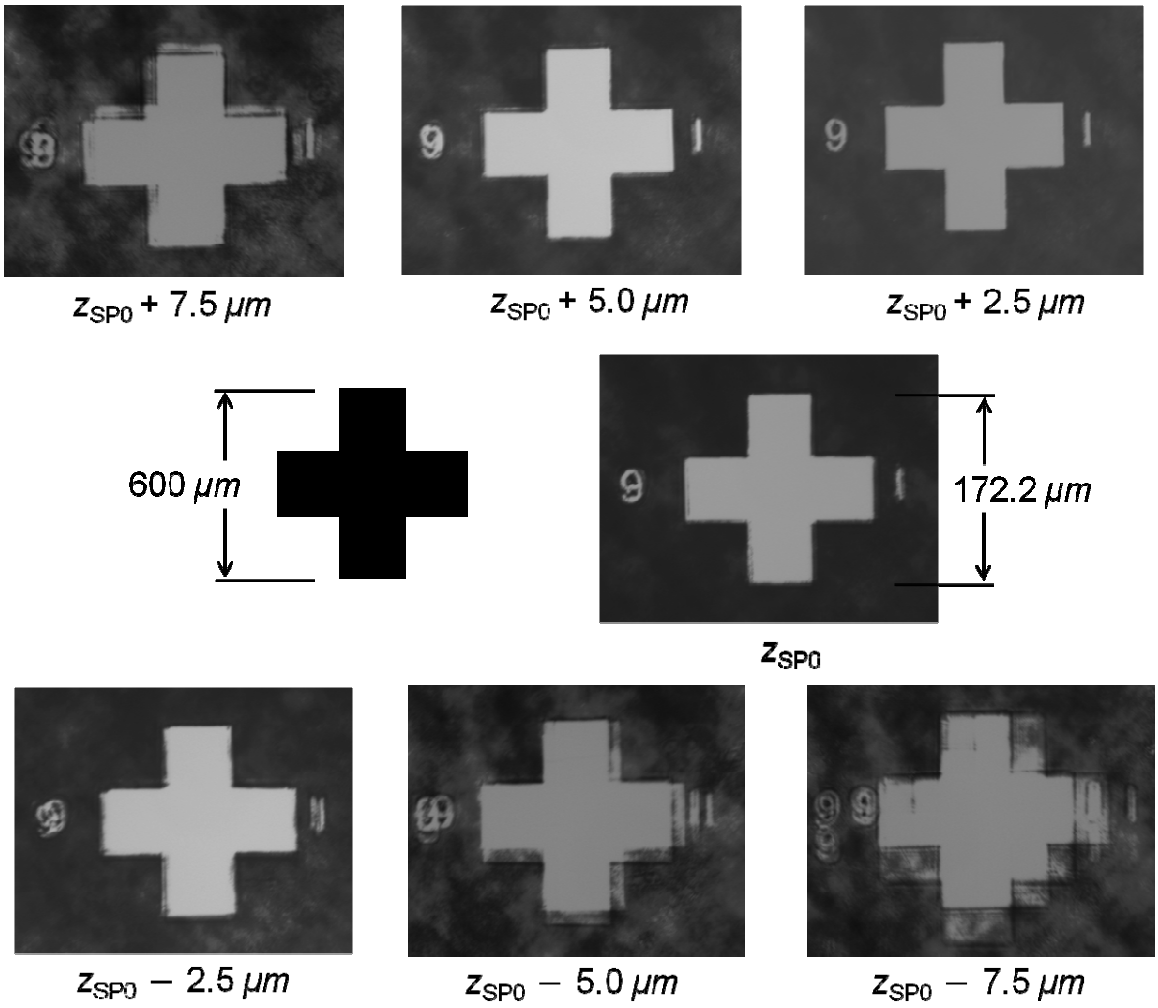

Figure 6.9: Experimental focusing of PIIES. CCD image captures using an Olympus NC60 microscope depict fabricated pattern-integrated images of a Greek cross at z_{SP0} + 7.5, z_{SP0} + 5.0, z_{SP0} + 2.5, $z_{SP0,}$ z_{SP0} − 2.5, z_{SP0} − 5.0, and z_{SP0} − 7.5 μm.

Next, a set of fine-focusing exposures was conducted at 0.5 μm intervals centered around the course focused position, z_{SP1}. This set of exposures should identify a fine-focused micrometer position, z_{SP2}, for the sample mount. Once this final sample mount position is established, the system is ready for PIIL exposure. In the research presented here, exposures of the Greek cross were made. In addition, smaller mask features were positioned on axis for pattern-integrated imaging of representative photonic crystal structures. The final exposed slides presented in the following section were developed

and layered with 20nm of Au/Pd using a Hummer 6 Gold Sputterer and imaged using a Zeiss Ultra60 scanning electron microscope (SEM).

6.4 Single-Exposure Fabrication Results

Through careful system alignment and experimental focusing procedures, the PIIES pattern-integrated optical-intensity distribution was successfully recorded in a positive photoresist in a single-exposure step for two representative fundamental PC structures. First, a relatively large mask feature consisting of a 600.0 x 600.0μm Greek cross as depicted in Fig. 6.10(a) was illuminated with the three off-axis interfering beams and projected to a size of 172.2 x 172.2μm. The resulting pattern-integrated optical-intensity distribution is depicted in the SEM image of Fig. 6.10(b). Next, the model presented in Chapter 5, including the optical system parameters for the experimental configuration (see Appendix B), was used to predict the optical-intensity distribution for a corner of the projected cross as depicted in Fig. 6.10(c). Figure 6.10(d) depicts the magnified SEM view of the corresponding area of the fabricated PC structure, revealing the surrounding square PC lattice defined by black circular regions corresponding to the intensity maxima of the periodic pattern (grey areas indicate areas of intensity minima, while the white areas represent the transition between the points of maximum and minimum intensity). This simulation depicted in Fig. 6.10(c), with intensity grayscale values adjusted to match the SEM image, show very good agreement with the experimental results. In this first experiment, the cross successfully blocked all three beams, preventing the formation of the periodic interference pattern within the projected cross, while transitioning to a well-defined PC lattice within the distance of one lattice constant, demonstrating PIIL's ability to define abrupt transitions within a lattice, such as a PC cavity.

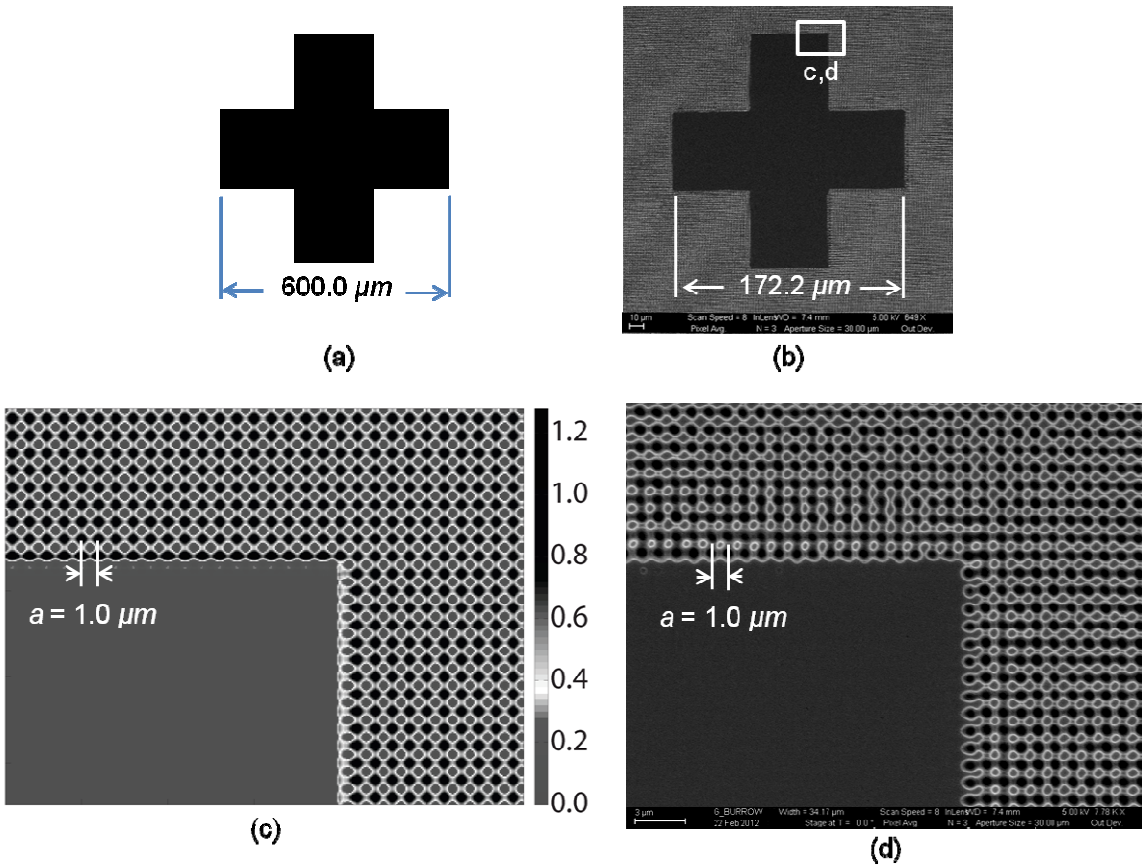

Figure 6.10: PIIES single-exposure fabrication results. (a) A pattern-mask feature of a 600.0 x 600.0μm Greek cross is projected to a size of 172.2 x 172.2μm. (b) An SEM image depicts the resulting single-exposure PIIES optical-intensity distribution of the projected cross and interference pattern. (c) A simulation provides a close-up view of one corner of the cross. (d) A magnified SEM view of the corresponding fabricated area depicts a well-defined corner produced by the projected Greek cross surrounded by the interferomatrically defined square PC lattice with a periodicity of a = 1.0μm.

To demonstrate PIIL's ability to fabricate smaller PC structures, such as a single PC waveguide, a single line segment with mask dimensions of 2.0 x 20.0μm as illustrated in Fig. 6.11(a) was illuminated with the three beams and projected to a size of 0.6 x 5.8μm as depicted in the SEM image of Fig. 6.11(b). Figure 6.11(c) shows the simulated optical-intensity distribution for the PC-lattice points near the projected waveguide segment. The corresponding magnified SEM view of the fabricated line segment is depicted in Fig. 6.11(d) showing the successful elimination of a single row of PC-lattice points. Small deviations of the experimental opto-mechanical system from the perfectly

aligned configuration used in the simulation may account for the qualitative differences between predicted and experimental results. Even with the opto-mechanical deviations present in the PIIES prototype, the experimental results presented in Fig. 6.11 demonstrate the ability of the PIIL to fabricate, in a single-exposure step, a PC waveguide, a fundamental structure in most PC devices. This represents the first single-exposure fabrication of a basic PC waveguide structure via the integration of superposed pattern imaging with interference lithography (IL).

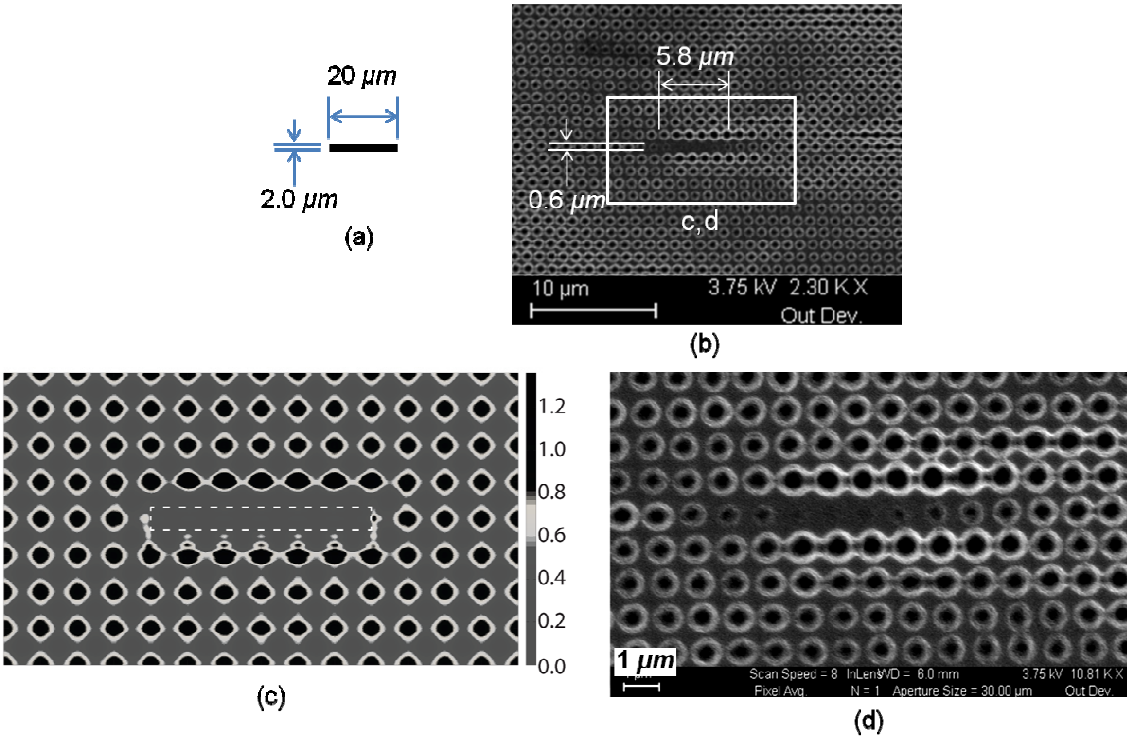

Figure 6.11: Demonstration of PIIL single-exposure PC waveguide fabrication. (a) A pattern-mask feature of a 2.0 x 20.0μm line segment is projected to a size of 0.6 x 5.8μm. (b) An SEM image depicts the resulting single-exposure PIIES optical-intensity distribution of the projected line segment and square-lattice PC. (c) A simulation depicts a close-up view of PC lattice points near the waveguide segment. (d) A magnified SEM view of the corresponding area depicts the selective elimination of a single row of lattice points in the surrounding periodic lattice, demonstrating the ability of the PIIL to fabricate a PC waveguide, the fundamental element of most PC devices.

For the PIIES presented here, the total interference area is approximately $4 mm^2$. Larger interference areas are possible as expander lens focal lengths are decreased, resulting in larger collimated interfering beam diameters at the sample plane as discussed in Chapter 5. From SEM images of the center and of the periphery of the interference area, the lattice constants were typically in the range from 1.02 to $1.06 \mu m$. Lattice-vector angles for **a** and **b** varied typically by less than one degree. These results demonstrate excellent uniformity across the entire periodic pattern.

Based on Zemax simulations, the present PIIES configuration is capable of sub-$500 nm$ periodicities with still smaller periodic features. In other PIIES experiments, lattice constants near $600 nm$ were achieved [72]. Of course, for smaller lattice periodicities, the required beam displacement d_{beam} depicted in Fig. 5.1(c) increases, placing the interfering beams near the limits of the clear apertures of the objective lenses. As a consequence, less of the diffracted energy from the projected mask features is collected by the objective lenses. This, in turn, degrades the quality of the projected mask features. For this reason, the beam displacements were adjusted to be well within the clear aperture limits of the objective lens to assist in focusing the projected mask features for the experimental fabrications presented here. This resulted in a lattice periodicity of $1.0 \mu m$. The initial fabrication results obtained with this relatively simple PIIES prototype and basic experimental procedures demonstrate the fundamental PIIL patterning capability. Future results are expected to be improved with advanced systematic objective lens design (e.g. larger numerical aperture and reduced aberrations), improved opto-mechanical stability and alignment, and advanced lithographic processing techniques.

6.5 Summary

In this chapter, example well-defined PC structures were fabricated with a PIIES prototype, representing the first-ever fabrication of these structures via the integration of superposed pattern imaging with IL in a single-exposure step. These structures exhibited favorable intensity and lattice-vector metrics, demonstrating the potential of PIIL for fabricating dense integrated optical circuits. The PIIES prototype experimental configuration was presented, including detailed system alignment and experimental procedures, serving as a foundation for future system design and enhancements.

CHAPTER 7

CONCLUSIONS

As a part of the 2004 Conference on *Micromachining Technology for Micro-Optics and Nano-Optics*, Prof. Dennis Prather *et al.* from the University of Delaware stated, "Ever since their introduction in 1987, the fabrication of photonic crystals for visible and near infrared wavelengths with controllably placed defects such as waveguides and cavities has been the holy grail of experimentalists working in the area [212]." In their work, Prather *et. al* defined a photonic-crystal (PC) lattice with a three-beam interference lithography (IL) exposure, followed by the use of electron beam lithography to create a functional element. While successful in creating a photonic crystal waveguide, their method, like many others, remains too costly and time-consuming for commercial application. In the method demonstrated in the present research, Pattern-Integrated Interference Lithography (PIIL) offers the first-ever single-step option for the fabrication of 'holy grail' PC waveguide and cavity structures.

The design, modeling, and experimental results using a prototype Pattern-Integrated Interference Exposure System (PIIES) presented in this thesis confirm the potential of PIIL for single-exposure fabrication of a wide range of periodic structures with integrated functional elements. With future research, improved optical system design, and refined processing considerations, PIIL holds the promise of commercially cost-effective wafer-scale fabrication of dense integrated optical circuits.

7.1 Summary of Results

7.1.1 Review of Multi-Beam Application Areas

The invited review paper completed as a part of this research provided a unified, comprehensive review of current multi-beam interference (MBI) applications, including nano-electronics, photonic crystals, metamaterials, subwavelength structures, biomedical structures, and optical trapping [38]. This review complements other MBI review papers that describe MBI methods and capabilities, and will provide researchers across numerous fields with a more thorough understanding of MBI utilization in other application areas.

7.1.2 Two-Dimensional Motif Geometries

To understand better the patterning possibilities afforded by MBI, analytical models were developed to describe the motif geometries associated with the four higher-order plane-group symmetries possible for both square and hexagonal lattices, under the conditions for primitive-lattice-vector-direction equal contrasts using linearly-polarized, three-beam interference [77,78]. The two defining geometric equations and the relationships between the plane-group symmetries were presented, providing the most accurate analytical model to date for these fundamental motif geometries.

The methodology and models developed as a part of this research may be further modified or combined to describe other lower-order symmetry motif geometries that change from the shape of an ellipse to that of an irregular polygon. Given these new analytical descriptions of the motif geometries, researchers may analyze directly the effects of wide range of motif geometries for a particular application using the analytical model alone, without the need for complicated experimentation or computer simulations.

7.1.3 Constrained Parametric Optimization

A systematic and comprehensive analysis of the effects of constraints on individual-beam amplitudes and polarizations was presented for the unique 2D plane-group symmetries possible using three linearly-polarized beams configured to produce an interference pattern with square- or hexagonal-lattice translational symmetry [69,71,77,79]. These patterns were optimized for maximum uniform contrast while satisfying the conditions for primitive-lattice-vector-direction equal contrasts.

When only amplitude constraints are considered, the results demonstrate that all plane-group symmetries remain possible over the full range of lattice constants. While the absolute contrast is reduced to a minimum value of $V_{abs} = 0.88$, this value is still sufficient for optical lithography purposes.

When polarization constraints are introduced, significant reductions were noted for all plane-group symmetries. Based on the specific application requirements, it may be necessary to use an MBI configuration, such as the multiple-beam-splitting configuration used in the PIIES configuration, that allows individual conditioning of beam polarizations to ensure a robust patterning capability.

Although numerous additional parametric constraint combinations are possible, the cases presented here provide useful insight into the general design requirements for an MBI system. Moreover, the optimization methodology presented here may be straightforwardly modified as necessary to model and predict the patterning possibilities of other constrained configurations to ensure that the a given MBI configuration meets the requirements for a specific patterning application.

7.1.4 Pattern-Integrated Interference Lithography

In this chapter, the *ad hoc* design, optimization, and modeling of the PIIES were introduced [69,71-76]. Using a novel three-beam interference system with an integrated projection imaging capability, PIIES was designed to produce a uniform PC lattice with integrated functional elements in a single-exposure step. To confirm this potential, Zemax optimization and simulation results were presented, demonstrating the possibility for wafer-scale uniform periodic patterning. Through the use of maskless MBI high-spatial-frequency patterning, PIIL should reduce the diffraction limitations of using traditional projection lithography alone, especially when the desired integrated pattern contains regular underlying grid patterns, such as seen in PC devices.

To understand better and predict the pattern-integrated imaging capabilities of the PIIES configuration, a new Fourier model was developed by modifying the three-beam plane-wave intensity distribution to include a complex description of each interfering field that includes the integrated projected pattern-mask information. Using this model, new performance metrics were developed to characterize the functional element and surrounding lattice point amplitudes and lattice vectors. Even with relatively low-cost commercially available optics, simulations indicated that the prototype PIIES would be able to produce the desired photonic crystal structures

7.1.5 Fabrication of Photonic-Crystal Structures

As a demonstration of the PIIL method, example well-defined PC structures were fabricated with a PIIES prototype, representing the first-ever fabrication of these structures via the integration of superposed pattern imaging with IL in a single-exposure step [69,71-76]. These structures exhibited favorable intensity and lattice-vector metrics,

demonstrating the potential of PIIL for fabricating dense integrated optical circuits. To support future system design and enhancements, information about the PIIES prototype experimental configuration was presented, including detailed system alignment and experimental procedures.

7.2 Future Work

7.2.1 PIIL and PIIES Development

In the *ad hoc* design and development of the PIIES prototype optical configuration presented in this research, only on-axis projection patterning was considered in order to demonstrate PIIL functionality. While rudimentary design considerations and experimental procedures were employed to minimize on-axis spherical aberration, no effort was made to minimize the off-axis aberrations. These aberrations will become significant in future design efforts to produce dense functional elements over a large area, especially considering the large-angle multi-beam off-axis illumination required by the PIIES configuration. As described in previous work concerning traditional projection lithography, off-axis illumination requires detailed analysis of the diffracted energy in the objective lens pupil, with specific consideration given to reducing aberrations in order to image accurately both on- and off-axis mask features over a large area [312]. These design considerations change with the pattern-mask feature size, shape, and density. In the PIIES configuration presented here, these same design considerations may be applied systematically to improve the optical configuration and allow for more precise modification of the interference pattern to create functional wafer-scale integrated optical circuits.

In the PIIES configuration presented in this thesis, interference patterning may be accomplished over a large area and is not greatly constrained by traditional diffraction limitations or depth of focus issues. However, this interferometric patterning capability does introduce new optical system design considerations. Specifically, to obtain a high-contrast uniform periodic optical-intensity distribution, the objective lens, in combination with the illumination optics, should be designed to produce a specific configuration of collimated interfering beams at the incidence angles required to produce the desired periodicity. The initial PIIES experimental results demonstrate that uniform interference patterning is consistently achieved even with the rudimentary optical configuration used here. Significantly larger interference areas with specific lattice symmetries are possible. Future research and design efforts may be oriented to the optimization of PIIES, while ensuring a uniform MBI-defined periodic pattern.

To apply PIIL in the semiconductor industry and other nanoscale fabrication efforts, larger NA systems must be developed to reduce the minimum feature size. Fortunately, the same research and development of high-NA systems for the semiconductor industry should be of benefit to the development of PIIL [313,314]. Fundamentally, higher NA systems will allow for larger incidence angles at the sample plane, corresponding to smaller period lattice patterns. With the reduced period, smaller projected mask features will be required. Of course, higher-NA systems will facilitate accomplishing this. It is anticipated that the resolution limits of the PIIL method will be similar to those of traditional projection lithography. PIIL may prove to be superior in two ways: 1) the diffraction-limited imaging resolution may be superior since the high-spatial-frequency patterning is formed by maskless MBI, and 2) the projected mask features need only

modify the interference pattern, possibly reducing the required effective resolution of the integrated imaging system.

7.2.1.1 Modeling

As newer PIIES designs with larger numerical apertures (NA) are developed, the scalar model presented here must be extended to cover high-NA effects and finite mask thicknesses. Specifically, the nonparaxial model must be modified to include polarization effects as NA values exceed 0.6 [310]. These polarization considerations will affect both the projected integrated-image and the periodic interference pattern.

In modeling the PIIES response, it will be appropriate to understand the system response to a single blocked pixel. For example, the blocking element in the mask plane might be an undersized pixel or an oversized pixel. Also, the pixel might not necessarily be a square, but can have various shapes like a circle, a triangle, or an octagon, as depicted in Fig. 7.1. Recent research in this area suggests that, through proper single-pixel design, interference motifs may be selectively modified, thereby minimizing the effects on the surrounding periodic pattern. Also, the system response to a single pixel may provide valuable guidance regarding the PIIES response to more complex realistic patterns. Convolution of a single pixel response with an array of delta functions may be an efficient approach to compute the response of a more complex pattern. As high densities and large lumped functional elements are considered, the present model may be helpful to quantify the PIIES capabilities, such as in micro- and nano-electronic applications. Finally, a spatial-frequency filter added at the PIIES Fourier plane can be modeled and the resulting aerial images can be simulated. The filtering can be binary in phase and/or in amplitude or it can be continuous in phase and/or amplitude.

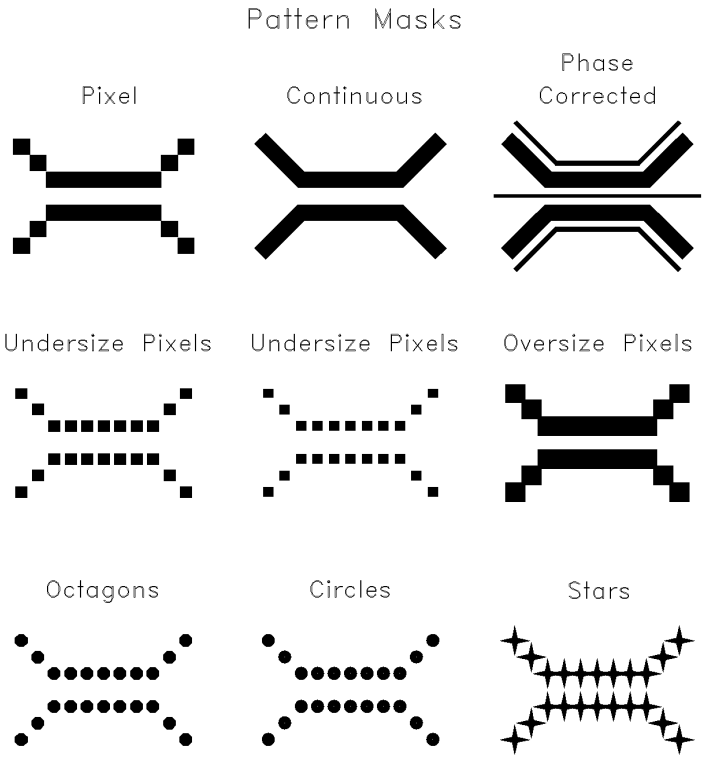

Figure 7.1: Alternative pattern mask options.

Additionally, the fundamental model may take into account the partial coherence inherent in the interfering beams. Partially coherent illumination at the PIIES sample plane is expected to degrade the absolute contrast of the interference pattern as the range of angles produces spatially shifted and superimposed interference patterns. Also, the minimum feature size will increase as the beams become less coherent at the mask plane. However, the "ringing" effect around an image is reduced with the decreasing degree of coherence of the beams illuminating the mask [315]. Reducing this effect by using intentionally introduced partial coherence may minimize the distortion effects on the nearest-neighbor motifs in the interference pattern. This should improve the photonic bandgap of the PC structure. According to modeling conducted as a part of this research, PIIES elements may be arranged such that partial coherent illumination occurs at the

mask plane, while maintaining collimated interfering beam at the sample plane, resulting in possible unity absolute contrast.

Together with the fundamental model, Zemax optical system design software will be a powerful tool to model and understand PIIES capabilities. First, Zemax provides the Zernike coefficients and the root-mean-square (RMS) optical path difference (OPD) of the PIIES compound objective lens. These parameters are useful to quantify the image quality at the PIIES sample plane. An acceptable diffraction-limited lens system would minimize the Zernike coefficients and produce no more than 0.25 waves RMS OPD [307]. Future design efforts may be oriented to fulfill these requirements. Second, in understanding the effects of misalignment, it will be necessary to perform a sensitivity analysis of the system by inducing tilt and decentration of PIIES elements. This investigation is crucial as it may provide helpful information regarding: 1) PIIES elements that require more precise alignment, 2) more precise Zernike fringe coefficients to better predict the PIIES imaging capability, and 3) more accurate beam profiles and lattice parameter metrics at the sample plane.

7.2.1.2 Experimental Implementation

The existing PIIES configuration has produced very encouraging initial results. However, there has not been a concerted attempt to fabricate more complex and larger-area devices. The experimental construction of such devices will be necessary to establish the capabilities and limitations of the existing PIIES configuration and PIIL in general. At the same time, such experiments will inevitably provide guidance toward modifying and improving such systems. The sensitivity analysis results from modeling need to be compared with the corresponding experimentally measured sensitivities.

Given the inherent interferometric nature of PIIES, it is anticipated that there will necessarily be very small tolerances on the positioning and alignment of the optical elements. The incorporation of an autocollimator (or a laser interferometer) into the PIIES configuration may be necessary in order to achieve and maintain the precision required in positioning and alignment. Wavefronts at various points in the system may need to be evaluated quantitatively (possibly in terms of their Zernike coefficients) and modified in order to achieve large-area exposures of suitably high quality.

In order to improve PIIES positioning tolerance, amplitude and/or phase spatial light modulators (SLMs) may be incorporated into the system. For example, an SLM may be used as mask, enabling more precise control of various patterns, while providing a fast and efficient method to modify complex amplitude and/or phase mask patterns. As an element of the illumination system, an SLM may be used to control precisely the point sources positions and coherence, thereby simplifying the current illumination system and improving the illumination over a large area at the PIIES sample plane. Finally, an SLM may be incorporated in the Fourier spatial-frequency plane.

For large area exposures, future research may be oriented to scanning beam interference lithography, a technique capable of patterning large-area linear gratings and used in the fiber optics industry [172,316-320].

7.2.2 Diffractive Photo-Mask

While future work should focus on enhancing the PIIES design for wafer-scale pattern-integrated imaging, future research may also provide alternative configurations to implement PIIL. Specifically, new designs are needed to overcome the interferometric instability of the amplitude-splitting configuration used to generate the multiple

interfering beams in the PIIES configuration. One option developed as a part of this research is a diffractive photo-mask (DPM) as depicted in Fig. 7.2 [74].

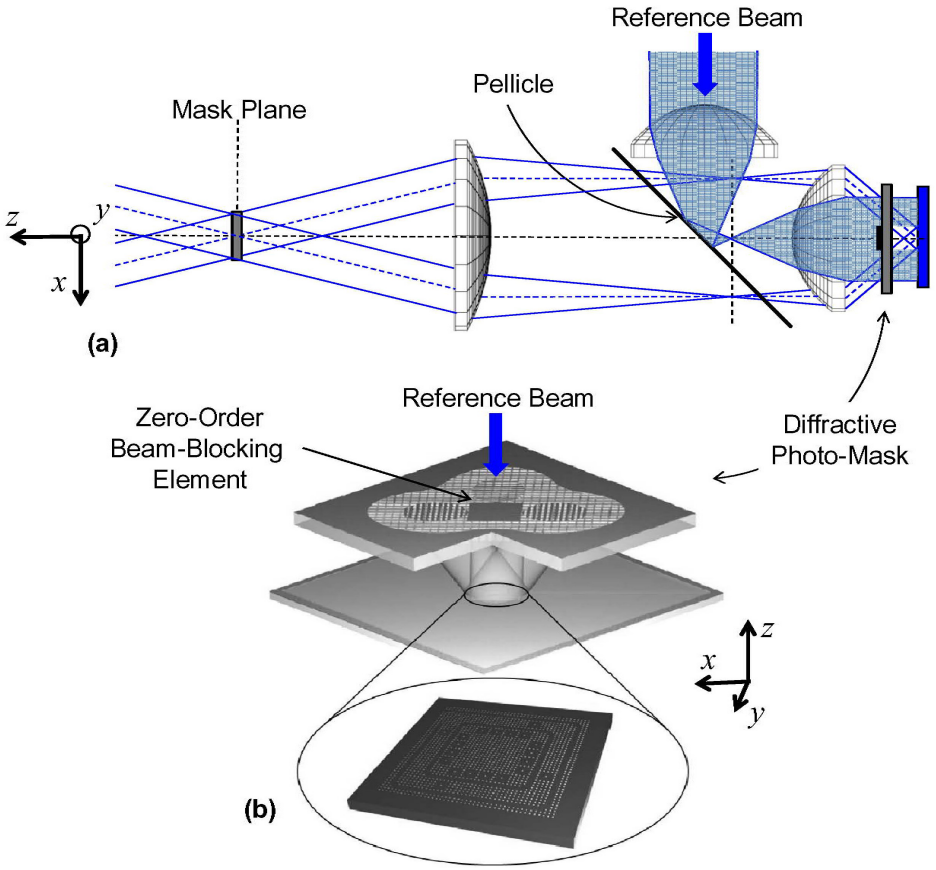

Figure 7.2: Diffractive photo-mask. (a) A reference beam, pellicle, and holographic recording substrate are incorporated into the PIIES to record a diffractive photo-mask (DPM). (b) The DPM then reproduces the multipile PIIES beams when illuminated by the collimated reference beam to produce a PIIL optical-intensity distribution in an interferometrically stable system.

The DPM presented here would be fabricated by incorporating a pellicle between the two objective lenses as depicted in Fig. 7.2(a) to combine the PIIES beams with a reference interfering beam to record interferometrically the multiple beams and integrated pattern-mask information in a holographic recording substrate between the objective lens and the sample plane. In this case, the reference beam, derived from the same source as the PIIES beams, is incident on the pellicle, a portion of which is reflected towards the

objective lens so that it is focused at the front focal plane of the objective lens as depicted in Fig. 7.2(a). This produces the collimated interfering reference beam required to record simultaneously the multiple PIIES beams used to form the pattern-integrated optical-intensity distribution at the sample plane. The result is a complex hologram grating recorded on the surface of the DPM.

As depicted in Fig. 7.2(b), when appropriately illuminated by the collimated reference beam used in the holographic recording process, the DPM should reproduce the original PIIES beams to form the same optical-intensity distribution at the sample plane, again in a single-exposure step. However, now this alternative PIIL implementation has two distinct advantages over the PIIES. First, by using a single diffractive element in close proximity to the sample plane, the DPM is essentially phase-locked, representing an interferometrically stable PIIL fabrication method. Second, the integrated pattern-mask image remains properly positioned within the surrounding MBI-defined lattice, assuming it was properly aligned during the recording of the photo-mask.

In the DPM presented here, there are no chrome or metallic patterns at the bottom of the mask (or anywhere within the photo-mask) to define the non-periodic functional elements. Not having a chrome or metallic pattern at the bottom of the mask eliminates the usual problem of the mask degrading upon repeated use due to deterioration of the metallic pattern when it is used in a contact lithography mode of operation. The proposed photo-mask eliminates this problem by having all of the diffractive elements at the top of the photo-mask and/or within the body of the photo-mask.

As a result, the DPM proposed here should provide the potential for relatively simple, subwavelength, and cost-effective periodic patterning with integrated non-

periodic functional elements in a commercial setting. The PIIES would remain a key tool for research, development, and fabrication of the DPM used to implement PIIL.

7.2.3 PIIL and PIIES Application Areas

As documented in this research, MBI is already widely used in numerous fields including nano-electronics, biomedical structures, optical trapping, metamaterials, and numerous other subwavelength structures. With the PIIL methodology presented here, MBI may have even broader impacts within each of these fields. Future research could focus on developing the PIIL method and PIIES configuration for any one of the areas reported in this thesis. For each of the areas employing PIIL, new specifications and metrics, such as the PC lattice metrics presented in this thesis, may need to be developed to understand better the performance and assist in design efforts,. In addition, the motif geometry models presented in this thesis should allow researchers to analyze directly the effects of wide range of motif geometries for a particular application, and may be included in the study of any PIIL implementation.

7.2.3.1 Nano-Electronics

Perhaps of most significance, the development of PIIL in support of semiconductor industry requirements may be the subject of considerable interest. Modern integrated circuits have very regular layouts with an underlying grid pattern that may be defined by PIIL, while simultaneously including an integrated non-periodic trim pattern. The PIIES and DPM development proposed in this section could make PIIL directly applicable to the semiconductor industry. To help reduce the minimum feature size possible with PIIL, other methods, such as reduced source wavelengths and immersion techniques may be considered. As PIIL becomes an option for the nano-electronics industry, circuit design

may be adjusted to take advantage of the maskless periodic-patterning capability. For example, gridded design rules (GDR) have been proposed by a new start-up company, Periodic Structures, Inc., that considers IL as the "optical lithography of last resort [321]." Using GDR, integrated circuit layers are developed based on a coarse grid corresponding to a two-beam interference fringe pattern, such as the composite pattern depicted in Fig. 1.9(b) [10,211]. With an integrated trim-pattern capability, GDR may be further using PIIL.

7.2.3.2 Three-Dimensional Photonic Crystal Structures

While the work presented in this thesis demonstrated the ability of PIIL to produce 2D PC structures, future research may focus on extending the method to the production of 3D PC structures using four or more interfering beams. For example, a 3D face-centered-cubic PC structure may be created by four-beam IL as depicted in Fig. 2.1(a) [19]. Fortunately, interference patterning is not greatly constrained by traditional depth of focus issues. New methods or modifications to the PIIIES configuration are needed to extend PIIL application to 3D PC structures.

7.2.3.3 Biomedical Structures

As established in the review of MBI applications in this thesis, numerous biomedical structures require a periodic or quasi-periodic matrix for uses such as scaffolds for bone and nerve regrowth. In some cases the MBI-defined pattern may be further modified by an integrated mask image to produce a well-defined patterned area such as the relatively large triangular cells with MBI-defined square-lattice structures on the surface of the cells depicted in Fig. 2.8(c) [21]. In other cases, the individual motifs may be separated or isolated by selectively removing one or more of surrounding motifs in the periodic

pattern. The geometrical shape of the motifs may be further modified using the models presented in this thesis to impact cell behavior in applications such as tissue engineering and biosensors [25]. In each of these example cases, the simplified fabrication process with the individual beam conditioning afforded by PIIL may assist both research and clinical efforts.

7.2.3.4 Optical Trapping

With the PIIES configuration presented in this thesis, it is possible to add dynamic control to the individual-beam parameters to modify the translational and plane-group symmetries and associated motif geometries. When applied to optical trapping, an enhanced PIIES configuration would allow for dynamic trapping and manipulation of subwavelength particles without the need for complex computational algorithms required for holographic optical trapping. Furthermore, the orientation of the trapped particles may be further controlled by changing the geometry of the trapping motif in controlled manner. For example, by producing a *cmm* motif (Fig. 3.9) and gradually changing the shape to *pmm* (Fig. 3.5), a trapped particle, such as a rod-shaped bacterium, may be dynamically rotated [290]. In addition, with the integrated pattern-mask, individual or groups of lattice points may be formed to trap selectively and manipulate groups of particles such as the 19-sphere hexagonal array of $2\mu m$ diameter silica spheres in Fig. 2.9(c) [26]. In this application, new specifications and metrics may include motif sizes and shapes, separation distances, and 3D intensity profiles.

7.2.3.5 Metamaterials

As documented in this thesis, IL has been successfully used to develop numerous metamaterial structures such as magnetic atoms and double-split ring resonators. Much

like photonic crystal devices, integrated non-periodic elements are required to produce truly dense integrated photonic circuits and systems that are very compact in size and highly field-portable. As the size scale of these devices is much smaller than the wavelength of light, the development of the PIIES and DPM to produce smaller features sizes, including 3D metamaterial structures, is required.

7.2.3.6 Subwavelength Structures

As micro- and nano-technology efforts continue to expand to other subwavelength structures, PIIL should find further application. Whether used in the fabrication of surface-relief gratings, anti-reflection surfaces, field-emission displays, plasmonic devices, or direct surface texturing, the PIIL method and the PIIES and DPM implementations presented here could play an important role in the development and commercial realization of integrated devices and structures. For example, PIIL could be used to fabricate the MBI-defined nanopillar arrays patterned in the hierarchical structure of Fig. 2.6(b), mimicking the surface of a lotus leaf, for enhanced hydropholic phenomenon [276]. With control over individual beam amplitudes and polarizations in the present PIIES configuration, subwavelength structures with characteristic motifs, such as the "moth-eye" anti-reflection surface, may be designed and fabricated using the motif geometry models developed in this research [183,255-258].

Until now, the application of IL was limited to strictly periodic patterns with limited control over space-group symmetries and motif geometries. With PIIL, a wide variety of subwavelength periodic patterns with integrated non-periodic features is now possible in a single-exposure step.

7.3 Concluding Remarks

While the current research has focused on the demonstration and fabrication of PC structures, PIIL and has the potential to impact an increasingly wide variety of application areas as proposed in the future work. As one reviewer of the primary manuscript [75] that supports this research stated,

> "The paper presents a new technique for the patterning of photonic crystals … in one setup resulting in an effective if not to say revolutionary single-exposure approach. The first experimental results are rather encouraging. The technique may have big potential not only for the manufacturing of photonic elements but also for the semiconductor technology and related fields."

As documented in this thesis, IL is already the subject of research and commercial development in the micro and nanoelectronics industry. Using the PIIL methodology presented here, multiple IL and traditional optical lithography exposures may be combined into a single step. With new circuit layouts, refined fabrication techniques, and enhanced PIIES designs, PIIL may allow the semiconductor industry to continue to meet the predictions of Moore's law.

APPENDIX A

ZEMAX SYSTEM OPTIMIZATION

The Pattern-Integrated Interference Exposure System (PIIES) configuration developed in Chapter 5 was modeled with Zemax [309] using the specifications for commercial large-diameter aspheric UV lenses. A Thorlabs [322] 100 *mm* diameter, 200 *mm* focal length aspheric lens (AL100200-B) was selected for both the condenser lens and the first objective lens. A Thorlabs 75 *mm* diameter, 60 *mm* focal length aspheric lens (AL7560-A) was selected for the second objective lens. A mounted Thorlabs 6.48 *mm* diameter, 11 *mm* focal length aspheric lens (A220TM-A) was selected for the three expander lenses. Based on the Thorlabs specification sheets for each lens, the optical system lens data used in the Zemax simulation is listed in Tables A.1 and A.2. The resulting Zemax 3D layout is depicted in Fig. A.1 for a single beam with labeled surface numbers.

Table A.1: Zemax PIIES lens data.

Surface Type	#	Radius (*mm*)	Thickness (*mm*)	Semi-Diameter (*mm*)	Note
Even Asphere	1	5.97	5.00	5.00	Expander Lens - See Table A.2
Standard	2	-72.47	Variable	5.00	
Coordinate Break	3		0.00	0.00	Decenter Y (*mm*) - Variable
Even Asphere	4	102.24	19.00	5.00	Condenser Lens - See Table A.2
Standard	5	Infinity	Variable	0.00	
Standard	6	Infinity	Variable	0.00	
Standard	7	Infinity	19.00	50.00	
Even Asphere	8	-102.24	Variable	50.00	Objective Lens 1 - See Table A.2
Even Asphere	9	43.84	35.50	37.50	Objective Lens 2 - See Table A.2
Standard	10	Infinity	Variable	37.50	
Standard	11	Infinity	0.00	0.00	

Table A.2: Zemax PIIES aspheric lens equation data.

	Aspheric Lens Equation Term						
#	Conic	2nd order	4th order	6th order	8th order	10th order	12th order
2	0.00		-3.383558E-4	-1.30539E-5	1.09825E-6	-1.374268E-7	5.49555e-9
6	-1.317766		8.682E-8	1.7733E-13	1.9032E-17		
10	-1.317766		-8.682E-8	-1.7733E-13	-1.9032E-17		
11	-0.750486	4.713E-3	1.615609E-6	3.725877E-10	9.893012E-14	1.099179E-17	

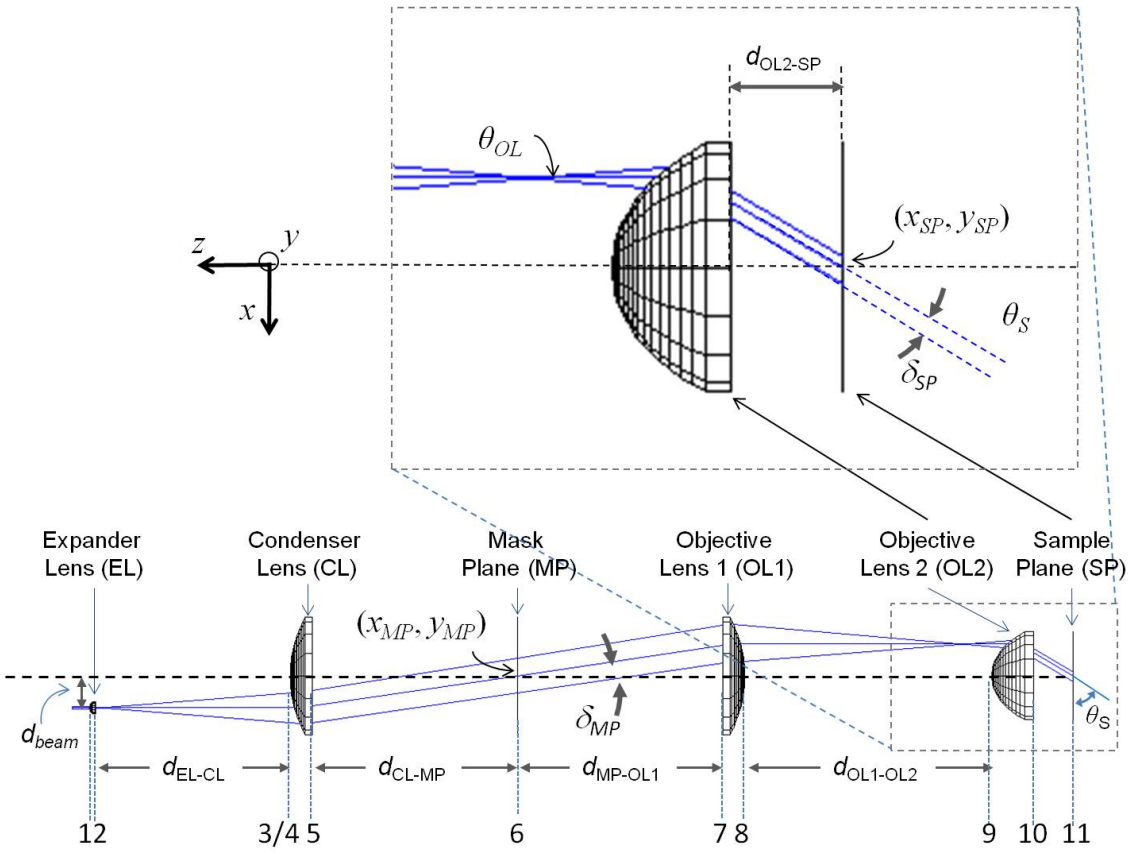

Figure A.1: PIIES configuration showing parameters to be optimized via Zemax. Each surface is numbered according to Table A.1. The beam displacement, d_{beam}, and the distances between each component along the optical axis, $d_{EL\text{-}CL}$, $d_{CL\text{-}MP}$, $d_{MP\text{-}OL1}$, $d_{OL1\text{-}OL2}$, and $d_{OL2\text{-}SP}$, are optimized for (1) collimation of the beam at the mask plane (δ_{MP} = 0), (2) centering of the beam on the origin at the mask plane (x_{MP}, y_{MP} = 0, 0), (c) axial beam propagation between the first and second objective lenses (θ_{OL} = 0), (d) collimation of the beam at the sample plane (δ_{SP} = 0), (e) centering of the beam on the origin at the sample plane (x_{SP}, y_{SP} = 0, 0), and (f) the specific value of θ_S at the sample plane (θ_{SP} = target value).

Figure A.1 depicts the key system parameters that are considered in the optimization of the system configuration, based on the PIIES design and optimization presented in Chapter 5. Specifically, the beam displacement and axial distances between each component (set as variables in Table A.1) are optimized for 1) collimation of the beam at the mask plane ($\delta_{MP} = 0$), 2) centering of the beam on the origin at the mask plane (x_{MP}, $y_{MP} = 0, 0$), 3) axial beam propagation between first and second objective lenses ($\theta_{OL} = 0$), 4) collimation of the beam at the sample plane ($\delta_{SP} = 0$), 6) centering of the beam on the origin at the sample plane (x_{SP}, $y_{SP} = 0, 0$), and 6) setting the specified value of θ_S at the sample plane (θ_{SP} = target value).

The Zemax optimization method used to determine the optimal PIIES configuration employs a routine that seeks to find a local minimum for the merit function

$$MF^2 = \frac{\sum W_i \left(V_i - T_i\right)^2}{\sum W_i}, \tag{6.1}$$

where W is the absolute value of the weight of the operand, V is the current value, T is the target value and i indicates the operand number [306]. In this method a root-mean-square algorithm is employed by calculating the square root of the average value of the squares of the individual errors. Table A.3 lists the operands that were included in the merit function to determine the optimal values for the inter-lens spacing and required beam displacement as described in Chapter 5. For the data presented in Table A.3, a target incidence angle was of $\theta_S = 25.39 deg$ was selected, corresponding to a $600 nm$ square-lattice constant. In the merit function, RAID is the ray angle of incidence with respect to the surface normal, REAX and REAY are the ray x- and y-coordinate positions at the specified surface, and Px and Py are the normalized pupil coordinates.

Table A.3: Optimization requirements and Zemax merit function operands.

Optimization Requirement	Merit Function		
	Operand	Target value	Surface #
Collimation at mask plane ($\delta_{MP} = 0$)	RAID (Px=0, Py=0) – RAID (Px=0,±1, Py=±1,0)	0.00	6
Centered on axis at mask plane ($x_{MP}, y_{MP} = 0, 0$)	REAX and REAY	0.00	6
Axial propagation between OL1 and OL2 ($\theta_{OL} = 0$)	RAID (Px=0, Py=0)	0.00	9
Collimation at sample plane ($\delta_{SP} = 0$)	RAID (Px=0, Py=0) – RAID (Px=0,±1, Py=±1,0)	0.00	11
Centered on axis at sample plane ($x_{SP}, y_{SP} = 0, 0$)	REAX and REAY	0.00	11
Target incidence angle at sample plane ($\theta_{SP} = 25.39 deg$)	RAID (Px=0, Py=0)	25.39	11

APPENDIX B

ZERNIKE FRINGE COEFFICIENTS

To simulate the Pattern-Integrated Interference Exposure System (PIIES) optical-intensity distribution using the model presented in Chapter 5, representative optical system parameters are needed. The accuracy of the model depends on these parameters, specifically the Zernike fringe coefficients. For well-corrected systems with small Zernike fringe coefficients, aberrations are minimized, and the projected image quality is limited primarily by the ability of the objective lens system to collect the diffracted light from the mask. For Figs. 5.9-13, Zemax models and manufacturer lens specifications were used to obtain the system parameters for the projection system formed by objective lens 1 (Thorlabs AL100200-B) and objective lens 2 (Thorlabs AL7560-A). All illuminating beams were assumed to be collimated and modeled as coherent plane waves. The common incidence angle, θ_M, and azimuthal angles, φ_i, of each illuminating beam were optimized in Zemax to produce the desired wavevector configuration at the sample as required for a lattice constant of $600\,nm$ and a square translational symmetry oriented as depicted in Fig. 5.1(b). Individual beam linear polarizations were selected to produce *p4m* plane group symmetry. The resulting parameters for the objective lens system used in the simulations for PC waveguide coupler depicted in Figs. 5.9-13 are given in Table B.1. The Zemax-derived values for the Zernike fringe coefficients at the design wavelength of $780\,nm$ are given in Table B.2. These values provide coefficients

consistent with the literature and are representative of the values that should be possible for the same lenses, corrected for the UV wavelength of $363.8\,nm$ used in the present work.

Table B.1: Objective lens parameters for PC waveguide coupler in Figs. 5.9-13.

Parameter	Value
λ	$363.8\,nm$
$\mathbf{k_1}$	$2\pi/\lambda$ (-0.30 -0.30 -0.90)
$\mathbf{k_2}$	$2\pi/\lambda$ (0.30 -0.30 -0.90)
$\mathbf{k_3}$	$2\pi/\lambda$ (-0.30 0.30 -0.90)
$\hat{\mathbf{e}}_1$	(-0.44 0.81 0.38)
$\hat{\mathbf{e}}_2$	(-0.89 0.18 0.42)
$\hat{\mathbf{e}}_3$	(0.25 0.96 0.12)
θ_M	$7.24\,deg$
φ_i	(45 135 -45) deg
f_2	$56.78\,mm$
CA_2	$57.73\,mm$
$\lvert m \rvert$	0.30

Table B.2: Zernike fringe coefficients for PC waveguide coupler in Figs. 5.9-13.

Zernike Fringe Coefficient	Value (nm)
Z_1	11.33
Z_4	8.57
Z_9	-7.16
Z_{16}	-0.89
Z_{25}	1.34
Z_{36}	-1.80
Z_{37}	0.41

To simulate the experimental optical-intensity distributions for comparison with the fabrication results for the Greek cross and line segments depicted in Figs. 6.10 and 6.11, Zemax was again used to obtain the system parameters for the PIIES projection system. However, to match the experimental configuration, the common incidence angle θ_M of each illuminating beam was optimized for a lattice constant of $1.0\,\mu m$. The resulting parameters for the objective lens system used in the simulations for Figs. 6.10 and 6.11, are given in Table B.3.

To provide an accurate prediction of the optical-intensity distribution for the experimental configuration, the Zemax Zernike fringe coefficients were obtained for a source wavelength of $363.8\,nm$ and are listed in Table B.4. These values are generally an order of magnitude larger than those given in Table B.2. This is due to the fact that the lenses were designed for a wavelength of $780\,nm$. The UV source used in the PIIES prototype resulted in the increased Zernike fringe coefficient values and provided a more accurate model for comparison to experimental results.

Table B.3: Objective lens parameters for the Greek cross and line segments in Figs. 6.10 and 6.11.

Parameter	Value
λ	$363.8\,nm$
$\mathbf{k_1}$	$2\pi/\lambda$(-0.18 -0.18 -0.97)
$\mathbf{k_2}$	$2\pi/\lambda$ (0.18 -0.18 -0.97)
$\mathbf{k_3}$	$2\pi/\lambda$ (-0.18 0.18 -0.97)
$\hat{\mathbf{e}}_1$	(-0.48 0.85 0.22)
$\hat{\mathbf{e}}_2$	(-0.26 0.96 0.07)
$\hat{\mathbf{e}}_3$	(0.94 0.23 0.25)
θ_M	$4.42\,deg$
φ_i	(45 135 -45) deg
f_2	$56.87\,mm$
CA_2	$57.73\,mm$
$\lvert m \rvert$	0.30

Table B.4: Zernike fringe coefficients for the Greek cross and line segments in Figs. 6.10 and 6.11.

Zernike Fringe Coefficient	Value (nm)
Z_1	172.86
Z_4	126.87
Z_9	384.16
Z_{16}	499.95
Z_{25}	71.16
Z_{36}	2.65
Z_{37}	1.36

REFERENCES

[1] S. R. J. Brueck, "Optical and interferometric lithography - nanotechnology enablers," *Proc. IEEE,* vol. 93, pp. 1704-1721, Oct. 2005.

[2] T. Jhaveri, A. Strojwas, L. Pileggi, and V. Rovner, "Economic assessment of lithography strategies for the 22 nm technology node," *Proc. SPIE,* vol. 7488, pp. 2Y1-2Y10, 2009.

[3] B. D. Gates, Q. Xu, M. Stewart, D. Ryan, C. G. Willson, and G. M. Whitesides, "New approaches to nanofabrication: molding, printing, and other techniques," *Chem. Rev.,* vol. 105, pp. 1171-1196, Mar. 4, 2005.

[4] S. H. Zaidi and S. R. J. Brueck, "Multiple-exposure interferometric lithography," *J. Vac. Sci. Technol. B,* vol. 11, pp. 658-666, May/June 1993.

[5] M. Rothschild, "Nanopatterning with UV optical lithography," *Mater. Res. Soc. Bull.,* vol. 30, pp. 942-946, Dec. 2005.

[6] M. C. Lemme, C. Moormann, H. Lerch, M. Moller, B. Vratzov, and H. Kurz, "Triple-gate metal-oxide-semiconductor field effect transistors fabricated with interference lithography," *Nanotechnol.,* vol. 15, pp. 208-210, Feb. 9, 2004.

[7] K.-S. Lim, M. Lee, H. Shin, and H. Kim, "Step-wise Ag thin film patterns fabricated by holographic lithography," *Thin Solid Films,* vol. 517, pp. 3273-5, Apr. 2, 2009.

[8] D. Xia, Z. Ku, S. C. Lee, and S. R. J. Brueck, "Nanostructures and functional materials fabricated by interferometric lithography," *Adv. Mater.,* vol. 23, pp. 147-179, Jan. 11, 2011.

[9] J. H. Jang, C. K. Ullal, M. Maldovan, T. Gorishnyy, S. Kooi, C. Y. Koh, and E. L. Thomas, "3D micro- and nanostructures via interference lithography," *Adv. Funct. Mater.,* vol. 17, pp. 3027-3041, Nov. 5, 2007.

[10] B. W. Smith, "Alternative optical technologies: more than curiosities?" *Proc. SPIE,* vol. 7274, pp. 21-210, 2009.

[11] J. Q. Chen, W. Jiang, X. N. Chen, L. Wang, S. S. Zhang, and R. T. Chen, "Holographic three-dimensional polymeric photonic crystals operating in the 1550 nm window," *Appl. Phys. Lett.,* vol. 90, pp. 93102-1-93102-3, Feb. 26, 2007.

[12] Y. C. Zhong, S. A. Zhu, H. M. Su, H. Z. Wang, J. M. Chen, Z. H. Zeng, and Y. L. Chen, "Photonic crystal with diamondlike structure fabricated by holographic lithography," *Appl. Phys. Lett.,* vol. 87, pp. 61103-1-61103-3, Aug. 2, 2005.

[13] X. L. Yang, L. Z. Cai, Q. Liu, and H. K. Liu, "Theoretical bandgap modeling of two-dimensional square photonic crystals fabricated by the interference of three noncoplanar laser beams," *J. Opt. Soc. Am. B,* vol. 21, pp. 1699-1702, Sept. 2004.

[14] X. L. Yang, L. Z. Cai, and Y. R. Wang, "Larger bandgaps of two-dimensional triangular photonic crystals fabricated by holographic lithography can be realized by recording geometry design," *Opt. Express,* vol. 12, pp. 5850-5856, Nov. 29, 2004.

[15] D. Y. Xia, J. Y. Zhang, X. He, and S. R. J. Brueck, "Fabrication of three-dimensional photonic crystal structures by interferometric lithography and nanoparticle self-assembly," *Appl. Phys. Lett.,* vol. 93, p. 071105, Aug. 18, 2008.

[16] C. K. Ullal, M. Maldovan, E. L. Thomas, G. Chen, Y. J. Han, and S. Yang, "Photonic crystals through holographic lithography: simple cubic, diamond-like, and gyroid-like structures," *Appl. Phys. Lett.,* vol. 84, pp. 5434-5436, June 28, 2004.

[17] J. H. Moon, A. Small, G.-R. Yi, S.-K. Lee, W.-S. Chang, D. J. Pine, and S.-M. Yang, "Patterned polymer photonic crystals using soft lithography and holographic lithography," *Synth. Met.,* vol. 148, pp. 99-102, Jan. 3, 2005.

[18] R. C. Rumpf and E. G. Johnson, "Fully three-dimensional modeling of the fabrication and behavior of photonic crystals formed by holographic lithography," *J. Opt. Soc. Am. A,* vol. 21, pp. 1703-1713, Sept. 2004.

[19] M. Campbell, D. N. Sharp, M. T. Harrison, R. G. Denning, and A. J. Turberfield, "Fabrication of photonic crystals for the visible spectrum by holographic lithography," *Nature,* vol. 404, pp. 53-56, Mar. 2, 2000.

[20] V. Berger, O. Gauthier-Lafaye, and E. Costard, "Fabrication of a 2D photonic bandgap by a holographic method," *Electron. Lett.,* vol. 33, pp. 425-426, Feb. 27, 1997.

[21] J.-H. Jang, D. Dendukuri, H. T. Alan, E. L. Thomas, and P. S. Doyle, "A route to three-dimensional structures in a microfluidic device: stop-flow interference lithography," *Angew. Chem. Int. Edit.,* vol. 46, pp. 9027-9031, Dec. 3, 2007.

[22] E. L. Hedberg-Dirk and U. A. Martinez, "Large-scale protein arrays generated with interferometric lithography for spatial control of cell-material interactions," *J. Nanomater.,* vol. 2010, pp. 1767501-1767509, May 2010.

[23] O. Akhavan, M. Abdolahad, and R. Asadi, "Storage of Ag nanoparticles in pore-arrays of SU-8 matrix for antibacterial applications," *J. Phys. D: Appl. Phys.,* vol. 42, pp. 135416-1-135416-7, June 19, 2009.

[24] F. A. Zoller, C. Padeste, Y. Ekinci, H. H. Solak, and A. Engel, "Nanostructured substrates for high density protein arrays," *Microelectron. Eng.,* vol. 85, pp. 1370-1374, May-June 2008.

[25] J. Jang, S. J. Jhaveri, B. Rasin, C. Koh, C. K. Ober, and E. L. Thomas, "Three-dimensionally-patterned submicrometer-scale hydrogel/air networks that offer a new platform for biomedical applications," *Nano Lett.,* vol. 8, pp. 1456-60, Apr. 5, 2008.

[26] E. Schonbrun, R. Piestun, P. Jordan, J. Cooper, K. D. Wulff, J. Courtial, and M. Padgett, "3D interferometric optical tweezers using a single spatial light modulator," *Opt. Express,* vol. 13, pp. 3777-3786, May 16, 2005.

[27] M. P. MacDonald, L. Paterson, K. Volke-Sepulveda, J. Arlt, W. Sibbett, and K. Dholakia, "Creation and manipulation of three-dimensional optically trapped structures," *Science,* vol. 296, pp. 1101-1103, May 10, 2002.

[28] A. E. Chiou, W. Wang, G. J. Sonek, J. Hong, and M. W. Berns, "Interferometric optical tweezers," *Opt. Commun.,* vol. 133, pp. 7-10, Jan. 1, 1997.

[29] A. Casaburi, G. Pesce, P. Zemánek, and A. Sasso, "Two- and three-beam interferometric optical tweezers," *Opt. Commun.,* vol. 251, pp. 393-404, Aug. 15, 2005.

[30] A. Jonas and P. Zemanek, "Light at work: the use of optical forces for particle manipulation, sorting, and analysis," *Electrophoresis,* vol. 29, pp. 4813-4851, Dec. 2008.

[31] M. P. MacDonald, K. Volke-Sepulveda, L. Paterson, J. Arlt, W. Sibbett, and K. Dholakia, "Revolving interference patterns for the rotation of optically trapped particles," *Opt. Commun.,* vol. 201, pp. 21-28, Jan. 1, 2002.

[32] N. I. Zheludev, "The road ahead for metamaterials," *Science,* vol. 328, pp. 582-583, Apr. 30, 2010.

[33] N. Feth, C. Enkrich, M. Wegener, and S. Linden, "Large-area magnetic metamaterials via compact interference lithography," *Opt. Express,* vol. 15, pp. 501-507, Jan. 22, 2007.

[34] Q. Li and G. P. Wang, "Tunable photonic metamaterials in the near infrared frequencies," *Opt. Express,* vol. 18, pp. 14123-14128, June 12, 2010.

[35] Y. Yang, Q. Z. Li, and G. P. Wang, "Design and fabrication of diverse metamaterial structures by holographic lithography," *Opt. Express,* vol. 16, pp. 11275-11280, July 21, 2008.

[36] V. A. Tamma, J.-H. Lee, Q. Wu, and W. Park, "Visible frequency magnetic activity in silver nanocluster metamaterial," *Appl. Opt.,* vol. 49, pp. A11-A17, Oct. 29, 2010.

[37] G. Q. Liang, W. D. Mao, H. Zou, B. C. Chen, J. F. Cao, Y. Y. Pu, X. W. Wen, and H. Z. Wang, "Holographic formation of large area split-ring arrays for magnetic metamaterials," *J. Mod. Opt.,* vol. 55, pp. 1463-1472, May 20, 2008.

[38] G. M. Burrow and T. K. Gaylord, "Multi-beam interference advances and applications: nano-electronics, photonic crystals, metamaterials, subwavelength structures, optical trapping, and biomedical structures," *Micromachines,* vol. 2, pp. 221-57, June 2011.

[39] L. Z. Cai, X. L. Yang, and Y. R. Wang, "Formation of a microfiber bundle by interference of three noncoplanar beams," *Opt. Lett.,* vol. 26, pp. 1858-60, Dec. 1, 2001.

[40] L. Z. Cai, X. L. Yang, and Y. R. Wang, "All fourteen Bravais lattices can be formed by interference of four noncoplanar beams," *Opt. Lett.,* vol. 27, pp. 900-902, June 1, 2002.

[41] A. Dwivedi, J. Xavier, J. Joseph, and K. Singh, "Formation of all fourteen Bravais lattices of three-dimensional photonic crystal structures by a dual beam multiple-exposure holographic technique," *Appl. Opt.,* vol. 47, pp. 1973-1980, Apr. 20, 2008.

[42] W. D. Mao, Y. C. Zhong, J. W. Dong, and H. Z. Wang, "Crystallography of two-dimensional photonic lattices formed by holography of three noncoplanar beams," *J. Opt. Soc. Am. B,* vol. 22, pp. 1085-1091, May 2005.

[43] D. Mei, B. Cheng, W. Hu, Z. Li, and D. Zhang, "Three-dimensional ordered patterns by light interference," *Opt. Lett.,* vol. 20, pp. 429-431, Mar. 1, 1995.

[44] Y. Ono and T. Ochi, "All fourteen Bravais lattices can be fabricated by triple exposure of two-beam interference fringes," *Proc. SPIE,* vol. 6327, pp. 632709-1-632709-8, 2006.

[45] A. I. Petsas, A. B. Coates, and G. Grynberg, "Crystallography of optical lattices," *Phys. Rev. A,* vol. 50, pp. 5173-5189, Dec. 1994.

[46] A. J. Turberfield, "Photonic crystals made by holographic lithography," *MRS Bull.,* vol. 26, pp. 632-636, Aug. 2001.

[47] L. J. Wu, Y. C. Zhong, K. S. Wong, G. P. Wang, and L. Yuan, "Fabrication of hetero-binary and honeycomb photonic crystals by one-step holographic lithography," *Appl. Phys. Lett.,* vol. 88, p. 09115, Feb. 27, 2006.

[48] X. Ao and S. He, "Two-stage design method for realization of photonic bandgap structures with desired symmetries by interference lithography," *Opt. Express,* vol. 12, pp. 978-983, Mar. 22, 2004.

[49] L. Z. Cai, X. X. Shen, X. L. Yang, G. Y. Dong, X. F. Meng, X. F. Xu, and Y. R. Wang, "Holographic design of hexagonal photonic crystals of irregular columns with large full band gap," *Opt. Commun.,* vol. 267, pp. 305-309, Nov. 15, 2006.

[50] C. W. Chien, Y. C. Lee, P. S. Lee, J. Y. Chang, and J. C. Chen, "Analysis of a two-dimensional photonic bandgap structure fabricated by an interferometric lithographic system," *Appl. Opt.,* vol. 46, pp. 3196-3204, June 1, 2007.

[51] X. X. Shen, X. L. Yang, L. Z. Cai, G. Y. Dong, X. F. Meng, X. F. Xu, and Y. R. Wang, "Negative refractions in two-dimensional photonic crystals formed by holographic lithography," *Opt. Express,* vol. 15, pp. 8003-8009, June 25, 2007.

[52] X. L. Yang, L. Z. Cai, Y. R. Wang, G. Y. Dong, X. X. Shen, X. F. Meng, and Y. Hu, "Large complete bandgaps in a two-dimensional square photonic crystal with isolated single-atom dielectric rods in air," *Nanotechnol.,* vol. 19, pp. 025201-1-025201-6, Dec. 6, 2008.

[53] X. L. Yang, L. Z. Cai, Y. R. Wang, C. S. Feng, G. Y. Dong, X. X. Shen, X. F. Meng, and Y. Hu, "Optimization of band gap of photonic crystals fabricated by holographic lithography," *Europhys. Lett.,* vol. 81, pp. 14001-1-14001-6, Jan. 2008.

[54] A. Fernandez, J. Y. Decker, S. M. Herman, D. W. Phillion, D. W. Sweeney, and M. D. Perry, "Methods for fabricating arrays of holes using interference lithography," *J. Vac. Sci. Technol. B,* vol. 15, pp. 2439-2443, Nov./Dec. 1997.

[55] L. Z. Cai, X. L. Yang, and Y. R. Wang, "Interference of three noncoplanar beams: patterns, contrast and polarization optimization," *J. Mod. Opt.,* vol. 49, pp. 1663-1672, Aug. 2002.

[56] J. L. Stay and T. K. Gaylord, "Contrast in four-beam-interference lithography," *Opt. Lett.,* vol. 33, pp. 1434-1436, July 1, 2008.

[57] X. L. Yang and L. Z. Cai, "Wave design and polarization optimization in the interference of four non-coplanar beams for making three-dimensional periodical microstructures," *J. Mod. Opt.,* vol. 50, pp. 1445-1453, June 2003.

[58] J. L. Stay and T. K. Gaylord, "Conditions for primitive-lattice-vector-direction equal contrasts in four-beam-interference lithography," *Appl. Opt.,* vol. 48, pp. 4801-4813, Aug. 20, 2009.

[59] J. L. Stay and T. K. Gaylord, "Three-beam-interference lithography: contrast and crystallography," *Appl. Opt.,* vol. 47, pp. 3221-3230, June 20, 2008.

[60] D. Chanda, L. E. Abolghasemi, and P. R. Herman, "Single laser exposure fabrication of diamond-like 3-dimensional photonic crystal microstructures using circularly polarized light," *Appl. Phys. A,* vol. 93, pp. 33-37, Oct. 2008.

[61] D. L. Brundrett, T. K. Gaylord, and E. N. Glytsis, "Polarizing mirror/absorber for visible wavelengths based on a silicon subwavelength grating: design and fabrication," *Appl. Opt.,* vol. 37, pp. 2534-2541, May 1, 1998.

[62] I. B. Divliansky, A. Shishido, I. C. Khoo, T. S. Mayer, D. Pena, S. Nishimura, C. D. Keating, and T. E. Mallouk, "Fabrication of two-dimensional photonic crystals using interference lithography and electrodeposition of CdSe," *Appl. Phys. Lett.,* vol. 79, pp. 3392-3394, Nov. 19, 2001.

[63] T. Kondo, S. Matsuo, S. Juodkazis, and H. Misawa, "Femtosecond laser interference technique with diffractive beam splitter for fabrication of three-dimensional photonic crystals," *Appl. Phys. Lett.,* vol. 79, pp. 725-727, Aug. 6, 2001.

[64] N. D. Lai, W. P. Liang, J. H. Lin, and C. C. Hsu, "Rapid fabrication of large-area periodic structures containing well-defined defects by combining holography and mask techniques," *Opt. Express,* vol. 13, pp. 5331-5337, July 11, 2005.

[65] N. D. Lai, W. P. Liang, J. H. Lin, C. C. Hsu, and C. H. Lin, "Fabrication of two- and three-dimensional periodic structures by multi-exposure of two-beam interference technique," *Opt. Express,* vol. 13, pp. 9605-9611, Nov. 14, 2005.

[66] Y. Lin, D. Rivera, and K. P. Chen, "Woodpile-type photonic crystals with orthorhombic or tetragonal symmetry formed through phase mask techniques," *Opt. Express,* vol. 14, pp. 887-892, Jan. 23, 2006.

[67] Y. K. Lin, A. Harb, K. Lozano, D. Xu, and K. P. Chen, "Five beam holographic lithography for simultaneous fabrication of three dimensional photonic crystal templates and line defects using phase tunable diffractive optical element," *Opt. Express,* vol. 17, pp. 16625-16631, Sept. 14, 2009.

[68] T. A. Savas, S. N. Shah, M. L. Schattenburg, J. M. Carter, and H. I. Smith, "Achromatic interferometric lithography for 100-nm-period gratings and grids," *J. Vac. Sci. Technol. B,* vol. 13, pp. 2732-2735, Nov./Dec. 1995.

[69] J. L. Stay, G. M. Burrow, and T. K. Gaylord, "Three-beam interference lithography methodology," *Rev. Sci. Instrum.,* vol. 82, pp. 231151-231158, Feb. 24, 2011.

[70] L. Wu, Y. Zhong, C. T. Chan, K. S. Wong, and G. P. Wang, "Fabrication of large area two- and three-dimensional polymer photonic crystals using single refracting prism holographic lithography," *Appl. Phys. Lett.,* vol. 86, p. 241102, June 7, 2005.

[71] J. L. Stay, G. M. Burrow, and T. K. Gaylord, "Three-beam interference lithography methodology," *Virtual J. Biol. Phys. Res.,* vol. 21, pp. 23115-8, Feb. 24, 2011.

[72] G. M. Burrow and T. K. Gaylord, "Interference projection exposure system," in *Frontiers in Optics,* San Jose, CA, FWZ2, Oct. 19, 2011.

[73] G. M. Burrow and T. K. Gaylord, "Apparatus and method for photolithographic projection exposure for fabrication of one-, two-, and three-dimensional periodic structures with or without integrated patterns," U. S. Patent Application No. 13/249,841, filed Sept. 30, 2011.

[74] G. M. Burrow and T. K. Gaylord, "Diffractive photo-mask for production of non-periodic functional elements integrated within periodic lattices and method for making the same," U. S. Patent Application no. 13/250,011, filed Sept. 30, 2011.

[75] G. M. Burrow, M. C. R. Leibovici, and T. K. Gaylord, "Pattern-integrated interference lithography: single-exposure fabrication of photonic-crystal structures," *Appl. Opt.,* (accepted).

[76] G. M. Burrow, M. C. R. Leibovici, J. W. Kummer, and T. K. Gaylord, "Pattern-integrated interference lithpgraphy instrumentation," *Rev. Sci. Instrum.,* (in prepration).

[77] G. M. Burrow and T. K. Gaylord, "Constrained parametric optimization of point geometries in multi-beam-interference lithography," in *Frontiers in Optics,* Rochester, NY, FWS3, Oct. 27, 2010.

[78] G. M. Burrow and T. K. Gaylord, "Design of motif geometries in multi-beam interference," *Opt. Lett.,* (in preparation).

[79] G. M. Burrow and T. K. Gaylord, "Parametric constraints in multi-beam interference," *J. Micro/Nanolithogr. MEMS MOEMS,* (submitted).

[80] J. D. Cressler, *Silicon Earth: Introduction to the Microelectronics and Nanotechnology Revolution*. New York: Cambridge University Press, 2009.

[81] B. E. A. Saleh and M. C. Teich, *Fundamentals of Photonics*. New York: John Wiley & Sons, INC., 1991.

[82] J. L. Stay, *Multi-Beam-Interference-Based Methodology for the Fabrication of Photonic Crystal Structures.* PhD thesis, Georgia Institute of Technology, Atlanta, GA, Oct., 2009.

[83] H. H. Solak, "Space-invariant multiple-beam achromatic EUV interference lithography," *Microelectron. Eng.,* vol. 78-79, pp. 410-416, Mar. 2005.

[84] A. Jimenez-Ceniceros, M. Trejo-Duran, E. Alvarado-Mendez, and V. M. Castano, "Extinction zones and scalability in N-beam interference lattices," *Opt. Commun.,* vol. 283, pp. 362-367, Feb. 1, 2010.

[85] W. D. Mao, J. W. Dong, Y. C. Zhong, G. Q. Liang, and H. Z. Wang, "Formation principles of two-dimensional compound photonic lattices by one-step holographic lithography," *Opt. Express,* vol. 13, pp. 2994-2999, Apr. 18, 2005.

[86] T. Y. M. Chan, O. Toader, and S. John, "Photonic band gap templating using optical interference lithography," *Phys. Rev. E,* vol. 71, pp. 46605-1-46605-18, Apr. 2005.

[87] E. R. Dedman, D. N. Sharp, A. J. Turberfield, C. F. Blanford, and R. G. Denning, "Photonic crystals with a chiral basis by holographic lithography," *Photonics Nanostruct.,* vol. 3, pp. 79-83, Dec. 2005.

[88] N. D. Lai, J. H. Lin, and C. C. Hsu, "Fabrication of highly rotational symmetric quasi-periodic structures by multiexposure of a three-beam interference technique," *Appl. Opt.,* vol. 46, pp. 5645-5648, Aug. 10, 2007.

[89] S. Juodkazis, V. Mizeikis, and H. Misawa, "Three-dimensional microfabrication of materials by femtosecond lasers for photonics applications," *J. Appl. Phys.,* vol. 106, pp. 51101-1-51101-14, Sept. 11, 2009.

[90] R. P. Zaccaria, S. Shoji, H. B. Sun, and S. Kawata, "Multi-shot interference approach for any kind of Bravais lattice," *Appl. Phys. B,* vol. 93, pp. 251-256, Oct. 2008.

[91] W. Y. Tam, "Icosahedral quasicrystals by optical interference holography," *Appl. Phys. Lett.,* vol. 89, p. 251111, Dec. 18, 2006.

[92] C. K. Ullal, M. Maldovan, M. Wohlgemuth, E. L. Thomas, C. A. White, and S. Yang, "Triply periodic bicontinuous structures through interference lithography: a level-set approach," *J. Opt. Soc. Am. A,* vol. 20, pp. 948-54, May 2003.

[93] J. H. Moon, D. J. Pine, and S.-M. Yang, "Fabrication of two-dimensional photonic crystals of non-spherical atoms by holographic lithography," *Proc. SPIE,* vol. 5450, pp. 95-99, 2004.

[94] F. Quinonez, J. W. Menezes, L. Cescato, V. F. Rodriguez-Esquerre, H. Hernandez-Figueroa, and R. D. Mansano, "Band gap of hexagonal 2D photonic crystals with elliptical holes recorded by interference lithography," *Opt. Express,* vol. 14, pp. 4873-4879, May 26, 2006.

[95] Y. Hung, Jr., S.-L. Lee, and Y.-T. Pan, "Photonic bandgap analysis of photonic crystal slabs with elliptical holes and their formation with laser holography," *J. Opt.,* vol. 12, pp. 15102-1-15102-8, Nov. 24, 2010.

[96] D. Chanda, L. Abolghasemi, and P. R. Herman, "Numerical band calculation of holographically formed periodic structures with irregular motif," *Proc. SPIE,* vol. 6128, pp. 61281E-1-61281E-6, 2006.

[97] M. Qiu and S. He, "Optimal design of a two-dimensional photonic crystal of square lattice with a large complete two-dimensional bandgap," *J. Opt. Soc. Am. B,* vol. 17, pp. 1027-1030, June 2000.

[98] L. M. Qi, Z. Q. Yang, X. Gao, W. X. Liu, and Z. Liang, "Research on three types of rhombus lattice photonic band structures," *J. Electromagn. Waves Appl.,* vol. 22, pp. 1155-1164, Aug. 2008.

[99] Y.-Y. Pu, G.-Q. Liang, W.-D. Mao, J.-W. Dong, and H.-Z. Wang, "Fabrication of two-dimensional photonic crystals with triangular rods by single-exposure holographic lithography," *Chin. Phys. Lett.,* vol. 24, pp. 983-985, Apr. 4, 2007.

[100] L. Z. Cai, G. Y. Dong, C. S. Feng, X. L. Yang, X. X. Shen, and X. F. Meng, "Holographic design of a two-dimensional photonic crystal of square lattice with a large two-dimensional complete bandgap," *J. Opt. Soc. Am. B,* vol. 23, pp. 1708-1711, Aug. 2006.

[101] R. Wang, X.-H. Wang, B.-Y. Gu, and G.-Z. Yang, "Effects of shapes and orientations of scatterers and lattice symmetries on the photonic band gap in two-dimensional photonic crystals," *J. Appl. Phys.,* vol. 90, pp. 4307-4313, Nov. 1, 2001.

[102] K. Ohlinger, Y. K. Lin, and J. S. Qualls, "Maximum and overlapped photonic band gaps in both transverse electric and transverse magnetic polarizations in two-dimensional photonic crystals with low symmetry," *J. Appl. Phys.,* vol. 106, pp. 63520-1-63520-4, Sept. 23, 2009.

[103] Z.-Y. Li, J. Wang, and B. Y. Gu, "Full band gap in fcc and bcc photonic band gaps structure: non-spherical atom," *J. Phys. Soc. Jpn.,* vol. 67, pp. 3288-3291, Sept. 1998.

[104] H. K. Kang, K. H. Lee, C. C. Wong, and F. Romanato, "ID to 2D transitional structure of plasmonic crystals: fabrication and characterization," *Appl. Phys. B,* vol. 97, pp. 671-677, Oct. 6, 2009.

[105] S. Noda, "Photonic crystal lasers-ultimate nanolasers and broad-area coherent lasers," *J. Opt. Soc. Am. B,* vol. 27, pp. B1-B8, Nov. 2010.

[106] S. Noda, M. Yokoyama, M. Imada, A. Chutinan, and M. Mochizuki, "Polarization mode control of two-dimensional photonic crystal laser by unit cell structure design," *Science,* vol. 293, pp. 1123-1125, Aug. 10, 2001.

[107] B. Hu, M. Lu, W. Li, K. Zou, Z. Zhou, A. Lin, and N. Li, "High birefringent rhombic-hole photonic crystal fibers," *Appl. Opt.,* vol. 49, pp. 6098-6101, Nov. 1, 2010.

[108] J. Huang, S. Beckemper, A. Gillner, and K. Wang, "Tunable surface texturing by polarization-controlled three-beam interference," *J. Micromech. Microeng.,* vol. 20, pp. 95004-1-95004-7, Aug. 5, 2010.

[109] P. Vavassori, O. Donzelli, V. Metlushko, M. Grimsditch, B. Ilic, P. Neuzil, and R. Kumar, "Magnetic switching in submicron-scale periodic magnetic arrays," *J. Appl. Phys.,* vol. 88, pp. 999-1003, July 15, 2000.

[110] Z. X. Tang, R. W. Peng, D. Y. Fan, S. C. Wen, H. Zhang, and L. J. Qian, "Absolute left-handed behaviors in a triangular elliptical-rod photonic crystal," *Opt. Express,* vol. 13, pp. 9796-9803, Nov. 28, 2005.

[111] D. B. Do, N. D. Lai, C. Y. Wu, J. H. Lin, and C. C. Hsu, "Fabrication of ellipticity-controlled microlens arrays by controlling the parameters of the multiple-exposure two-beam interference technique," *Appl. Opt.,* vol. 50, pp. 579-585, Feb. 1, 2011.

[112] J. W. Menezes and L. Cescato, "Recording different geometries of 2D hexagonal photonic crystals by choosing the phase between two-beam interference exposures," *Opt. Express,* vol. 14, pp. 8578-8583, Sept.18, 2006.

[113] X. L. Yang, L. Z. Cai, and Q. Liu, "Polarization optimization in the interference of four umbrellalike symmetric beams for making three-dimensional periodic microstructures," *Appl. Opt.,* vol. 41, pp. 6894-6900, Nov. 10, 2002.

[114] H. M. Su, Y. C. Zhong, X. Wang, X. G. Zheng, J. F. Xu, and H. Z. Wang, "Effects of polarization on laser holography for microstructure fabrication," *Phys. Rev. E,* vol. 67, pp. 56619-1-56619-6, May 21, 2003.

[115] A. Fernandez and D. W. Phillion, "Effects of phase shifts on four-beam interference patterns," *Appl. Opt.,* vol. 37, pp. 473-478, Jan. 20, 1998.

[116] M. Ellman, A. Rodriguez, N. Perez, M. Echeverria, Y. K. Verevkin, C. S. Peng, T. Berthou, Z. Wang, S. M. Olaizola, and I. Ayerdi, "High-power laser interference lithography process on photoresist: effect of laser fluence and polarisation," *Appl. Surf. Sci.,* vol. 255, pp. 5537-5541, Aug. 12, 2009.

[117] D. C. Meisel, M. Wegener, and K. Busch, "Three-dimensional photonic crystals by holographic lithography using the umbrella configuration: symmetries and complete photonic band gaps," *Phys. Rev. B,* vol. 70, pp. 165104-1-165104-10, Oct. 2004.

[118] L. Z. Cai and X. L. Yang, "Interference of circularly polarized light: contrast and application in fabrication of three-dimensional periodic microstructures," *Opt. Laser Technol.,* vol. 34, pp. 671-674, Nov. 2002.

[119] X. L. Yang and L. Z. Cai, "Wave design of the interference of three noncoplanar beams for microfiber fabrication," *Opt. Commun.,* vol. 208, pp. 293-297, July 15, 2002.

[120] X. L. Yang, L. Z. Cai, Y. R. Wang, and Q. Liu, "Interference of four umbrellalike beams by a diffractive beam splitter for fabrication of two-dimensional square and trigonal lattices," *Opt. Lett.,* vol. 28, pp. 453-455, Mar. 15, 2003.

[121] M. Salaun, M. Audier, M. Duneau, and F. Delyon, "Holographic lithography of a two-dimensional hexagonal structure: effect of beam polarization," *Appl. Surf. Sci.,* vol. 254, pp. 850-854, Aug. 6, 2007.

[122] A. F. Lasagni, Y. Dajun, and S. Das, "Layer-by-layer interference lithography of three-dimensional microstructures in SU-8," *Adv. Eng. Mater.,* vol. 11, pp. 408-11, May 2009.

[123] L. Pang, W. Nakagawa, and Y. Fainman, "Fabrication of two-dimensional photonic crystals with controlled defects by use of multiple exposures and direct write," *Appl. Opt.,* vol. 42, pp. 5450-5456, Sept. 20, 2003.

[124] G. S. Pati, R. K. Heilmann, P. T. Konkola, C. Joo, C. G. Chen, E. Murphy, and M. L. Schattenburg, "Generalized scanning beam interference lithography system for patterning gratings with variable period progressions," *J. Vac. Sci. Technol. B,* vol. 20, pp. 2617-2621, Nov./Dec. 2002.

[125] L. E. Gutierrez-Rivera and L. Cescato, "SU-8 submicrometric sieves recorded by UV interference lithography," *J. Micromech. Microeng.,* vol. 18, pp. 115003-1-115003-7, Sept. 19, 2008.

[126] R. C. Gauthier and K. W. Mnaymneh, "Design of photonic band gap structures through a dual-beam multiple exposure technique," *Opt. Laser Technol.,* vol. 36, pp. 625-633, Nov. 2004.

[127] C. Moormann, J. Bolten, and H. Kurz, "Spatial phase-locked combination lithography for photonic crystal devices," *Microelectron. Eng.,* vol. 73-74, pp. 417-422, Sept. 2004.

[128] F. Y. Lee, K. H. Fung, T. L. Tang, W. Y. Tam, and C. T. Chan, "Fabrication of gold nano-particle arrays using two-dimensional templates from holographic lithography," *Curr. Appl. Phys.,* vol. 9, pp. 820-5, July 2009.

[129] P. N. Dyachenko, S. V. Karpeev, E. V. Fesik, Y. V. Miklyaev, V. S. Pavelyev, and G. D. Malchikov, "The three-dimensional photonic crystals coated by gold nanoparticles," *Opt. Commun.,* vol. 284, pp. 885-888, Feb. 1, 2011.

[130] B. D. MacLeod, A. F. Kelsey, M. A. Leclerc, D. P. Resler, S. Liberman, and J. P. Nole, "Fully automated interference lithography," *Proc. SPIE,* vol. 4688, pp. 910-921, 2002.

[131] A. Rodriguez, M. Echeverria, M. Ellman, N. Perez, Y. K. Verevkin, C. S. Peng, T. Berthou, W. Zuobin, I. Ayerdi, J. Savall, and S. M. Olaizola, "Laser interference lithography for nanoscale structuring of materials: from laboratory to industry," *Microelectron. Eng.,* vol. 86, pp. 937-940, Apr.-June 2009.

[132] C. Lu, X. K. Hu, S. S. Dimov, and R. H. Lipson, "Controlling large-scale film morphology by phase manipulation in interference lithography," *Appl. Opt.,* vol. 46, pp. 7202-7206, Oct. 10, 2007.

[133] X. S. Xie, M. Li, J. Guo, B. Liang, Z. X. Wang, A. Sinitskii, Y. Xiang, and J. Y. Zhou, "Phase manipulated multi-beam holographic lithography for tunable optical lattices," *Opt. Express,* vol. 15, pp. 7032-7037, May 28, 2007.

[134] S. Pissadakis and C. Pappas, "Planar periodic structures fabricated in Er/Yb-codoped phosphate glass using multi-beam ultraviolet laser holography," *Opt. Express,* vol. 15, pp. 4296-4303, Apr. 2, 2007.

[135] Z. H. Levine, S. Grantham, and T. B. Lucatorto, "Design considerations for a cascaded grating interferometer suitable for extreme ultraviolet interference lithography," *J. Microlith. Microfab. Microsys.,* vol. 8, pp. 21202-1-21202-8, Apr.-June 2009.

[136] J. H. Klein-Wiele and P. Simon, "Fabrication of periodic nanostructures by phase-controlled multiple-beam interference," *Appl. Phys. Lett.,* vol. 83, pp. 4707-4709, Dec. 8, 2003.

[137] L. Z. Cai, X. L. Yang, Q. Liu, and Y. R. Wang, "What kind of Bravais lattices can be made by the interference of four umbrellalike beams?" *Opt. Commun.,* vol. 224, pp. 243-246, Sept. 1, 2003.

[138] X. L. Yang, L. Z. Cai, Y. R. Wang, and Q. Liu, "Interference technique by three equal-intensity umbrellalike beams with a diffractive beam splitter for fabrication of two-dimensional trigonal and square lattices," *Opt. Commun.,* vol. 218, pp. 325-332, Apr. 1, 2003.

[139] W. Y. Tam, "Woodpile and diamond structures by optical interference holography," *J. Opt. A: Pure Appl. Opt.,* vol. 9, pp. 1076-1081, Nov. 2007.

[140] G. Y. Dong, L. Z. Cai, X. L. Yang, X. X. Shen, X. F. Meng, X. F. Xu, and Y. R. Wang, "Holographic design and band gap evolution of photonic crystals formed with five-beam symmetric umbrella configuration," *Opt. Express,* vol. 14, pp. 8096-8102, Sept. 4, 2006.

[141] Y. K. Pang, J. C. W. Lee, C. T. Ho, and W. Y. Tam, "Realization of woodpile structure using optical interference holography," *Opt. Express,* vol. 14, pp. 9113-9119, Oct. 2, 2006.

[142] X. Mai, R. Moshrefzadeh, U. J. Gibson, G. I. Stegeman, and C. T. Seaton, "Simple versatile method for fabricating guided-wave gratings," *Appl. Opt.,* vol. 24, pp. 3155-3161, Oct. 1, 1985.

[143] Y. Guan and A. J. Pedraza, "Synthesis and characterization of self-organized nanostructure arrays generated by laser irradiation," *Mat. Res. Soc. Symp. Proc.,* vol. 818, pp. 335-340, Apr. 2004.

[144] J. de Boor, N. Geyer, U. Gosele, and V. Schmidt, "Three-beam interference lithography: upgrading a Lloyd's interferometer for single-exposure hexagonal patterning," *Opt. Lett.,* vol. 34, pp. 1783-1785, June 15, 2009.

[145] J. de Boor, K. Dong Sik, and V. Schmidt, "Sub-50 nm patterning by immersion interference lithography using a Littrow prism as a Lloyd's interferometer," *Opt. Lett.,* vol. 35, pp. 3450-3452, Oct. 15, 2010.

[146] N. H. Rizvi and M. C. Gower, "Production of submicrometer period Bragg gratings in optical fibers using wavefront division with a biprism and an excimer laser source," *Appl. Phys. Lett.,* vol. 67, pp. 739-741, June 8, 1995.

[147] W. Xiang, J. Liang, G. Zhang, L. Wu, K. S. Wong, and G. K. L. Wong, "Non-coplanar multi-beam interference produced by one triangular pyramid for fabricating photonic crystals," *Chin. Opt. Lett.,* vol. 3, pp. 712-714, Dec. 10, 2005.

[148] Y. C. Zhong, L. J. Wu, H. M. Su, K. S. Wong, and H. Z. Wang, "Fabrication of photonic crystals with tunable surface orientation by holographic lithography," *Opt. Express,* vol. 14, pp. 6837-6843, July 24, 2006.

[149] M. Lei, B. Yao, and R. A. Rupp, "Structuring by multi-beam interference using symmetric pyramids," *Opt. Express,* vol. 14, pp. 5803-5811, June 12, 2006.

[150] Y. V. Miklyaev, D. C. Meisel, A. Blanco, G. von Freymann, K. Busch, W. Koch, C. Enkrich, M. Deubel, and M. Wegener, "Three-dimensional face-centered-cubic photonic crystal templates by laser holography: fabrication, optical

characterization, and band-structure calculations," *Appl. Phys. Lett.,* vol. 82, pp. 1284-1286, Feb. 24, 2003.

[151] C. H. Lin, Z. H. Zhu, and Y. H. Lo, "New grating fabrication technology for optoelectronic devices: cascaded self-induced holography," *Appl. Phys. Lett.,* vol. 67, pp. 3072-3074, Sept. 13, 1995.

[152] V. Berger, O. Gauthier-Lafaye, and E. Costard, "Photonic band gaps and holography," *J. Appl. Phys.,* vol. 82, pp. 60-64, July 1, 1997.

[153] Y. Lin and P. R. Herman, "Effect of structural variation on the photonic band gap in woodpile photonic crystal with body-centered-cubic symmetry," *J. Appl. Phys.,* vol. 98, pp. 63104-1-63104-4, Sept. 27, 2005.

[154] G. J. Schneider, E. D. Wetzel, J. A. Murakowski, and D. W. Prather, "Fabrication of three-dimensional "Yablonovite" photonic crystals by multiple-exposure UV interference lithography," *Proc. SPIE,* vol. 5720, pp. 9-17, 2004.

[155] A. Chelnokov, S. Rowson, J. M. Lourtioz, V. Berger, and J. Y. Courtois, "An optical drill for the fabrication of photonic crystals," *J. Opt. A: Pure Appl. Opt.,* vol. 1, pp. 3-6, Sept. 1999.

[156] I. Divliansky, T. S. Mayer, K. S. Holliday, and V. H. Crespi, "Fabrication of three-dimensional polymer photonic crystal structures using single diffraction element interference lithography," *Appl. Phys. Lett.,* vol. 82, pp. 1667-1669, Mar. 17, 2003.

[157] M. Okai, S. Tsuji, N. Chinone, and T. Harada, "Novel method to fabricate corrugation for a λ/4-shifted distributed feedback laser using a grating photomask," *Appl. Phys. Lett.,* vol. 55, pp. 415-417, May 16, 1989.

[158] S. Jeon, J. Park, R. Cirelli, S. Yang, C. Heitzman, P. Braun, P. Kenis, and J. Rogers, "Fabricating complex three-dimensional nanostructures with high-resolution conformable phase masks," *PNAS,* vol. 101, pp. 12428-12433, Aug. 24, 2004.

[159] Y. Lin, P. R. Herman, and E. L. Abolghasemi, "Proposed single-exposure holographic fabrication of microsphere-type photonic crystals through phase-mask techniques," *J. Appl. Phys.,* vol. 97, pp. 96102-1-96102-3, Apr. 14, 2005.

[160] Y. Lin, P. R. Herman, and K. Darmawikarta, "Design and holographic fabrication of tetragonal and cubic photonic crystals with phase mask: toward the mass-production of three-dimensional photonic crystals," *Appl. Phys. Lett.,* vol. 86, p. 071117, Feb. 10, 2005.

[161] K. O. Hill, B. Malo, F. Bilodeau, D. C. Johnson, and J. Albert, "Bragg gratings fabricated in monomode photosensitive optical fiber by UV exposure through a phase mask," *Appl. Phys. Lett.,* vol. 62, pp. 1035-1037, Jan. 5, 1993.

[162] D. Chanda, L. Abolghasemi, and P. R. Herman, "One-dimensional diffractive optical element based fabrication and spectral characterization of three-dimensional photonic crystal templates," *Opt. Express,* vol. 14, pp. 8568-8577, Sept. 18, 2006.

[163] T. Y. M. Chan, O. Toader, and S. John, "Photonic band-gap formation by optical-phase-mask lithography," *Phys. Rev. E,* vol. 73, pp. 46610-1-46610-11, Apr. 26, 2006.

[164] D. Chanda and P. R. Herman, "Two-dimensional diffractive optical element based fabrication of 3D photonic crystal templates," *Proc. SPIE,* vol. 6480, pp. 64800Q-1-64800Q-5, 2007.

[165] Y. Lin, A. Harb, D. Rodriguez, K. Lozano, D. Xu, and K. P. Chen, "Holographic fabrication of photonic crystals using multidimensional phase masks," *J. Appl. Phys.,* vol. 104, pp. 113111-1-113111-6, Dec. 4, 2008.

[166] G. Zhou and F. S. Chau, "Three-dimensional photonic crystal by holographic contact lithography using a single diffraction mask," *Appl. Phys. Lett.,* vol. 90, pp. 181106-1-181106-3, Apr. 30, 2007.

[167] X. Di, K. P. Chen, K. Ohlinger, and Y. Lin, "Holographic fabrication of diamondlike photonic crystal template using two-dimensional diffractive optical elements," *Appl. Phys. Lett.,* vol. 93, pp. 31101-1-31101-3, July 21, 2008.

[168] M. C. George, E. C. Nelson, J. A. Rogers, and P. V. Braun, "Direct fabrication of 3D periodic inorganic microstructures using conformal phase masks," *Angew. Chem. Int. Edit.,* vol. 48, pp. 144-148, Dec. 17, 2008.

[169] D. Chanda, N. Zachari, M. Haque, M. L. Ng, and P. R. Herman, "Flexible fabrication of three-dimensional optical-domain photonic crystals using a combination of single-laser-exposure diffractive-optics lithography and template inversion," *Opt. Lett.,* vol. 34, pp. 3920-3922, Dec. 15, 2009.

[170] I. Divliansky and T. S. Mayer, "Three-dimensional low-index-contrast photonic crystals fabricated using a tunable beam splitter," *Nanotechnol.,* vol. 17, pp. 1241-1-1241-5, Feb. 17, 2006.

[171] J. Xu, R. Ma, X. Wang, and W. Y. Tam, "Icosahedral quasicrystals for visible wavelengths by optical interference holography," *Opt. Express,* vol. 15, pp. 4287-4295, Apr. 2, 2007.

[172] J. L. Horner, "Additional property of interferometer symmetry," *Appl. Opt.,* vol. 17, pp. 505-505, Feb. 15, 1978.

[173] M. L. Dakss, L. Kuhn, P. F. Heidrich, and B. A. Scott, "Grating coupler for efficient excitation of optical guided waves in thin films," *Appl. Phys. Lett.,* vol. 16, pp. 523-525, June 15, 1970.

[174] T. Kondo, S. Juodkazis, and H. Misawa, "Reduction of capillary force for high-aspect ratio nanofabrication," *Appl. Phys. A,* vol. A81, pp. 1583-1586, Sept. 13, 2005.

[175] J. Amako, D. Sawaki, and M. Kato, "Fringe-shifting interferometric laser lithography with optical nonlinearity for micro- and nanofabrications," *Appl. Phys. Lett.,* vol. 91, pp. 54105-1-54105-3, July 31, 2007.

[176] A. Lasagni, Y. Dajun, S. Peng, and S. Das, "Rapid fabrication of biocompatible hydrogels microdevices using laser interference lithography," *Proc. SPIE,* vol. 7365, pp. 73650I-1-73650I-9, 2009.

[177] Y. Zhong, J. Zhou, and K. S. Wong, "Two-photon fabrication of photonic crystals by single-beam laser holographic lithography," *J. Appl. Phys.,* vol. 107, pp. 74311-1-74311-4, Apr. 14, 2010.

[178] Y. Yang and G. P. Wang, "Realization of periodic and quasiperiodic microstructures with sub-diffraction-limit feature sizes by far-field holographic lithography," *Appl. Phys. Lett.,* vol. 89, pp. 111104-1-111104-3, Sept. 11, 2006.

[179] T.-F. Zhu, B.-H. Tan, X.-F. Pan, and W.-D. Tao, "Fabrication of two-and three-dimensional periodic submicron structures by holographic lithography with a 635 nm laser and matched photopolymer," *Chin. Phys. B,* vol. 19, pp. 14218-1-14218-6, Jan. 2010.

[180] A. Arsh, M. Klebanov, V. Lyubin, L. Shapiro, A. Feigel, M. Veinger, and B. Sfez, "Glassy $mAs_2S_3nAs_2Se_3$ photoresist films for interference laser lithography," *Opt. Mater.,* vol. 26, pp. 301-304, Mar. 5, 2004.

[181] X. Wang, H. Su, L. Zhang, Y. He, X. Zheng, and H. Wang, "Fabrication of a submicrometer crystalline structure by thermoplastic holography," *Appl. Opt.,* vol. 40, pp. 5588-5591, Nov. 1, 2001.

[182] S. Yang, M. Megens, J. Aizenberg, P. Wiltzius, P. M. Chaikin, and W. B. Russel, "Creating periodic three-dimensional structures by multibeam interference of visible laser," *Chem. Mater.,* vol. 14, pp. 2831-2833, July 2002.

[183] C. Aydin, A. Zaslavsky, G. J. Sonek, and J. Goldstein, "Reduction of reflection losses in $ZnGeP_2$ using motheye antireflection surface relief structures," *Appl. Phys. Lett.,* vol. 80, pp. 2242-2244, Apr. 1, 2002.

[184] T. Liu, M. Fallahi, J. V. Moloney, and M. Mansuripur, "Fabrication of two-dimensional photonic crystals with embedded defects using blue-laser-writer and optical holography," *IEEE Phot. Tech. Lett.,* vol. 18, pp. 1100-1102, May 1, 2006.

[185] C. W. J. Berendsen, M. Skeren, D. Najdek, and F. Cerny, "Superhydrophobic surface structures in thermoplastic polymers by interference lithography and thermal imprinting," *Appl. Surf. Sci.,* vol. 255, pp. 9305-9310, July 8, 2009.

[186] C. P. Fucetola, H. Korre, and K. K. Berggren, "Low-cost interference lithography," *J. Vac. Sci. Technol. B,* vol. 27, pp. 2958-2961, Nov./Dec. 2009.

[187] T. J. Suleski, B. Baggett, W. F. Delaney, C. Koehler, and E. G. Johnson, "Fabrication of high-spatial-frequency gratings through computer-generated near-field holography," *Opt. Lett.,* vol. 24, pp. 602-604, May 1, 1999.

[188] R. M. de Ridder, C. G. Bostan, H. A. G. M. van Wolferen, I. van Dorssen, L. Vogelaar, F. B. Segerink, L. Kuipers, and N. F. van Hulst, "Fabrication of photonic crystal slabs and defects using laser interference lithography and focused ion beam-assisted deposition," *Proceedings of the 4th International Conference on Transparent Optical Networks,* vol. 2, pp. 14-19, Apr. 2002.

[189] X. Chen, S. H. Zaidi, S. R. J. Brueck, and D. J. Devine, "Interferometric lithography of sub-micrometer sparse hole arrays for field-emission display applications," *J. Vac. Sci. Technol. B,* vol. 14, pp. 3339-3349, Sept./Oct. 1996.

[190] C. S. Peng and C. Tan, "Fast, high efficiency and cost-effective laser nano-lithography," *Proc. SPIE,* vol. 7657, pp. 765708-765712, 2010.

[191] S. Ura, M. Hamada, J. Ohmori, K. Nishio, and K. Kintaka, "Free-space-wave drop demultiplexing waveguide device fabricated by use of the interference exposure method," *Appl. Opt.,* vol. 45, pp. 22-26, Jan. 1, 2006.

[192] M. Fritze, T. M. Bloomstein, B. Tyrrell, T. H. Fedynyshyn, N. N. Efremow Jr, D. E. Hardy, S. Cann, D. Lennon, S. Spector, M. Rothschild, and P. Brooker, "Hybrid optical maskless lithography: scaling beyond the 45 nm node," *J. Vac. Sci. Technol. B,* vol. 23, pp. 2743-2748, Nov./Dec. 2005.

[193] M. G. Capeluto, G. Vaschenko, M. Grisham, M. C. Marconi, S. Luduena, L. Pietrasanta, L. Yunfeng, B. Parkinson, C. S. Menoni, and J. J. Rocca, "Nanopatterning with interferometric lithography using a compact λ = 46.9-nm laser," *IEEE Nanotechnol.,* vol. 5, pp. 3-7, Jan. 2006.

[194] A. Ritucci, A. Reale, P. Zuppella, L. Reale, P. Tucceri, G. Tomassetti, P. Bettotti, and L. Pavesi, "Interference lithography by a soft X-ray laser beam: nanopatterning on photoresists," *J. Appl. Phys.,* vol. 102, pp. 34313-1-34313-4, Aug. 14, 2007.

[195] H. H. Solak, D. He, W. Li, S. Singh-Gasson, F. Cerrina, B. H. Sohn, X. M. Yang, and P. Nealey, "Exposure of 38 nm period grating patterns with extreme ultraviolet interferometric lithography," *Appl. Phys. Lett.,* vol. 75, pp. 2328-2330, Aug. 18, 1999.

[196] A. Isoyan, Y. C. Cheng, F. Jiang, J. Wallace, F. Cerrina, and S. Bollepalli, "Progress in extreme ultraviolet interferometric and holographic lithography," *J. Vac. Sci. Technol. B,* vol. 25, pp. 2145-2150, Nvo./Dec. 2007.

[197] K. V. Sreekanth, J. K. Chua, and V. M. Murukeshan, "Interferometric lithography for nanoscale feature patterning: a comparative analysis between laser interference, evanescent wave interference, and surface plasmon interference," *Appl. Opt.,* vol. 49, pp. 6710-6717, Dec. 10, 2010.

[198] R. Luttge, "Massively parallel fabrication of repetitive nanostructures: nanolithography for nanoarrays," *J. Phys. D: Appl. Phys.,* vol. 42, pp. 123001-1-123001-18, June 5, 2009.

[199] H. I. Smith, "Low cost nanolithography with nanoaccuracy," *Rutherford Memorial Workshop on Semiconductor Nanostructures,* pp. 104-109, Feb. 2001.

[200] C. H. Liu, M. H. Hong, M. C. Lum, H. Flotow, F. Ghadessy, and J. B. Zhang, "Large-area micro/nanostructures fabrication in quartz by laser interference lithography and dry etching," *Appl. Phys. A,* vol. 101, pp. 237-241, June 10, 2010.

[201] M. Salaun, M. Audier, F. Delyon, and M. Duneau, "3-D holographic lithography of organic-inorganic hybrids," *Appl. Surf. Sci.,* vol. 254, pp. 830-835, Aug. 19, 2007.

[202] K. Saravanamuttu, C. F. Blanford, D. N. Sharp, E. R. Dedman, A. J. Turberfield, and R. G. Denning, "Sol−gel organic−inorganic composites for 3-D holographic lithography of photonic crystals with submicron periodicity," *Chem. Mater.,* vol. 15, pp. 2301-2304, June 17, 2003.

[203] R. Gronheid and M. J. Leeson, "Extreme ultraviolet interference lithography as applied to photoresist studies," *J. Microlith. Microfab. Microsys.,* vol. 8, pp. 21205-1-21205-10, Apr.-June 2009.

[204] Y. J. Liu and X. W. Sun, "Electrically tunable two-dimensional holographic photonic crystal fabricated by a single diffractive element," *Appl. Phys. Lett.,* vol. 89, p. 171101, Oct. 23, 2006.

[205] J. Teteris, "Immersion holography based on amorphous chalcogenide films," *J. Mater. Sci. - Mater. Electron.,* vol. 20, pp. 149-152, Dec. 5, 2009.

[206] A. Shishido, I. B. Diviliansky, I. C. Khoo, T. S. Mayer, S. Nishimura, G. L. Egan, and T. E. Mallouk, "Direct fabrication of two-dimensional titania arrays using interference photolithography," *Appl. Phys. Lett.,* vol. 79, pp. 3332-3334, Nov. 12, 2001.

[207] Z. G. Guo, S. L. Qu, Y. H. Han, and S. T. Liu, "Multi-photon fabrication of two-dimensional periodic structure by three interfered femtosecond laser pulses on the surface of the silica glass," *Opt. Commun.,* vol. 280, pp. 23-26, Dec. 1, 2007.

[208] M. Vlcek, S. Schroeter, S. Brueckner, S. Fehling, and A. Fiserova, "Direct fabrication of surface relief gratings in chalcogenide glasses by excimer laser interference lithography," *J. Mater. Sci. - Mater. Electron.,* vol. 20, pp. 290-293, Feb. 5, 2009.

[209] M. Duarte, A. Lasagni, R. Giovanelli, J. Narciso, E. Louis, and F. Mucklich, "Increasing lubricant film lifetime by grooving periodical patterns using laser interference metallurgy," *Adv. Eng. Mater.,* vol. 10, pp. 554-558, June 2008.

[210] A. Lasagni, S. Peng, J. L. Hendricks, C. M. Shaw, D. C. Martin, and S. Das, "Direct fabrication of periodic patterns with hierarchical sub-wavelength structures on poly(3,4-ethylene dioxythiophene)poly(styrene sulfonate) thin films using femtosecond laser interference patterning," *Appl. Surf. Sci.,* vol. 256, pp. 1708-1713, Oct. 6, 2010.

[211] R. T. Greenway, R. Hendel, K. Jeong, A. B. Kahng, J. S. Petersen, Z. Rao, and M. C. Smayling, "Interference assisted lithography for patterning of 1D gridded design," *Proc. SPIE,* vol. 7271, pp. U1-U11, 2009.

[212] J. Murakowski, G. J. Schneider, and D. Prather, "Fabrication of 3-dimensional photonic crystals with embedded defects," *Proc. SPIE,* vol. 5347, pp. 181-189, 2004.

[213] L. Zhao, Y. Xuan, and M. Qi, "Generating integrated-circuit patterns via cutting and stitching of gratings," *J. Vac. Sci. Technol. B,* vol. 27, pp. 2750-2754, Nov./Dec. 2009.

[214] D. Szymanski, R. Dylewicz, S. Patela, S. Bartkiewicz, and A. Miniewicz, "Defects generation in photonic crystal pattern by electron beam induced deposition technique," *Proc. SPIE,* vol. 5950, pp. 59501T-1-59501T-6, 2005.

[215] C. J. M. van Rijn, "Laser interference as a lithographic nanopatterning tool," *J. Microlith. Microfab. Microsys.,* vol. 5, pp. 110121-110126, Jan.-Mar. 2006.

[216] H.-B. Sun, A. Nakamura, K. Kaneko, S. Shoji, and S. Kawata, "Direct laser writing defects in holographic lithography-created photonic lattices," *Opt. Lett.,* vol. 30, pp. 881-883, Apr. 15, 2005.

[217] P. V. Braun, S. A. Rinne, and F. Garcia-Santamaria, "Introducing defects in 3D photonic crystals: state of the art," *Adv. Mater.,* vol. 18, pp. 2665-2678, Oct. 2006.

[218] P. Parisse, D. Luciani, A. D'Angelo, S. Santucci, P. Zuppella, P. Tucceri, A. Reale, and L. Ottaviano, "Patterning at the nanoscale: atomic force microscopy and extreme ultraviolet interference lithography," *Mater. Sci. Eng. B,* vol. 165, pp. 227-230, Dec. 15, 2009.

[219] V. Ramanan, E. Nelson, A. Brzezinski, P. V. Braun, and P. Wiltzius, "Three dimensional silicon-air photonic crystals with controlled defects using interference lithography," *Appl. Phys. Lett.,* vol. 92, pp. 173304-1-173304-3, May 1, 2008.

[220] N. D. Lai, J. H. Lin, W. P. Liang, C. C. Hsu, and C. H. Lin, "Precisely introducing defects into periodic structures by using a double-step laser scanning technique," *Appl. Opt.,* vol. 45, pp. 5777-5782, Aug. 1, 2006.

[221] J. Scrimgeour, D. N. Sharp, C. F. Blanford, O. M. Roche, R. G. Denning, and A. J. Turberfield, "Three-dimensional optical lithography for photonic microstructures," *Adv. Mater.,* vol. 18, pp. 1557-1560, June 2006.

[222] C. A. Mack, *Field Guide to Optical Lithgraphy*. Bellingham, Washington: SPIE Press, 2006.

[223] H. H. Solak, "Nanolithography with coherent extreme ultraviolet light," *J. Phys. D: Appl. Phys.,* vol. 39, pp. R171–R188, May 5, 2006.

[224] J. H. Moon, J. Ford, and S. Yang, "Fabricating three-dimensional polymeric photonic structures by multi-beam interference lithography," *Polym. Adv. Technol.,* vol. 17, pp. 83-93, Feb. 2006.

[225] H. O. Everitt, "Applications of photonic band gap structures," *Opt. Photon. News,* vol. 3, pp. 20-23, Nov. 1992.

[226] G. Parker and M. Charlton, "Photonic crystals," *Phys. World,* vol. 13, pp. 29-34, Aug. 1, 2000.

[227] T. Y. M. Chan and S. John, "Circuits for light in holographically defined photonic-band-gap materials," *Phys. Rev. A,* vol. 78, pp. 33812-1-33812-13, Sept. 9, 2008.

[228] C. O. Cho, J. Jeong, J. Lee, H. Jeon, I. Kim, J. D. H., Y. S. Park, and J. C. Woo, "Photonic crystal band edge laser array with a holographically generated square-lattice pattern," *Appl. Phys. Lett.,* vol. 87, p. 161102, Oct. 10, 2005.

[229] R. C. Gauthier and K. Mnaymneh, "Towards physical implementation of an optical add-drop multiplexer (OADM) based upon properties of 12-fold photonic quasicrystals," *Proc. SPIE,* vol. 5970, pp. 59700-1-59700-10, 2005.

[230] U. Geyer, J. Hauss, B. Riedel, S. Gleiss, U. Lemmer, and M. Gerken, "Large-scale patterning of indium tin oxide electrodes for guided mode extraction from organic light-emitting diodes," *J. Appl. Phys.,* vol. 104, pp. 93111-1-93111-5, Nov. 12, 2008.

[231] G. Q. Liang, W. D. Mao, Y. Y. Pu, H. Zou, H. Z. Wang, and Z. H. Zeng, "Fabrication of two-dimensional coupled photonic crystal resonator arrays by holographic lithography," *Appl. Phys. Lett.,* vol. 89, pp. 173304-1-173304-3, July 24, 2006.

[232] Q.-Y. Lu, W. Zhang, L.-J. Wang, J.-Q. Liu, L. Li, F.-Q. Liu, and Z.-G. Wang, "Holographic fabricated photonic-crystal distributed-feedback quantum cascade laser with near-diffraction-limited beam quality," *Opt. Express,* vol. 17, pp. 18900-18905, Oct. 12, 2009.

[233] M. W. Klein, C. Enkrich, M. Wegener, and S. Linden, "Second-harmonic generation from magnetic metamaterials," *Science,* vol. 313, pp. 502-504, July 28, 2006.

[234] J. B. Pendry, A. J. Holden, D. J. Robbins, and W. J. Stewart, "Magnetism from conductors and enhanced nonlinear phenomena," *IEEE T. Microw. Theory,* vol. 47, pp. 2075-2084, Nov. 1999.

[235] J. B. Pendry and D. R. Smith, "The quest for the superlens," *Sci. Amer.,* vol. 295, pp. 60-67, July 2006.

[236] D. Schurig, J. J. Mock, B. J. Justice, S. A. Cummer, J. B. Pendry, A. F. Starr, and D. R. Smith, "Metamaterial electromagnetic cloak at microwave frequencies," *Science,* vol. 314, pp. 977-980, Nov. 10, 2006.

[237] V. G. Veselago, "The electrodynamics of substances simultaneously negative values of ε and μ," *Sov. Phys. Usp.,* vol. 10, pp. 509-514, July 1968.

[238] C. Caloz and T. Itoh, "Metamaterials for high-frequency electronics," *Proc. IEEE,* vol. 93, pp. 1744-1751, Oct. 2005.

[239] T. M. Grzegorczyk, C. D. Moss, J. Lu, X. Chen, J. Pacheco Jr, and J. A. Kong, "Properties of left-handed metamaterials: transmission, backward phase, negative refraction, and focusing," *IEEE T. Microw. Theory,* vol. 53, pp. 2956-2966, Sept. 2005.

[240] W. N. Hardy and L. A. Whitehead, "Split-ring resonator for use in magnetic resonance from 200--2000 MHz," *Rev. Sci. Instrum.,* vol. 52, pp. 213-216, Feb. 1981.

[241] G. Dolling, C. Enkrich, M. Wegener, C. M. Soukoulis, and S. Linden, "Simultaneous negative phase and group velocity of light in a metamaterial," *Science,* vol. 312, pp. 892-894, May 12, 2006.

[242] S. Linden, C. Enkrich, G. Dolling, M. W. Klein, J. Zhou, T. Koschny, C. M. Soukoulis, S. Burger, F. Schmidt, and M. Wegener, "Photonic metamaterials: magnetism at optical frequencies," *IEEE J. Sel. Top. Quantum Electron.,* vol. 12, pp. 1097-1105, Nov./Dec. 2006.

[243] H. Kikuta, H. Toyota, and W. Yu, "Optical elements with subwavelength structured surfaces," *Opt. Rev.,* vol. 10, pp. 63-73, Mar. 2003.

[244] R. Magnusson and S. S. Wang, "New principle for optical filters," *Appl. Phys. Lett.,* vol. 61, pp. 1022-1024, Aug. 31, 1992.

[245] R. Magnusson and S. S. Wang, "Transmission bandpass guided-mode resonance filters," *Appl. Opt.,* vol. 34, pp. 8106-8109, Dec. 10, 1995.

[246] S. Tibuleac and R. Magnusson, "Reflection and transmission guided-mode resonance filters," *J. Opt. Soc. Am. A,* vol. 14, pp. 1617-1626, July 1997.

[247] M. Shokooh-Saremi and R. Magnusson, "Leaky-mode resonant reflectors with extreme bandwidths," *Opt. Lett.,* vol. 35, pp. 1121-1123, Apr. 15, 2010.

[248] T. K. Gaylord, W. E. Baird, and M. G. Moharam, "Zero-reflectivity high spatial-frequency rectangular-groove dielectric surface-relief gratings," *Appl. Opt.,* vol. 25, pp. 4562-4567, Dec. 15, 1986.

[249] D. Sawaki and J. Amako, "Deep-UV laser-based nano-patterning with holographic techniques," *Proc. SPIE,* vol. 6459, pp. F1-F9, 2007.

[250] J. Amako, D. Sawaki, and E. Fujii, "High-efficiency diffractive beam splitters surface-structured on submicrometer scale using deep-UV interference lithography," *Appl. Opt.,* vol. 48, pp. 5105-5113, Sept. 10, 2009.

[251] J. S. Yu, Y. M. Song, J. W. Leem, and Y. T. Lee, "Subwavelength antireflection structures and their device applications," *Proc. SPIE,* vol. 7608, pp. 760812-1-760812-8, 2010.

[252] Y.-P. Chen, H.-C. Chiu, G.-Y. Chen, C.-H. Chiang, C.-T. Tseng, C.-H. Lee, and L. A. Wang, "Fabrication and measurement of large-area sub-wavelength structures with broadband and wide-angle antireflection effect," *Microelectron. Eng.,* vol. 87, pp. 1323-1327, Dec. 23, 2010.

[253] T. K. Gaylord, E. N. Glytsis, and M. G. Moharam, "Zero-reflectivity homogeneous layers and high spatial-frequency surface-relief gratings on lossy materials," *Appl. Opt.,* vol. 26, pp. 3123-3135, Aug. 1, 1987.

[254] N. F. Hartman and T. K. Gaylord, "Antireflection gold surface-relief gratings: experimental characteristics," *Appl. Opt.,* vol. 27, pp. 3738-3743, Sept. 1, 1988.

[255] P. B. Clapham and M. C. Hutley, "Reduction of lens reflection by the `moth eye' principle," *Nature,* vol. 244, pp. 281-282, Aug. 3, 1973.

[256] B. MacLeod and G. Sonek, "Motheye surfaces reflect little light," *Laser Focus World,* vol. 35, pp. 109-114, Aug. 1999.

[257] B. S. Thornton, "Limit of the moth's eye principle and other impedence-matching corrugations for solar-absorber design," *J. Opt. Soc. Am.,* vol. 65, pp. 267-70, Mar. 1975.

[258] S. J. Wilson and M. C. Hutley, "The optical properties of `moth eye' antireflection surfaces," *Opt. Acta (UK),* vol. 29, pp. 993-1009, in *Twelfth Congress of the International Commission for Optics,* UK, Aug. 5 - Sept. 5, 1981.

[259] H. Nakano, H. Morita, H. Washida, T. Kato, S. Hayashi, and A. Onoe, "Low cost and high performance antireflective coatings for solar cells," *Opt. Engr.,* vol. 24, pp. 207-212, Jan. 1985.

[260] B. L. Sopori and R. A. Pryor, "Design of antireflection coatings for textured silicon solar cells," *Solar Cells,* vol. 8, pp. 249-261, Apr. 1983.

[261] Y. M. Song, J. S. Yu, and Y. T. Lee, "Antireflective submicrometer gratings on thin-film silicon solar cells for light-absorption enhancement," *Opt. Lett.,* vol. 35, pp. 276-278, Feb. 1, 2010.

[262] L. Zhuang, S. Schablitsky, R. C. Shi, and S. Y. Chou, "Fabrication and performance of thin amorpnous Si subwavelength transmission grating for controlling vertical cavity surface emitting laser polarization," *J. Vac. Sci. Technol. B,* vol. 14, pp. 4055-4057, Nov. 1996.

[263] A. Minseung, R. K. Heilmann, and M. L. Schattenburg, "Fabrication of ultrahigh aspect ratio freestanding gratings on silicon-on-insulator wafers," *J. Vac. Sci. Technol. B,* vol. 25, pp. 2593-2597, Nov./Dec. 2007.

[264] D. L. Brundrett, E. N. Glytsis, and T. K. Gaylord, "Subwavelength transmission grating retarders for use at 10.6um," *Appl. Opt.,* vol. 35, pp. 6195-6202, Nov. 1, 1996.

[265] M. J. Colgan and M. J. Brett, "Field emission from carbon and silicon films with pillar microstructure," *Thin Solid Films,* vol. 389, pp. 1-4, June 15, 2001.

[266] N. S. Xu and S. E. Huq, "Novel cold cathode materials and applications," *Mater. Sci. Eng. R,* vol. 48, pp. 47-189, Jan. 31, 2005.

[267] J. P. Spallas, A. M. Hawryluk, and D. R. Kania, "Field emitter array mask patterning using laser interference lithography," *J. Vac. Sci. Technol. B,* vol. 13, pp. 1973-1978, Sept./Oct. 1995.

[268] M. K. Dawood, T. H. Liew, P. Lianto, M. H. Hong, S. Tripathy, J. T. L. Thong, and W. K. Choi, "Interference lithographically defined and catalytically etched, large-area silicon nanocones from nanowires," *Nanotechnol.,* vol. 21, pp. 205305-1-205305-9, Apr. 26, 2010.

[269] J. Yun, R. Wang, W. K. Choi, J. T. L. Thong, C. V. Thompson, Z. Mei, Y. L. Foo, and M. H. Hong, "Field emission from a large area of vertically-aligned carbon nanofibers with nanoscale tips and controlled spatial geometry," *Carbon,* vol. 48, pp. 1362-1368, Jan. 13, 2010.

[270] H. Li, X. Luo, C. Du, X. Chen, and Y. Fu, "Ag dots array fabricated using laser interference technique for biosensing," *Sens. Actuators, B,* vol. 134, pp. 940-944, July 4, 2008.

[271] P. K. Sahoo, K. Vogelsang, H. Schift, and H. H. Solak, "Surface plasmon resonance in near-field coupled gold cylinder arrays fabricated by EUV-interference lithography and hot embossing," *Appl. Surf. Sci.,* vol. 256, pp. 431-434, June 5, 2009.

[272] C. H. Liu, M. H. Hong, H. W. Cheung, F. Zhang, Z. Q. Huang, L. S. Tan, and T. S. A. Hor, "Bimetallic structure fabricated by laser interference lithography for tuning surface plasmon resonance," *Opt. Express,* vol. 16, pp. 10701-10709, July 7, 2008.

[273] J. W. Menezes, E. S. Braga, and L. Cescato, "Photonic crystals and plasmonic structures recorded by multi-exposure of holographic patterns," *Proc. SPIE,* vol. 7358, pp. 73580K-1-73580K-10, 2009.

[274] C. Daniel, "Biomimetic structures for mechanical applications by interfering laser beams: more than solely holographic gratings," *J. Mater. Res.,* vol. 21, pp. 2098-2105, Aug. 2006.

[275] D. Wu, Q.-D. Chen, J. Yao, Y.-C. Guan, J.-N. Wang, L.-G. Niu, H.-H. Fang, and H.-B. Sun, "A simple strategy to realize biomimetic surfaces with controlled anisotropic wetting," *Appl. Phys. Lett.,* vol. 96, pp. 53704-1-53704-3, Feb. 5, 2010.

[276] Y.-L. Yang, C.-C. Hsu, T.-L. Chang, L.-S. Kuo, and P.-H. Chen, "Study on wetting properties of periodical nanopatterns by a combinative technique of photolithography and laser interference lithography," *Appl. Surf. Sci.,* vol. 256, pp. 3683-3687, Jan. 11, 2010.

[277] Z. Zhang, X. Wang, Y. Liu, Y. Guo, Y. Hong, X. Xu, S. Fu, P. Xu, J. Wang, and J. Cai, "Fabrication of CoFe nanostructures by holographic lithography," *Proc. SPIE,* vol. 6831, pp. 68311B-1-68311B-6, 2008.

[278] R. Murillo, H. A. van Wolferen, L. Abelmann, and J. C. Lodder, "Fabrication of patterned magnetic nanodots by laser interference lithography," *Microelectron. Eng.,* vol. 78-79, pp. 260-265, Mar. 2005.

[279] W. O. Rosa, M. Knobel, L. Cescato, A. L. Gobbi, and M. Vazquez, "Experimental magnetic study and evidence of the exchange bias effect in unidimensional Co arrays produced by interference lithography," *Solid State Commun.,* vol. 142, pp. 228-231, Apr. 2007.

[280] P. M. Leufke, S. Riedel, M.-S. Lee, J. Li, H. Rohrmann, T. Eimuller, P. Leiderer, J. Boneberg, G. Schatz, and M. Albrecht, "Two different coercivity lattices in Co/Pd multilayers generated by single-pulse direct laser interference lithography," *J. Appl. Phys.,* vol. 105, pp. 113915-1-113915-6, June 5, 2009.

[281] P. A. Wieringa, R. W. F. Wiertz, E. L. de Weerd, and W. L. C. Rutten, "In vitro verification of a 3-D regenerative neural interface design: examination of neurite growth and electrical properties within a bifurcating microchannel structure," *Proc. IEEE,* vol. 98, pp. 389-397, Mar. 2010.

[282] M. P. Lutolf, F. E. Weber, H. G. Schmoekel, J. C. Schense, T. Kohler, R. Muller, and J. A. Hibbell, "Repair of bone defects using synthetic mimetics of collagenous extracellular matrices," *Nature Biotechnol.,* vol. 21, pp. 513-518, May 2003.

[283] J. R. Capadona, T. A. Petrie, K. P. Fears, R. A. Latour, D. M. Collard, and A. J. Garcia, "Surface-nucleated assembly of fibrillar extracellular matrices," *Adv. Mater.,* vol. 17, pp. 2604-2608, Nov. 2005.

[284] N. D. Gallant, J. R. Capadona, A. B. Frazier, D. M. Collard, and A. J. Garcia, "Micropatterned surfaces to engineer focal adhesions for analysis of cell adhesion stregthening," *Langmuir,* vol. 18, pp. 5579-5584, June 8, 2002.

[285] W. H. Koch, "Technology platforms for pharmacogenomic diagnostic assays," *Nat. Rev. Drug Discov.,* vol. 3, pp. 749-761, Sept. 2004.

[286] N. J. Sniadecki, R. A. Desai, S. A. Ruiz, and C. S. Chen, "Nanotechnology for cell-substrate interactions," *Ann. Biomed. Eng.,* vol. 34, pp. 59-74, Jan. 2006.

[287] G. Zhao, O. Zinger, Z. Schwartz, M. Wieland, D. Landolt, and B. D. Boyan, "Osteoblast-like cells are sensitive to submicron-scale surface structure," *Clin. Oral Implan. Res.,* vol. 17, pp. 258-264, June 2006.

[288] G. Sinclair, P. Jordan, J. Courtial, M. Padgett, J. Cooper, and Z. J. Laczik, "Assembly of 3-dimensional structures using programmable holographic optical tweezers," *Opt. Express,* vol. 12, pp. 5475-5480, Nov. 1, 2004.

[289] J. Leach, G. Sinclair, P. Jordan, J. Courtial, M. J. Padgett, J. Cooper, and Z. J. Laczik, "3D manipulation of particles into crystal structures using holographic optical tweezers," *Opt. Express,* vol. 12, pp. 220-226, Jan. 12, 2004.

[290] F. Horner, M. Woerdemann, S. Muller, B. Maier, and C. Denz, "Full 3D translational and rotational optical control of multiple rod-shaped bacteria," *J. Biophotonics,* vol. 3, pp. 468-475, May 10, 2010.

[291] M. Woerdemann, S. Glasener, F. Horner, A. Devaux, L. D. De Cola, and C. Denz, "Dynamic and reversible organization of zeolite L crystals induced by holographic optical tweezers," *Adv. Mater.,* vol. 22, pp. 4176-4179, Oct. 1, 2010.

[292] M. P. MacDonald, L. Paterson, W. Sibbett, K. Dholakia, and P. E. Bryant, "Trapping and manipulation of low-index particles in a two-dimensional interferometric optical trap," *Opt. Lett.,* vol. 26, pp. 863-865, June 15, 2001.

[293] P. Jakl, T. Cizmar, M. Sery, and P. Zemanek, "Static optical sorting in a laser interference field," *Appl. Phys. Lett.,* vol. 92, pp. 11101-11103, Apr. 24, 2008.

[294] L. Yuan, G. P. Wang, and X. K. Huang, "Arrangements of four beams for any Bravais lattice," *Opt. Lett.,* vol. 28, pp. 1769-1771, Oct. 1, 2003.

[295] E. B. Li, J. T. Xi, and J. Chicharo, "Predication of multi-dimensional photonic crystal structures generated by multi-beam interference in holographic lithography," *Smart Mater. Struct.,* vol. 15, pp. 158-64, Dec. 13, 2006.

[296] M. Fernández Guasti, A. Meléndez Cobarrubias, F. J. Renero Carrillo, and A. Cornejo Rodríguez, "LCD pixel shape and far-field diffraction patterns," *Optik,* vol. 116, pp. 265-269, July 6, 2005.

[297] The Mathworks, Inc., Natick, Massachusetts.

[298] MicroChem Corp., Newton, Massachusetts.

[299] Newport Corporation, Irvine, California.

[300] Anatech USA, Union City, California.

[301] LEO Elektronenmikroskopie GmbH, Oberkochen, Germany.

[302] Z. Fajian, Z. Liangmin, and R. O. Claus, "Investigation of the photoresist pattern profile contrast improvement in interference lithography technique using 488-nm laser," *IEEE Trans. Semicond. Manuf.,* vol. 21, pp. 464-468, 2008.

[303] S. Boscolo, M. Midrio, and C. G. Someda, "Coupling and decoupling of electromagnetic waves in parallel 2D photonic crystal waveguides," *IEEE J. Quantum Electron.,* vol. 38, pp. 47-53, Jan. 2002.

[304] A. K.-K. Wong, *Optical Imaging in Projection Microlithography*. Bellingham, WA: SPIE Optical Engineering Press, 2005.

[305] B. W. Smith, "Optics for photolithography," in *Microlithography: Science and Technology*, K. Suzuki and B. W. Smith, Eds., 2nd ed. ed Boca Raton: CRC Press, 2007.

[306] *Zemax Optical Design Program User's Guide*: Focus Software, Inc.,Tucson, Arizona, 2003.

[307] J. R. Sheats and B. W. Smith, *Microlithography: Science and Technology*. New York: Marcel Dekker, 1998.

[308] M. Born and E. Wolf, *Principles of Optics*, 6 ed. New York: Pergamon Press, 1980.

[309] Radian Zemax LLC, Bellevue, Washington.

[310] D. C. Cole, E. Barouch, U. Hollerbach, and S. A. Orszag, "Derivation and simulation of higher numerical aperture scalar aerial images," *Jpn. J. Appl. Phy.,* vol. 31, pp. 4110-4119, Dec. 1992.

[311] Olympus America, Inc., Melville, New York.

[312] B. W. Smith and R. Schlief, "Understanding lens aberration and influences on lithographic imaging," *Proc. SPIE,* vol. 4000, pp. 294-306, 2000.

[313] D. G. Flagello, T. Milster, and A. E. Rosenbluth, "Theory of high-NA imaging in homogeneous thin films," *J. Opt. Soc. Am. A,* vol. 13, pp. 53-64, 1996.

[314] M. Totzeck, P. Graupner, T. Heil, A. Gohnermeier, O. Dittmann, D. Krahmer, V. Kamenov, J. Ruoff, and D. Flagello, "Polarization influence on imaging," *J. Microlith. Microfab. Microsys.,* vol. 4, pp. 31108-1, 2005.

[315] B. J. Thompson, "Image formation with partially coherent light," in *Progress in optics, vol.VII*, ed London, UK: North Holland, 1969, pp. 171-229.

[316] L. F. Mollenauer and W. J. Tomlinson, "Piecewise interferometric generation of precision gratings," *Appl. Opt.,* vol. 16, pp. 555-557, Mar. 1977.

[317] P. T. Konkola, C. G. Chen, R. K. Heilmann, and M. L. Schattenburg, "Beam steering system and spatial filtering applied to interference lithography," *J. Vac. Sci. Technol. B,* vol. 18, pp. 3282-3286, 2000.

[318] M. Miler, F. Kostka, and M. Dvorak, "Scanning for piecewise holographic grating generation," *Proc. SPIE,* vol. 6180, pp. 61801F-1-61801F-8, 2005.

[319] H. J. Deyerl, N. Plougmann, J. B. Jensen, F. Floreani, H. R. Sorensen, and M. Kristensen, "Fabrication of advanced Bragg gratings with complex apodization profiles by use of the polarization control method," *Appl. Opt.,* vol. 43, pp. 3513-22, June 10, 2004.

[320] B. R. Napier and N. J. Phillips, "Writing long holographic diffraction gratings by use of a novel scanning method," *Appl. Opt.,* vol. 40, pp. 5170-5174, Oct. 10, 2001.

[321] Periodic Structures, Inc., Los Gatos, California.

[322] Thorlabs, Ltd., Newton, New Jersy.

VITA

Guy “Matt” Burrow was born in 1970 in Big Spring, Texas. He received his Bachelor of Science in Electrical Engineering from the United States Military Academy at West Point in 1992. After serving 10 years as an Army aviator, he returned to school and received his Master of Science in Electrical and Computer Engineering from the Georgia Institute of Technology in 2002. Following graduation, Matt served as an Instructor from 2002-2004 and an Assistant Professor from 2004-2005 in the Department of Electrical Engineering and Computer Science at West Point. As an Assistant Professor at West Point, Matt received the 2005 Education Excellence Award. After serving an additional four years as an Army Space Operations Officer, he returned to Georgia Tech in 2009. Matt is a member of Eta Kappa Nu, the Optical Society of America, the Institute of Electrical and Electronics Engineers, and the Army Space Professional Association. Matt remains an active duty Army lieutenant colonel with over 20 years of service.